Synthetic Aperture Radar for Process-Related Monitoring in Urban and Mining Areas

Von der
Fakultät Architektur, Bauingenieurwesen und Umweltwissenschaften
der Technischen Universität Carolo-Wilhelmina
zu Braunschweig

zur Erlangung des Grades eines
Doktor-Ingenieurs (Dr.-Ing.)
genehmigte

Dissertation

von
Donglie Liu
geboren am 23.09.1987
aus Hunan, China

Eingereicht am	21. Juni 2013
Disputation am	09. Dezember 2013
Berichterstatter	Prof. Dr.-Ing. habil. Wolfgang Niemeier
	Prof. Dr.-Ing. Axel Preuße

2014

Abstract

Considering it is hazardous to the environment and people, monitoring land movements at urban area become more and more significant. This is mainly due to human activities (or man-made geological processes). For example, civil engineering construction and use of underground water brought a lot of subsidence in many cities in the past years. On the other hand, studying of land movements in non-urban area is also important. Mining activities, earthquakes, volcanos induced land movements occur all over the world. Such land movements are normally strong and come with big hazards. Synthetic aperture radar using interferometric technique, which is known as InSAR, is capable of providing a quite denser measurement over large areas. Furthermore, SAR can work during both day and night and under all weather conditions. Nowadays, there are increasing interests of applying SAR to ground movements monitoring. More specifically, Interferometric SAR (InSAR), Differential InSAR (DInSAR), Persistent Scatterers InSAR (PSI) techniques are developing to meet people's requirements of detecting land movements. Persistent Scatterer Interferometry (PSI) is the extension of conventional InSAR and aims at addressing the influences of de-correlation and atmospheric delay in InSAR processing. PSI investigates the characteristics of all phase stable points on a succession of time-ordered SAR images. Such points with stable phase temporally are so-called PS points that with dominant scatterers in the resolution cells.

Due to the different features of urban and non-urban area, the application of InSAR for land movements monitoring may come cross different challenges. In urban area, buildings and infrastructure may provide lots of good back scatterers. However, the displacement in urban area is normally insignificant and therefore easy to be contaminated by atmospheric effect. On the contrary, non-urban area lacks of concrete structures but has abundance vegetation so that coherence loss is a problem that could not be ignored here. Besides, land movements in non-urban area that people would like to pay attention to are always with higher intensity scales than those in urban area. Subsequently, another problem occurs when the land displacement has big phase gradient and exceeds the maximum detectable gradient of InSAR, which is one fringe in one pixel. Therefore, InSAR applications to urban and non-urban area were discussed separately in this thesis.

Düsseldorf was used as the urban test site by processing 20 TerraSAR-X images using PSI. The algorithms and approaches integrated in the open source software DORIS and following StaMPS were chosen in data processing. DORIS processed this TerraSAR-X data set and formed interferograms. Subsequently, a combined MTI (multi-temporal InSAR) which integrated both PS and SBAS methods in StaMPS was applied for time series analysis of 787,991 persistent scatterers selected over $12.3\ km^2$. Atmospheric effect was estimated as a parameter and eliminated in this processing. The GPS station in Düsseldorf was set as the start point of 3-D unwrapping. Levelling results provided by the State Capital of Düsseldorf validated the PSInSAR result, when two time series showed similar progress with very few discrepancies. Furthermore, we compared the difference of PPP-derived atmospheric delay between two dates to that estimated by PSInSAR. The result of this comparison is not so delightful. Nevertheless, it could be a good approach to use GPS for eliminating atmospheric effect in InSAR, according to the theoretical study and some excellent works carried out by other researchers in this field.

Xishan mining region was chosen as the non-urban test site in this project, because of clear advantages. Such as well served mining schedule and literature and rapid movements with big phase gradients. A major advantage is that the TerraSAR-X acquisitions is cooperated by synchronous field work and GPS-CR (Corner Reflector) measurements. In the DDG (Detectable Deformation Gradient) test, 2-look seems to be a good choice for Xishan case where the deformation gradients are predictable large. One conclusion is people have to select SAR data set with suitable wavelength and choose a good look number for InSAR processing, in order to make sure reliable results are obtained.

In the experiments carried out in Xishan mine, InSAR fulfilled the aim of mining parameters derivation. Advanced influence angle and distance were successfully estimated for the test at Tunlan test site. Besides, it was confirmed that InSAR is able to measure the initial moving distances with the help of mining schedule according to data analysis at Xiqu test site. Due to the retention of high coherence and being strong back scatterers, a corner reflector network was established in this experiment. GPS surveying was collated for the coordinates of corner reflectors, which can validate and improve the accuracy of geocoding (< 5 m).

Zusammenfassung

Die Überwachung von Setzungen in städtischen Gebieten wird immer wichtiger, da es sich um eine potenzielle Bedrohung für Umwelt und den Menschen handelt. Ein Teil der Gefahren durch Oberflächenbewegungen werden durch menschliche Aktivitäten oder geologische Prozesse verursacht. Als Beispiel, Aufgrund der Baukonstruktion und der Nutzung von Grundwasser, wurden viele Städte in den vergangenen Jahren erheblich abgesetzt. Mögliche Beispiele für signifikante Setzung ist der Einfluß von Bauprozessen oder die Senkung des Grundwasserspiegels. Die Untersuchung von Landsenkungen in nicht-städtischen Bereichen sind ebenfalls sehr wichtig, da in der ganzen Welt Bergbau, Erdbeben und Vulkanaktivitäten derartige Setzungen verursachen können. Solche Bodenbewegungen führen zu großen Gefahren.

Mit interferometrischen Auswertungen von Synthetic Aperture Radar Messungen (InSAR) ist man in der Lage große Bereiche hochauflösend zu beobachten. SAR Systeme können während des Tages, der Nacht und unter allen Wetterbedingungen arbeiten. Heutzutage gibt es zunehmendes Interesse an der Anwendung von SAR für das Monitoring von Veränderungen der Erdoberfläche. Hierzu wurden speziell die Techniken des Interferometrischen SAR (InSAR), Differential InSAR (DInSAR) und Persistent Scatterers InSAR (PSI) entwickelt. Die PSI-Technologie ist eine Erweiterung der konventionellen InSAR Methode und zielt darauf ab, die Einflüsse von Dekorrelation und atmosphärische Verzögerungen bei der InSAR Verarbeitung zu berücksichtigen. PSI untersucht die Merkmale aller phasenstabilen Punkte entlang einer Zeitreihe der SAR-Bilder. Solche Punkte mit zeitlich stabiler Phase sind die sogenannten PS Punkte mit dominanten Streuern in den Auflösungszellen.

Aufgrund der unterschiedlichen Merkmale von urbanen und nichturbanen Gebieten, kann die Anwendung von InSAR für das Monitoring von Bewegungen unterschiedliche Herausforderungen stellen. In städtischen Gebieten bieten Gebäude und andere Strukturen eine Vielzahl von Körpern mit guten Rückstreueigenschaften. Allerdings sind die Verschiebungen in städtischen Gebieten in der Regel gering und können daher leicht durch atmosphärische Effekte kontaminiert werden. Im Gegensatz dazu fehlen in nicht städtischen Gebieten große Flächen mit starken Rückstreuern, dadurch führt das Vorhandensein einer reichen Vegetation zur Verminderung bzw. dem Verlust der Kohärenz. Das ist ein Problem, das nicht ignoriert werden kann. Wenn die Oberflächenveränderungen zu große Phasengradienten haben führt dies dazu, dass der maximal erfassbare Phasengradient von einem Fringe pro Pixel in der InSAR Auswertung erreicht wird. Daher werden die Anwendung der InSAR Technologie - in urbanen und nichturbanen Gebieten in dieser Arbeit separat diskutiert.

Die Stadt Düsseldorf wurde als Testfeld für die Verarbeitung von 20 TerraSAR-X Bilder mit PSI ausgewählt. Für die Datenverarbeitung wurden die Algorithmen und Ansätze, die in den Open-Source-Software Paketen DORIS und PS integriert sind, genutzt. DORIS verarbeitet den TerraSAR-X-Daten-Satz und berechnet die Interferogramme. Anschließend wurde eine kombinierte MTI Auswertung (multi-temporale InSAR Processing auf Basis von PS und SBAS) mit StaMPS berechnet. Für die Zeitreihenanalyse wurden 787,991 Persistent Scatterer ausgewählt. Atmosphärische Effekte wurden als Parameter geschätzt und in der Bearbeitung berücksichtigt. Die GPS-Station in Düsseldorf wurde als Startpunkt des 3-D Phase Unwrapping gesetzt. Die Ergebnisse aus dem Nivellement der Landeshauptstadt Düsseldorf wurden für die Validierung der PSInSAR Ergebnisse genutzt. Zwei Zeitreihen zeigen einen ähnlichen Verlauf mit sehr geringen Abweichungen. Weiterhin wurde die Differenz der PPP-abgeleiteten atmosphärischen Verzögerung mit der aus PSInSAR geschätzten Verzögerung an 2 Tagen miteinander verglichen. Das Ergebnis dieses Vergleichs ist nicht optimal, dennoch könnte es ein guter Ansatz sein, um GPS Beobachtungen für die Beseitigung der atmosphärischen Wirkung auf die InSAR Auswertung nutzen zu können, da das Studium der Theorie und die vorliegenden Arbeiten von anderen Forschern auf diesem Gebiet diese Möglichkeit aufzeigen.

Die Bergbauregion Xishan wurde als nichturbanes Testgebiete in diesem Projekt ausgewählt, weil es die Möglichkeit bietet an Informationen über den Bergbau, die Zeitpläne und Literatur zu kommen und es dort schnelle Oberflächenbewegungen mit großen Phasengradienten gibt. Ein großer Vorteil ist, dass die TerraSAR-X Akquisitionen von zeitgleichen Feldarbeiten mit GPS-Corner Reflectoren (CR) Messungen stattfanden. Die Untersuchung von DDG (Detektierbare Deformationsgradient) zeigt, dass ein zwei-mal-zwei Multilook eine gute Wahl für dieses Gebiet ist, da dort große Verformungsgradienten vorhersehbar sind. Eine Schlussfolgerung in der Arbeit ist, dass die SAR-Daten mit geeigneter Wellenlänge und ein entsprechender Multilook-Faktor für InSAR Verarbeitung auszuwählen ist, um sicherzustellen, dass zuverlässige Ergebnisse erzielt werden können.

Die durchgeführten Experimente im Xishan Gebiet zeigen, dass man mit der InSAR Auswertung auch Bergbauparameter ableiten kann. Der erweiterte Einflusswinkel und der dazugehörige Abstand wurden erfolgreich für das Testgelände Tunlan geschätzt. Darüber hinaus wurde für die Xiqu Mine bestätigt, dass durch die Datenanalyse von InSAR Beobachtungen man in der Lage ist, die untertägige Bewegung in Verbindung mit dem Bergbauzeitplan zu bestimmen. In diesem Gebiet konnte auch ein CR-Netzwerk etabliert werden, da die CR ihre hohe Kohärenz und ihre starke Rückstreueigenschaft beibehalten. Für die Koordinatenbestimmung der Corner Reflektoren wurden GPS Messungen durchgeführt, die auch zur Verbesserung der Satellitenbasislinien dienen und die Genauigkeit der Geokodierung (<5 m) verbessern.

Acknowledgements

This research has been undertaken at the Institute of Geodesy and Photogrammetry, TU Braunschweig. Funding for this PhD project was supported by Institute of Geodesy and Photogrammetry. This work is also linked to the TerraSAR-X satellite project CAL1140 and LAN1185 kindly supported by the German Aerospace Centre (DLR). The GPS data sources of Düsseldorf experiment were provided SAPOS® through Geobasis NRW.

The foremost thankyou to my supervisors, Prof. Wolfgang Niemeier and Prof. Axel Preusse, who mentored me and encouraged me throughout my PhD program. I am very grateful to Dr. Björn Riedel, for his continued support and guidance.

I owe special thanks to groups who developed and maintain ROI_PAC (JPL), DORIS (TU Delft), StaMPS (Stanford University and TU Delft), PUNNET (Andrew Sowter), GIPSY (JPL). These open source softwares made my research possible and easier. Besides, I would like to thank my friends Dr. Jianghui Geng in SCRIPPS, University of California San Diego, and Dr. Zhen Dai in DLR for their constructive discussions. Besides, many thanks to Dr. Batuhan Osmanoglu in University of Alaska Fairbanks, for the smart Automated DORIS Environment (ADORE).

Further thanks go to Dr. Andrew Sowter for his constant support since I met him in 2008. I am very grateful to Prof. Yunjia Wang in CUMT for his continued recommendations. A special thanks must go to Prof. Zhengfu Bian and Mr. Zhenguo Liu, who cooperated with me on Xishan project and provided excellent results from field work and data processing in CUMT.

I would like to express my thanks to all colleagues in IGP, and also to my housemates Mr. Yanan Cai and Mr. Weiwei Du.

Finally, I reserve my special appreciation for my family. I am grateful to my parents for supporting and encouraging me all the time. Thanks go to my girlfriend, now my wife Lili Zhang for her unshaking belief in me, and for her patience while the weekends and holidays were taken from her by this PhD project.

Contents

List of Figures

List of Tables

Acronyms and Abbreviations

2-DInSAR	Two-pass Differential InSAR
3-DInSAR	Three-pass Differential InSAR
4-DInSAR	Four-pass Differential InSAR
ASAR	Advanced Synthetic Aperture Radar
CGPS	Continuous GPS
CMF	Chao Mapping Function
DEM	Digital Elevation Model
DInSAR	Differential Interferometric SAR
DLR	Deutsches Zentrum für Luft- und Raumfahrt (German Aerospace Center)
ECMWF	European Centre for Medium-range Weather Forecasts
GMF	Global Mapping Function
GPS	Global Positioning System
IGS	International GPS Service
InSAR	SAR Interferometry (or Interferometric SAR)
JPL	Jet Propulsion Laboratory
LOS	Line of Sight
NASA	National Aeronautics and Space Administration
NMF	Niell Mapping Function
NWM	Numerical Weather Model
RAR	Real Aperture Radar
RMS	Root Mean Square
SAR	Synthetic Aperture Radar
SHB	Subsidence Hazard Boundary
SLC	Single Look Complex
SRTM	Shuttle Radar Topography Mission
TEC	Total Electron Content
VMF	Vienna Mapping Function
ZHD	Zenith Hydrostatic Delay
ZTD	Zenith Total Delay
ZWD	Zenith Wet Delay

Chapter 1 Introduction

1.1 Background

Studying of land movements is significant. Mining activities, earthquakes, volcanos induced land movements occur all over the world. Such land movements are normally strong and come with big hazards. On the other hand, land movements at urban area also become more and more frequent. This is mainly due to human activities. For example, civil engineering construction, mining and use of underground water have brought a lot of subsidence in many cities. Considering it is hazardous to the environment and people, it is high time that we require knowledge and process-related monitoring to such movements. In the past 20 years, GPS is widely applied on deformation monitoring and has provided lots of high-quality results. GPS, however, only measures sparse points. Fortunately, synthetic aperture radar using interferometric technique, which is known as InSAR, is capable of providing a quite denser measurement. However, InSAR also has some limitations like relative low temporal resolution and deccorelation problems.

1.2 Urban Surface Movements

Since the industrial age, cities are expanding fast and urban ground movements are widespread. Surface movements in urban areas may lead to building and road damages, large-scale subsidence then kinds of geo-hazards. Firstly, it will threaten even endanger people' lives. On the other hand, such damages to infrastructure and buildings cost huge money each year (BGS, 2002). Wide characteristics lead to movements in urban areas. As (Leighton, 2010) said, the factors behind urban ground movements come from many different sources. People have to consider the hydrology, geology and historic evidence, and so on. For instance, construction of subway, underground water extraction and increasing skyscrapers provide challenges to engineers and geologists.

In fact, many movements are very slight at the beginning and may be ignored easily. Unfortunately, it is always too late to pay attention to when the movements have manifested to be catastrophic. Therefore, detecting small movements and long term monitoring are necessary.

1.3 Non-urban Surface Movements

Unlike urban area, buildings and people are fewer in non-urban areas. Nevertheless, we must pay attention to the non-urban movements due to three main reasons. The first, things behind the non-urban movements like mining activities, volcanic eruptions and earthquakes often attract scientists' interests even though few people live in those areas. Secondly, subsidence in mining areas and geo-hazards mentioned before may cause economic losses. Thirdly, movements in non-urban area will lead to geo hazards and have influences to urban areas, i.e., mud-rock flow in Figure 1.1.

Monitor non-urban area movements provides more challenges than urban areas. At some non-urban regions (e.g. mining area), it is difficult for people to get access to because vegetation and terrain conditions may barrier the way to carrying out engineering survey. In some other cases, large-scale movements require extremely hard work and therefore advanced technique is needed. We will take a mining region as the experimental area in this study.

Figure 1.1 Zhouqu (in China) mud-rock flow happened on 8th Aug, 2010. (Available on 8th Oct 2013. http://news.xinhuanet.com/politics/2011-08/07/c_121824181.htm)

1.4 Detection of Movements

People developed lots of techniques to detect ground movements. Levelling is one of the most widely applied techniques due to its high precision when measure heights. Levelling networks were set up in many countries and there is no doubt that levelling played an important role in history. However, levelling is an expensive method for measuring movements with labour intensive feature. Since 1980s, the Navigation Satellite Timing and Ranging/Global Positioning System (GPS) has been used more and more often in geodesy, since it is able to work worldwide under all weather conditions and no matter day or night. Like all other techniques, GPS has drawbacks. GPS can only provide observations of discrete points. Besides, under some situations, it poses safety risks on antenna or receiver installation. Apparently, photogrammetry, which is detecting objects' geometric properties with the help of optical images, can provide information of surfaces.

Synthetic Aperture Radar (SAR) has most advantages of traditional photogrammetric technologies. Moreover, it can also work during both day and night and under all weather conditions. Nowadays, there are increasing interests of applying SAR to ground movements monitoring. More specifically, Interferometric SAR (InSAR), Differential InSAR (DInSAR), Persistent Scatterers InSAR (PSI) techniques are developing to meet people's requirements of detecting ground movements.

1.5 Contributions of this research

This thesis focuses on SAR for studying land movements and solutions to problems that hinder its further applications.

From point-of-view of geodesists and geoscientists, several contributions may be of interests are addressed here:

1. Advantages and limitations of applying InSAR to monitor process-related movements in urban and mining areas have been found out. Relevant solutions to such limitations have been proposed.

2. Research on the atmospheric effects on InSAR measurements has been carried out. PSI and GPS were tested for reducing atmospheric effects. By reducing atmospheric effects and other errors, InSAR is able to detect process –related movements at millimetre level in urban area.
3. We applied InSAR technique with multiple platform satellite data such as ALOS, ENVISAT and TerraSAR-X data to active mining areas which the movements are rapid and phase gradients are big. Limitations of applying TerraSAR-X data have been analysed. Proper processing methodology for overcoming such limitations has been proposed. It has been proved that TerraSAR-X fulfilled most of the requirements of deriving mining parameters in mountainous area.
4. A software platform of SAR and InSAR processing has been established in IGP by integrating open source packages such as ROI_PAC, DORIS, PUNNET and StaMPS.

1.6 Research Methodology

The research aims of the thesis were presented above. In order to achieve those objectives, the research methodology is given below.

- Study the background and theory of InSAR and relevant topics. Global Positioning System (GPS) and Precise Point Positioning (PPP) technique review.
- Research on Atmosphere structure and components, and its effects to signal propagations. Find different ways to estimate atmospheric effects to electromagnetic signals.
- Select a test site in urban area where both the SAR data and GPS measurements are available. Try persistent scatterers method for eliminating atmospheric effects.
- Apply GPS PPP to derive Zenith Wet Delay (ZWD) parameters for correcting atmospheric effects.
- Compare corrected InSAR results to instrumental observations.
- Select a test site in nor-urban area where the movements are rapid and phase gradients are large.
- Apply Stanford Method for Persistent Scatterers (StaMPS) to this nor-urban area, and evaluate the quality and density of persistent scatterers.
- Study the maximum detectable phase gradients by InSAR. Find suitable methods and parameters for detecting movements with big phase gradients.
- Use these methods and parameters evaluated already to derive the movements at test site.
- Process GPS data and use the results for the validation of InSAR results.
- Derive mining parameters required by mining engineering based on InSAR results.

1.7 Thesis Overview

This thesis is arranged as 6 chapters. Following this chapter, chapter 2 reviews the histories and principles of SAR and GPS, the theory of SAR and relevant techniques, including InSAR, DInSAR, PSInSAR, are studied. Furthermore, the PPP technique is explained.

Chapter 3 reviews the knowledge of atmosphere, including its structure and components. Also, atmospheric effects on microwave propagation are reviewed. Consequently, we study different techniques of atmospheric correction and compare their advantages and disadvantages. Besides, different mapping functions are compared and discussed, as mapping function is one of the key parts of atmospheric correction, especially when applying PPP technique.

Chapter 4 starts with describing the first test site, the city centre of Düsseldorf. Climate, topography are discussed as well as the activities, the existing SAR data and GPS data and instrumental measurements. Then both PS and GPS correction method are applied to eliminate the atmospheric effects. This chapter finishes by comparing InSAR results corrected by different methods.

Chapter 5 is dedicated to study on using SAR to take the challenge of detecting land movements when the movements are rapid and phase gradients are large. Xishan coal mine, which has available SAR data and corner reflectors and GPS control survey, is a perfect test site for our experiment. StaMPS method shows its advantages to obtain sufficient PS points in non-urban area. However, it is not able to solve all problems in this area. One main finding in this study is determination of reliable methods and parameters for detecting movements with big phase gradients. Finally, we detect corner reflectors at the test sites and evaluate the accuracy of geocoding.

Chapter 6 provides conclusions and comments, which leads to recommendations for future work.

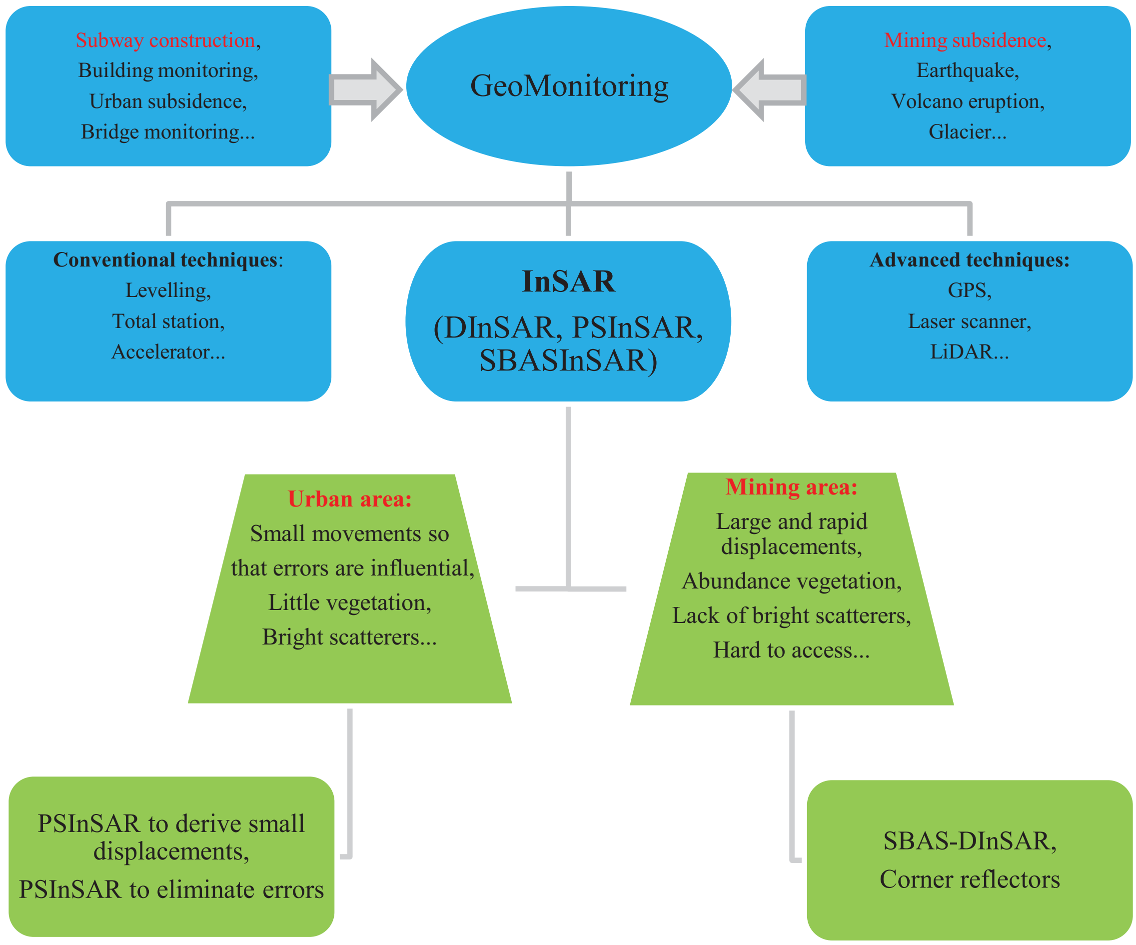

Figure 1.2 Research methodology.

1.8 Summary

This chapter has explained the importance of monitoring land movements and provided a background to this field. The objectives and research approach were briefly described. An overview of the thesis was then provided.

Chapter 2 Background

2.1 Radar history

As Lillesand and Kiefer (2004) defined: “Remote Sensing is the science and art of obtaining information about an object, area, or phenomenon through the analysis of data acquired by a device that is not in contact with the object, area, or phenomenon under investigation.”. Radar (Radio Detection and Ranging) is an important technique in remote sensing, as well as an instrument. Radar emits radio and microwave portions (from 1mm to 1m) of electromagnetic spectrum and receives reflections from objects. Antenna transmits signals of electromagnetic energy to targets, and then receives responses (reflected signals) from targets. The return signals then are collected and recorded to generate radar images. Therefore, radar is called active sensor.

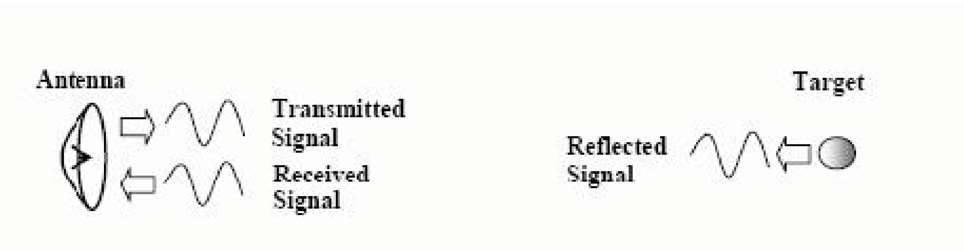

Figure 2.1 Basic operation of Radar (Sowter, 2003).

The monostatic radar uses only one antenna for both transmitting and receiving, whereas two antennas are used separately in bistatic radar (Skolnik, 1962).

As Ramon F. Hanssen pointed out in 2001, there are two landmark discoveries in the development of radar. One is Maxwell’s equations in “Treatise on Electricity and Magnetism” of electromagnetism in 1873.

$\nabla \cdot \mathbf{D} = \rho$	(1)	Gauss’ Law
$\nabla \cdot \mathbf{B} = 0$	(2)	Gauss’ Law for magnetism
$\nabla \times \mathbf{E} = -\frac{\partial \mathbf{B}}{\partial t}$	(3)	Faraday’s Law
$\nabla \times \mathbf{H} = \frac{\partial \mathbf{D}}{\partial t} + \mathbf{J}$	(4)	Ampère-Maxwell Law

Figure 2.2 Maxwell’s equation (Maxwell, 1873. Available on 1st Dec, 2013. http://www.ieeeghn.org/wiki/index.php/STARS:Maxwell's_Equations).

Equation one describes the nature of the electric field while equation two describes the nature of the magnetic field. Consequently, equation three shows the change of magnetic field excites the electric field, and equation four shows the change of electric field excites the magnetic field. These predicted exist of electromagnetic wave. The other landmark discovery is Hertz’s experiments in 1886, which generated and discovered the radio wave. In 1904, Huelsmeyer tried the first patent to use radar for a ship detecting. In the 1920s and 1930s, the US and the UK paid attention to the detection and navigation for ships and aircraft using radar. Some early advancements of radar took place during the period leading up to, and including World War II, with Germany, the UK, and the US all developing radar systems almost simultaneously (Curlander and McDonough, 1991). However, the civilian application of radar was widely carried out since 1960s. Early radars transmitted from the ground to the air or from an air platform to the ground, then noticed noise or ground clutter so that the terrain was recognized (Henderson and Lewis, 1998). JPL（Jet Propulsion Laboratory）brought the radar into space in 1962. After that, JPL started radar observation for lunar based on Apollo 17 in 1972. In 1978, one radar (with nadir-looking radar altimeter) which was on Pioneer 1 observed Venus, with a spatial resolution of about 50 km and an accuracy of about 300m (Hanssen, 2001). Higher resolution was achieved by the soviet venera 15 and 16 to 2 km (Curlander and McDonough, 1991). The 1990s, proved to be a fertile time for satellite-based Radar with the successful launch of a number of satellite Radar missions (Liu et al., 2012): the European Space Agency's (ESA) ERS-1/2, Japan's JERS-1, Russian's Almaz-1 and Canada's Radarsat-1. In February 2000, during an 11-day mission, NASA's Shuttle Radar Topography Mission (SRTM), which contained a specially modified radar system, flew onboard the Space Shuttle Endeavour. More recently, ESA's ENVISAT was launched in March 2002 and Japan's ALOS was launched in January 2006. Germany launched TerraSAR-X on June 15th, 2007, and then TanDEM-X on June 21st, 2010.

2.2 SAR

According to antenna theory, the area illuminated on the ground is inversely in proportion to the physical shape and dimensions of the antenna (Skolnik, 1962). As a result, a very long antenna is needed in real-aperture radar systems, in order to obtain good azimuth resolution. Synthetic aperture radar (SAR) is a coherent imaging method (Bamler et al., 1998) by active microwave with a long aperture. In other words, SAR is a modification of a basic imaging radar system that creates an artificially long antenna synthetically from a small moving antenna to improve spatial resolution in the azimuth (along-track) direction (Liu et al., 2012). The satellite flies along the fight path, and transmits microwave beam to illuminate the ground. The area illuminated on the ground is known as swath. For each pulse, one footprint is generated. The width of swath depends on the elevation beamwidth, which is in proportion to the wavelength and the width of the antenna. In each footprint, the azimuth beamwidth is proportional to the wavelength and the length of the antenna. The incidence angle is defined as the angle between the transmitted microwave and the nadir of the satellite (Fig. 2.3).

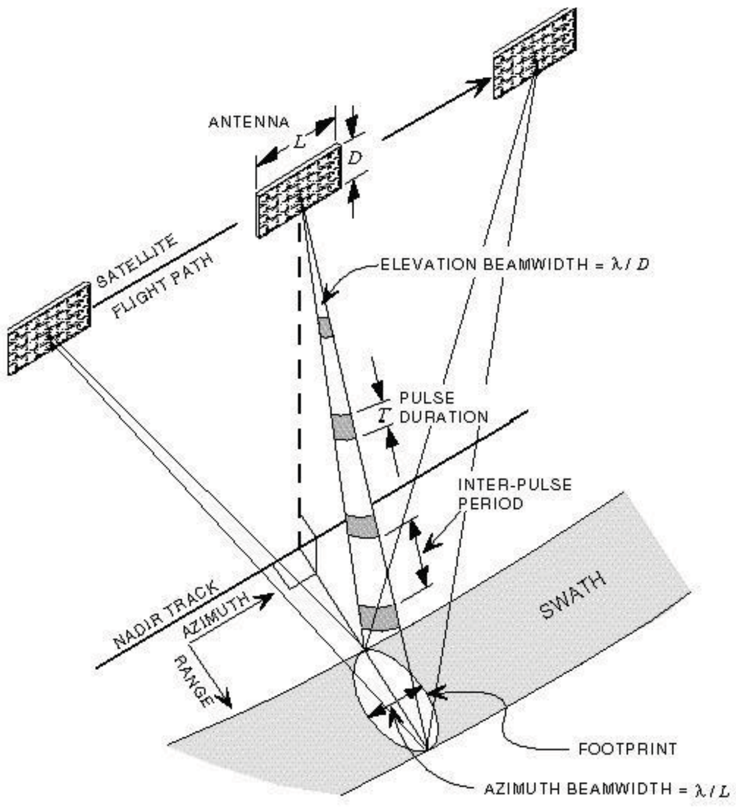

Figure 2.3 Geometry of SAR (Li, 2005. Olmsted, 1993).

Resolution defines the shortest separation distance between two targets for them to be resolved and displayed as individual features. It is fundamental to any remote sensing interpretation. Resolution is usually discussed in two directions: parallel and perpendicular to the moving line. For SAR system, people define range and azimuth resolutions.

The slant range resolution is the minimum distance between two targets along the line of sight that could be discerned as individual objects:

$$\Delta r_s = \frac{c\tau}{2} \tag{2.2.1}$$

where c is the speed of light, and τ is the pulse duration. The factor 2 accounts for the two-way propagation.

Consequently, the ground range resolution is defined as the minimum distance on the ground between two targets in the direction perpendicular to the flight path that could be discerned as individual objects:

$$\Delta r_g = \frac{c\tau}{2\sin\theta} \tag{2.2.2}$$

where θ is the incidence angle.

If high bandwidth phase coded waveforms, for instance, chirp pulses are used, the ground range resolution is given:

$$\Delta r_g = \frac{c}{2W\sin\theta} \tag{2.2.3}$$

where W is the frequency bandwidth of chirp pulses.

Take TerraSAR-X as an example, the nominal bandwidth of TerraSAR-X is 150 MHz. If the incidence angle is 24°, then the ground range resolution is around 2.5 m.

One have to be kept in mind is the slant range resolution is always better than the ground range resolution. The slant range resolution is independent of the incidence angle while the ground range resolution is affected by the incidence angle. In other words, the ground range resolution gets worse when the incidence angle decreases.

As for two targets to be separated in the azimuth direction, they should be within one beam. Therefore, the azimuth resolution Δa is dependent on the antenna azimuth beamwidth and distance in range:

$$\Delta a = \frac{1}{2}\beta R \tag{2.2.4}$$

where β is the beamwidth and R is the slant range. Beamwidth is the width of the area being imaged. Factor $\frac{1}{2}$ is added, because the same antenna is used for both transmitting and receiving normally, and therefore the beamwidth is sharpened. Apparently, the azimuth resolution improves when the beamwidth decreases. Since Δa is proportional to R, the azimuth resolution for long distance is decreased. Furthermore, beamwidth can be expressed in terms of the wavelength and the physical length of radar antenna.

$$\beta = \frac{\lambda}{L} \tag{2.2.5}$$

where λ is the wavelength, L is the physical length of radar antenna. Therefore, azimuth resolution is

$$\Delta a = \frac{1}{2}\frac{\lambda}{L}R \tag{2.2.6}$$

According to this equation, in addition to range (R) there are two other parameters that can be altered to increase azimuth resolution. One is decreasing wavelength and the other is increasing antenna length. However, both of them have limitations. For example, antenna lengths are limited by the size of system and degree of difficulties in manufacture. It was estimated that (Li, 2005) if ERS which has a 10 m antenna was adopted as a real aperture radar, the azimuth resolution would be about 4.8 km with a range R = 850 km. That means, a 2.4 km long antenna is required if we want 20 m azimuth resolution for ERS when ERS is not a SAR but a RAR. As mentioned before, SAR is developed to generate a longer antenna artificially. The accumulative time T_a for synthesizing a long aperture is (Yuan, 2003):

$$T_a = \frac{R\beta}{v_a} \tag{2.2.7}$$

where R is the slant range, β is the beamwidth, v_a is the fight velocity of the satellite.

The length of synthesized aperture is:

$$L_s = v_a T_a = R\beta \tag{2.2.8}$$

Considering equation (2.2.6), the azimuth resolution of SAR then is:

$$\Delta a_s = \frac{1}{2}\frac{\lambda}{L_s}R = \frac{\lambda}{2\beta} = \frac{L}{2} \tag{2.2.9}$$

Therefore, the azimuth resolution of a SAR is independent of range and wavelength and only be determined by the physical length of antenna. Take ERS as example again, the azimuth resolution achieve finer, from 4.8 km to 5 m (Li, 2005), by using synthetic aperture.

2.3 InSAR

Physically speaking, interference is a phenomenon that superimposition of two waves forms a consequent wave with lower or greater amplitude (Fig. 2.4). This phenomenon was noted in two slits experiment by Thomas Young in 1801 firstly. In other words, interference is the interaction of two waves which are coherent with each other. The basic requirement is that these waves come from the same source or have the same (similar) frequency.

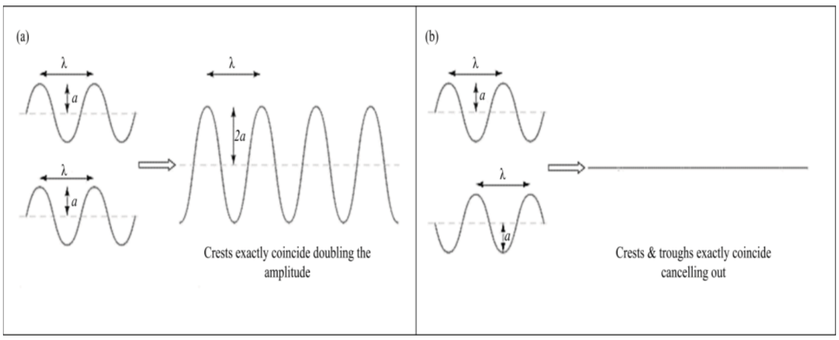

Figure 2.4 Waves interaction (Leighton, 2010).

In Figure 2.4 (a), two waves are in phase and produce constructive interference. Conversely, destructive interference appears when two waves are out of phase.

For SAR system, the frequency is constant so that phases preserved in SAR images from the same sensor are able to do interference, and form so-called interferogram in theory. In fact, a satellite-borne SAR can observe the same area simultaneously with two radars on the same satellite platform or it is able to observe and take images that area at different times by repeated orbits of the same satellite (Fig. 2.5). The latter is the usually used at the moment, for example, ERS-1/2, ENVISAT and TerraSAR-X.

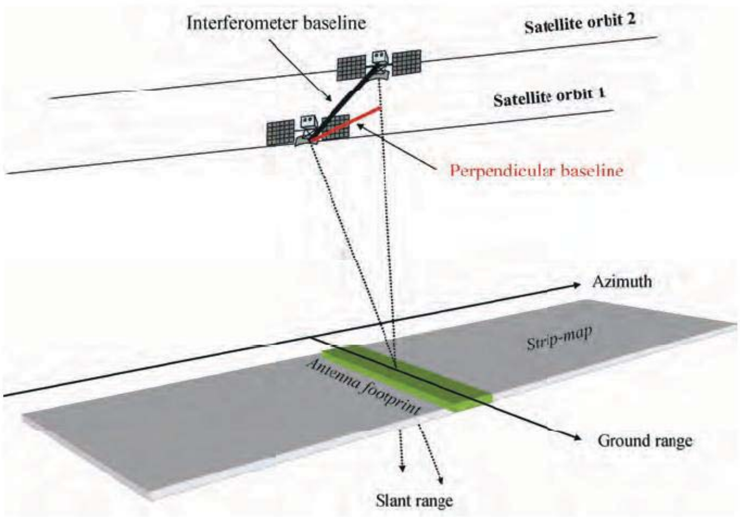

Figure 2.5 InSAR Geometry (ESA, 2007).

As shown in Figure 2.5, the distance between the two satellites is called the interferometer baseline, and its projection perpendicular to the slant range is called the perpendicular baseline, which is more important in InSAR processing.

2.3.1 InSAR Mathematic Model

In an error free environment, Interferometric SAR (InSAR) measures the phase differences between two SAR acquisitions S_1 and S_2 which are primarily related to the position change of P on the Earth surface (Fig. 2.6).

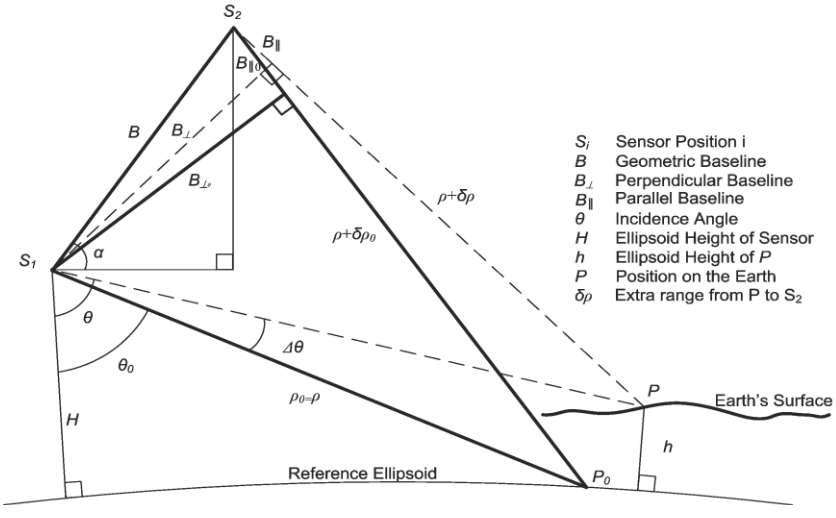

Figure 2.6 Earth and ellipsoidal InSAR Geometry (Hanssen, 2001).

In the figure above, S_1 and S_2 are two acquisitions (or two radar sensors), B is the geometry baseline, $B_\perp$ is the perpendicular baseline, $B_\parallel$ is the parallel baseline, H is the ellipsoid height of S_1, P is a point on the Earth with a ellipsoid height of h, P_0 is a corresponding point on the reference ellipsoid, θ is the look angle, Δθ is the angular distortion due to the topography, α is the angle of the geometry baseline with respect to the horizontal. The range between S_1 and P is ρ when between S_2 and P is $\rho + \delta\rho$. P_0 is with the same distance ρ from S_1 as P.

If there is a movement of the object between two observations, the measured phase difference ϕ, which is called interferometric phase is (Zebker et al., 1994):

$$\phi = \frac{4\pi}{\lambda}\delta\rho \qquad (2.3.1)$$

where λ is the SAR wavelength, $\delta\rho$ is the range difference between S_1 and S_2.

It is impossible to obtain $\delta\rho$ in practice directly because of the orbit inaccuracies and phase ambiguity (Leighton, 2010). Then people consider geometry in Figure 2.6 and give:

$$(\rho + \delta\rho)^2 = \rho^2 + B^2 - 2\rho B\sin(\theta - \alpha) \quad (2.3.2)$$

And by removed ρ^2 on both sides, it can be expressed to:

$$2\rho\delta\rho + \delta\rho^2 = B^2 - 2\rho B\sin(\theta - \alpha) \quad (2.3.3)$$

The $\delta\rho^2$ term can be ignored, because $\delta\rho \ll \rho$. As demonstrated (Zebker et al., 1986), in the airborne NASA CV990 system, the aircraft elevation ranges from 8×10^3 to 14×10^3 m , and the incidence angle was 25°~ 55°, when the distance ρ was 8.8×10^3 m up to 24.4×10^3 m, since $\delta\rho < B = 11$m , therefore gives $\delta\rho \ll \rho$. Another example with regard to satellite-borne SAR ERS-1/2 was provided (Li, 2005): the ρ is about 8×10^5 m, $\delta\rho < B \approx 1 \times 10^3$ m, also gives $\delta\rho \ll \rho$.

As a result, equation (2.3.3) is rearranged to:

$$\delta\rho = \frac{B^2}{2\rho} - B\sin(\theta - \alpha) \quad (2.3.4)$$

When $B\sin(\theta - \alpha)$ is $B_{\parallel}$ and the term $\frac{B^2}{2\rho}$ considered negligible (Zebker et al., 1986) is usually be ignored, then:

$$\delta\rho = -B\sin(\theta - \alpha) \quad (2.3.5)$$

Substituting equation (2.3.5) into equation (2.3.1), then:

$$\phi = -\frac{4\pi}{\lambda} B\sin(\theta - \alpha) \quad (2.3.6)$$

This is the function can be used in practice.

2.3.2 InSAR Processing Flow

Normally, InSAR processing starts from either raw data or SLC data. In case of starting from raw data, the first step is SLC (Single Look Complex) image generation by focusing techniques. A popular one is range Doppler algorithm including range compression, range migration correction and azimuth compression steps.

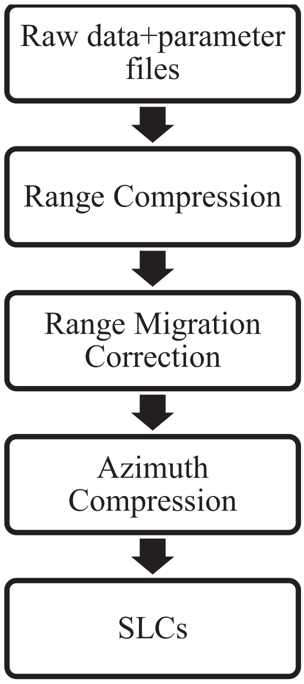

Figure 2.7 Range-Doppler processing.

In other cases, SLC images are used for interferogram generation. Several steps are generally indispensable in such a processing chain.

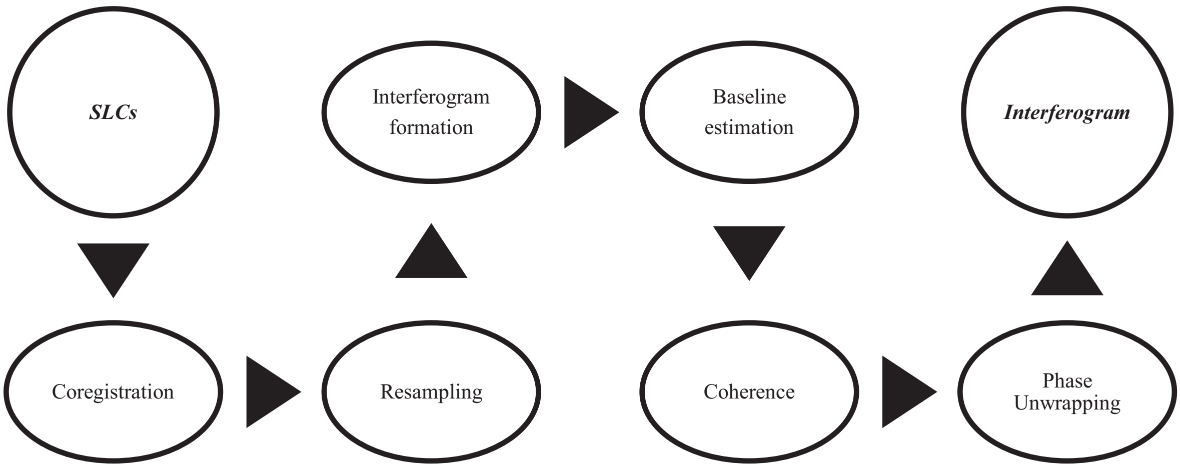

Figure 2.8 Basic InSAR processing.

Parameters of two SAR images always vary from two acquisitions. For instance, the look angles will be a little bit difference. Furthermore, scattering features will be different as well due to the time and different look angles. The coregistration aims to map the slave pixels in the reference, so-called master image. One approach is to estimate both range and azimuth offsets between master and slave images. In this approach, coarse offsets are obtained in both range and azimuth directions. Consequently, based on the coarse coregistration, a so-called fine coregistration will be carried out to get sub-pixel accurate offsets.

Based on the coregistration results determined from the previous step, an interpolation kernel is applied to resample the slave image. Two features are considered when people make choice of kernel function: the accuracy and the computational time. Hanssen and Bamler (1999) concluded that a 6-point cubic convolution is a good trade-off.

After resampling, master and slave images are on the same grid and can be used to form the interferogram. By multiplying pixels from one SAR image with the conjugate of those from the other, the interferogram is formed.

$$I = MS^{*} \tag{2.3.7}$$

where I is the complex interferogram, M is the complex reference image (master), S is the complex slave image, and the asterisk means conjugation.

In fact, the master and slave images are complex arrays of values identically sized (Leighton, 2010). Therefore, if talking about each pixel, equation (2.3.7) can be rearranged:

$$I(x.y) = M(x,y)S^{*}(x,y) \tag{2.3.8}$$

where $\mathrm{I}(\mathrm{x},\mathrm{y})$ is the pixel value at (x,y) in the interfergram, $\mathrm{M}(\mathrm{x},\mathrm{y})$ is the master pixel value at (x,y) and $\mathrm{S}^{*}(\mathrm{x},\mathrm{y})$ is the conjugate of slave pixel value at (x,y).

Figure 2.9 is an interferogram constructed by two ENVISAT SAR images which cover Xishan coal mine in Shanxi province, China. Each periodic colour cycle, which is usually called fringe, denotes the phase modulo 2π. This images shows the fringes appears quite frequently in range direction. This is mainly due to the effect of natural increase in distance between the SAR and the image, which can be removed by using an ellipsoidal Earth model such as the WGS84 ellipsoid (Warren, 2007). Usually, this removing process is called interferogram flattening (Figure 2.9).

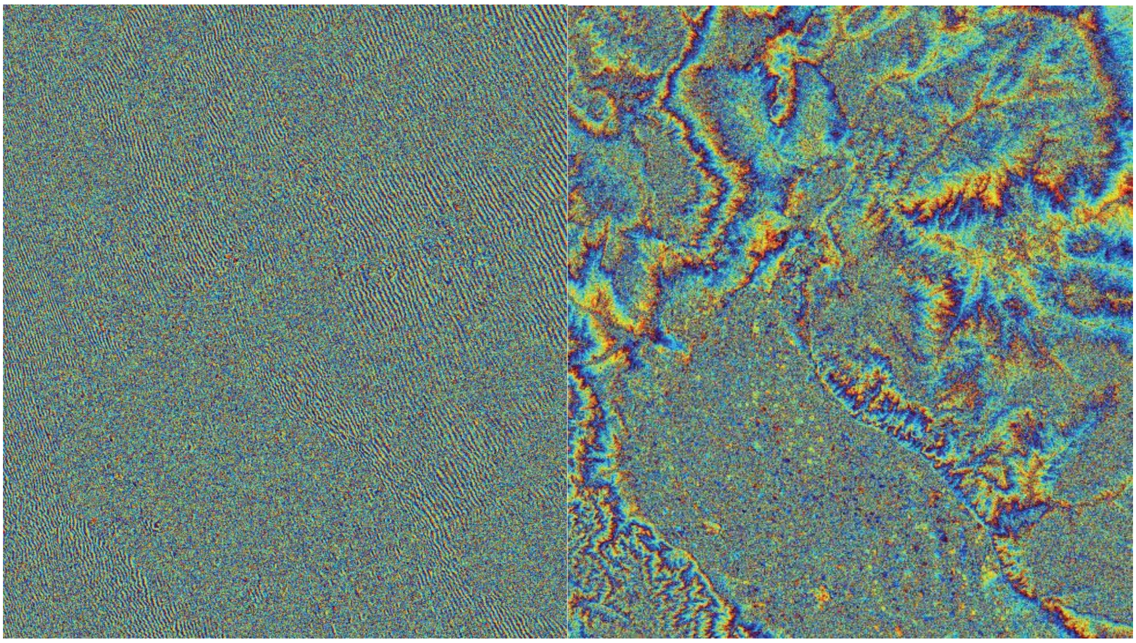

Figure 2.9 Left: Interferogram of Xishan area. Right: Flatened interferogram.

ENVISAT images from 13 Jan, 2008, and 17 May, 2009.

The estimation of the interferometric baseline, or in other words, knowledge of satellite positions is obvious important. Interferometric baseline is used for flattening progress, which removes the phase component introduced by the ellipsoidal Earth. In this step, precise estimation of baseline plays a significant role to improve the interferogram product. A comparison (Li, 2005) between orbits provided by German Processing and Archiving Facility (D-PAF) and by the Delft Institute for Earth-Oriented Space Research (DEOS) for ERS-2 interferogram shows up to 2~3 fringes differences. The accuracy of D-PAF provided orbit is around 8~10 cm when that of Delft orbit is about 5~7 cm (Scharroo and Visser, 1998).

Coherence estimation is a useful process as it provides an evaluation of the reliability of the phase values (Zebker and Villesenor, 1992). The coherence is a measure of the correlation between two SAR images:

$$\gamma_{MS} = \left| \frac{<MS^{*2}>}{\sqrt{<|M|^2><|S|^2>}} \right| \tag{2.3.9}$$

where γ_{MS} is the coherence, M and S are the complex pixel values for the master and slave images, <> means the average over a neighbourhood.

γ_{MS} values range from 0 to 1 where value 0 means there is no coherence and 1 means perfect coherence. High coherence always tends to urban area gives more confidence in the phase value. On the contrary, low coherence is often due to water, vegetation or rapid changes of scatterer properties between SAR acquisitions. For example in Figure 2.10, most areas are in low coherence as this is a mountainous area with vegetations. Some brightness parts only appear in the town (centre of the image).

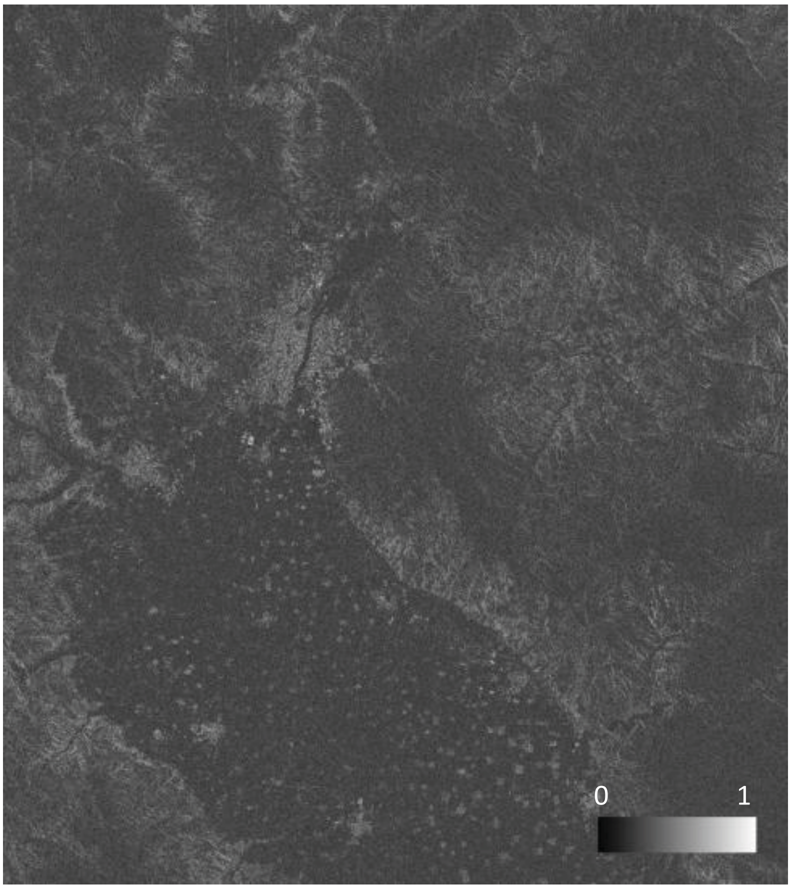

Figure 2.10 Coherence map in Xishan area. By ENVISAT images from 13 Jan, 2008, and 17 May, 2009.

Usually, there are two main kinds of de-correlation in interferograms, which are temporal de-correlation and geometric de-correlation (Warren, 2007). By using SAR images with shot temporal baselines, temporal de-correlation can be reduced. During short time, scatterer characteristics will change relative little. But for larger time periods those will be difference. For example vegetation grows and changes the scattering characteristics a lot in nor-urban area.

In order to minimise geometric de-correlation, people can select SAR images with small geometric baselines only. As (Li and Goldstein, 1990) pointed out that along with the baseline between the SAR images increases, the look angles of the SAR differ by more, and consequently the scattering in the resolution cell will differs more.

Phase unwrapping is essential if the absolute interferometric phase are needed. As we know, the phase in SAR signals are only able to be measured modulo 2π. Technically speaking, an integer number of 2π should be added to obtain the phase in reality. There are two main approaches for phase unwrapping which are residue-based algorithms and least squares algorithms proposed by (Goldstein et al., 1988) and (Zebker and Lu, 1998) respectively. After setting a start point, gradients between each adjacent pixel are computed and integrated along a path defined. Therefore, phase values are all relative to the start point in the interferogram. Phase unwrapping is a specific topic and people would refer to relevant literature.

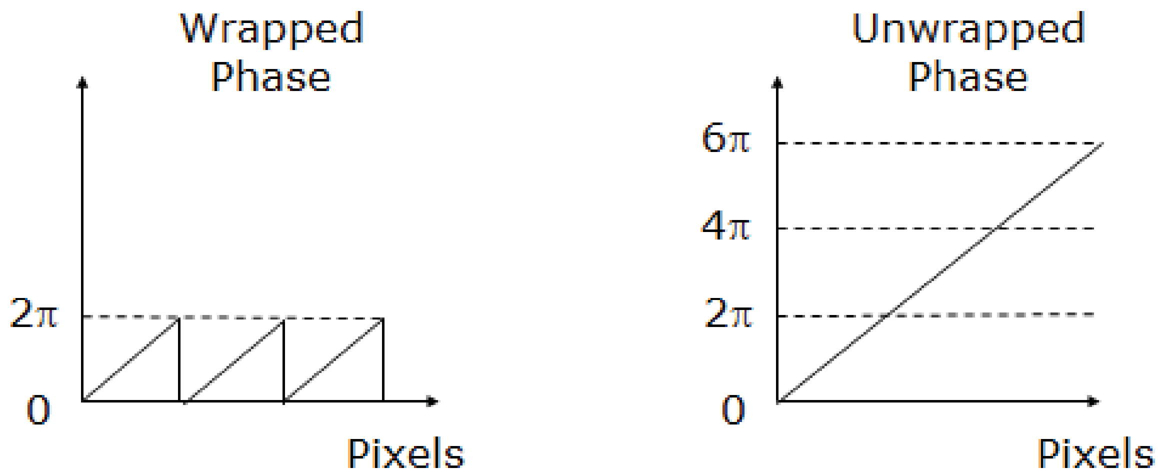

Figure 2.11 Simplified process of phase unwrapping.

Generally speaking, an interferogram is produced based on steps above. Apart from those, filtering, baseline refinement, multilooking, and so on can be done in an InSAR processing as well.

2.4 DInSAR

2.4.1 DInSAR approaches

Differential interferometric synthetic aperture radar (DInSAR) is a technique based on InSAR. DInSAR is an appropriate method for sudden and large deformations (Liu et al., 2012). It removes the topographic phase with the help of an external Digital Elevation Model (DEM) (2-DInSAR) like shown in Figure 2.12 or another interferogram (3-DInSAR or 4-DInSAR), which leaves the phase component related to the land movements between the two image dates. In recent years, worldwide and high resolution DEM becomes available so that two-pass DInSAR has some advantages nowadays (Leighton, 2010). For example, the atmospheric phase error in the topographic interferogram is eliminated, and people don’t need to worry about any unknown deformation contaminating the topographic interferogram. Three-pass method developed by Zebker in 1994 showed good agreement with two-pass results.

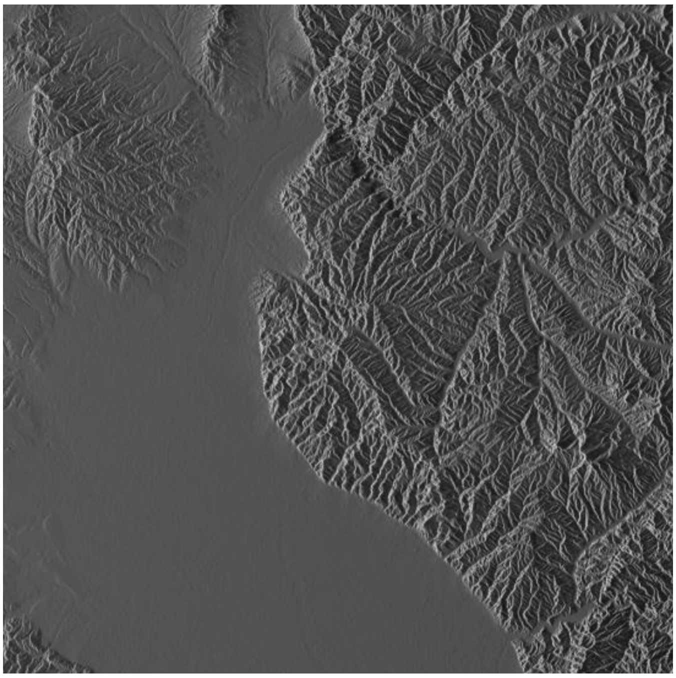

Figure 2.12 Simulated amplitude from SRTM DEM.

Similar to three-pass, another multi-pass DInSAR technique is four-pass. Four SAR images are needed to form two interferograms, respectively. One key step in this approach different with two-pass or three-pass is to coregistration of two interferograms, as there is no common image in the two interferograms. This approach is always used when datasets are not good for three-pass DInSAR.

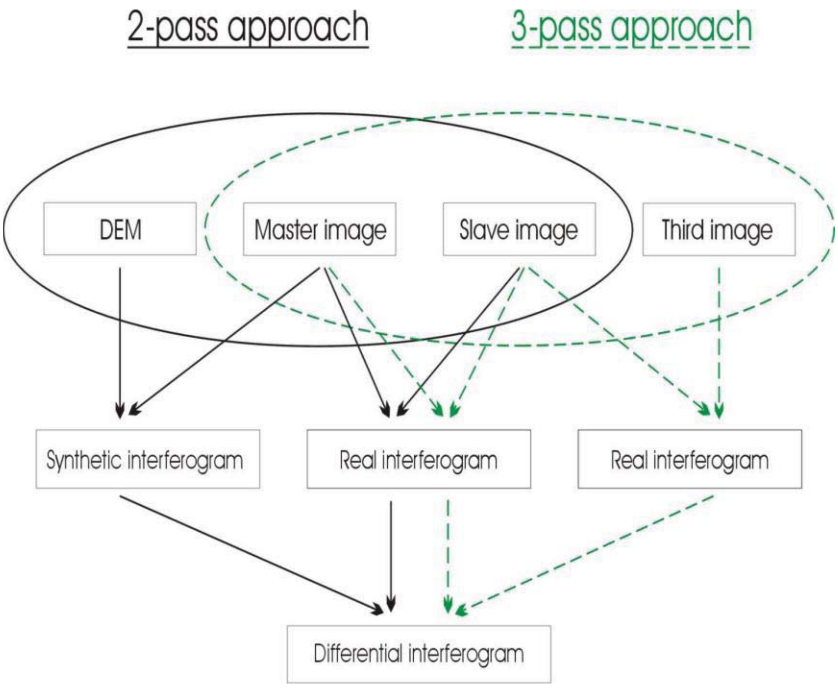

Figure 2.13 Flow chart of 2-pass and 3-pass DInSAR (Riedel and Walther, 2008).

DInSAR in theory has some limitations to contend with. There are multiple sources of noise in DInSAR and all of them will be propagated into the interferometric phase. But the largest one is the atmosphere which sometimes even will swamp the deformation signal (Hanssen, 1998). Consequently, in the case of three-pass or four-pass DInSAR, this effect increases because more interferograms are used means more atmospheric effects will be introduced.

Besides, for two-pass DInSAR, there is an additional DEM error which requires the high accurate DEM to be used.

2.4.2 SRTM DEM

Due to its good resolution and worldwide availability, The 90 m resolution Shuttle Radar Topography Mission (SRTM) DEM was used in this study. The Shuttle Radar Topography Mission was a joint project carried out by the National Aeronautics and Space Administration (NASA), the National Geospatial Intelligence Agency (NGA) of the Department of Defense (DoD) of U.S (Farr et al., 2007). Besides, Deutschen Zentrums für Luft- und Raumfahrt (DLR) is involved. The aim of SRTM project was to produce Digital Elevation Model (DEM) of all land between 60° north and 56° south latitude, which means about 80% of Earth's land surface. This model is sampled over a 1-arc-second grid. As evaluated (Farr and Kobrick, 2007), the accuracy of this elevation model is less than 7 meters in vertical direction. Following is an example of SRTM DEM with 90 m resolution.

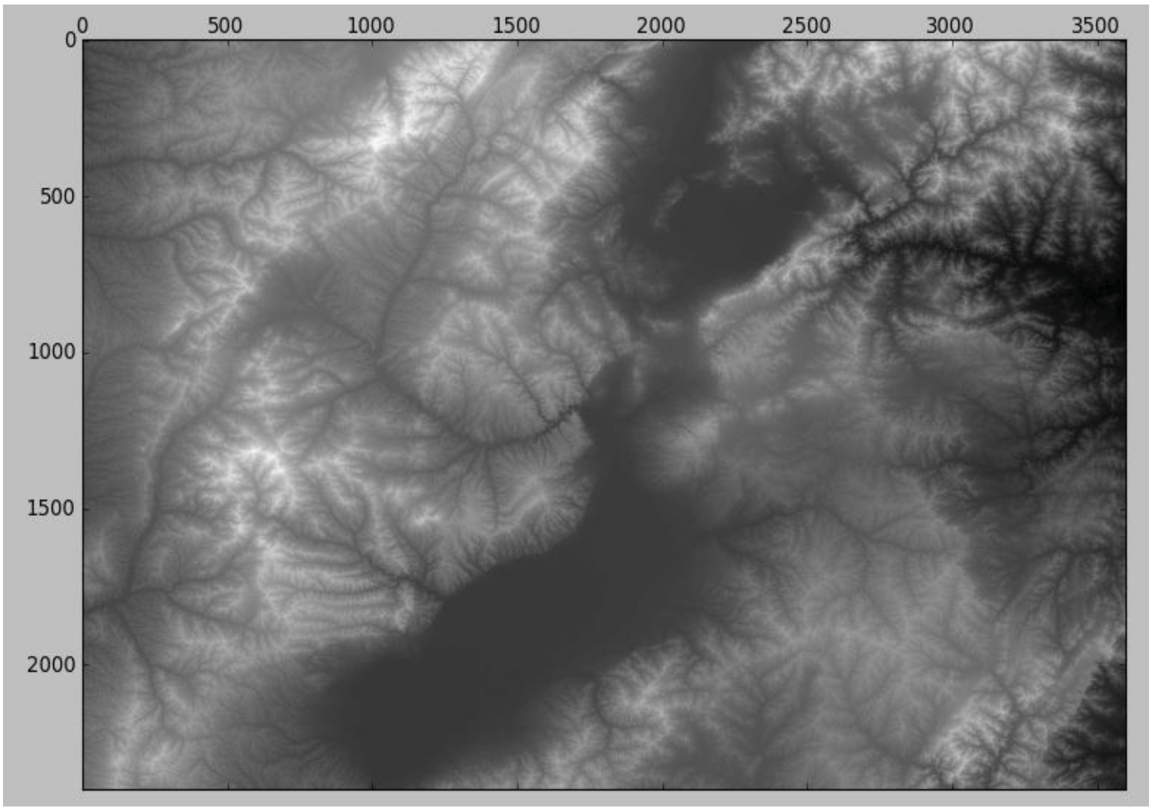

Figure 2.14 SRTM DEM of Xishan area.

The latitude of the upper left corner is 39° north and 111° east. One has to be taken care of is there is missing data in the DEM, which is indicated by a value -32,768. Interpolation has been used to fill in such holes.

2.5 Persistent Scatterer Interferometry

Persistent Scatterer Interferometry (PSI) is the extension of conventional InSAR, and was proposed by (Ferretti et al., 1999, Ferretti et al., 2000) firstly. PSI aims at addressing the influences of de-correlation and atmospheric delay in InSAR processing (Agram, 2010). PSI investigates the characteristics of all phase stable points on a succession of time-ordered SAR images. Such points with stable phase temporally are so-called PS points that with dominant scatterers in the resolution cells (Fig. 2.15).

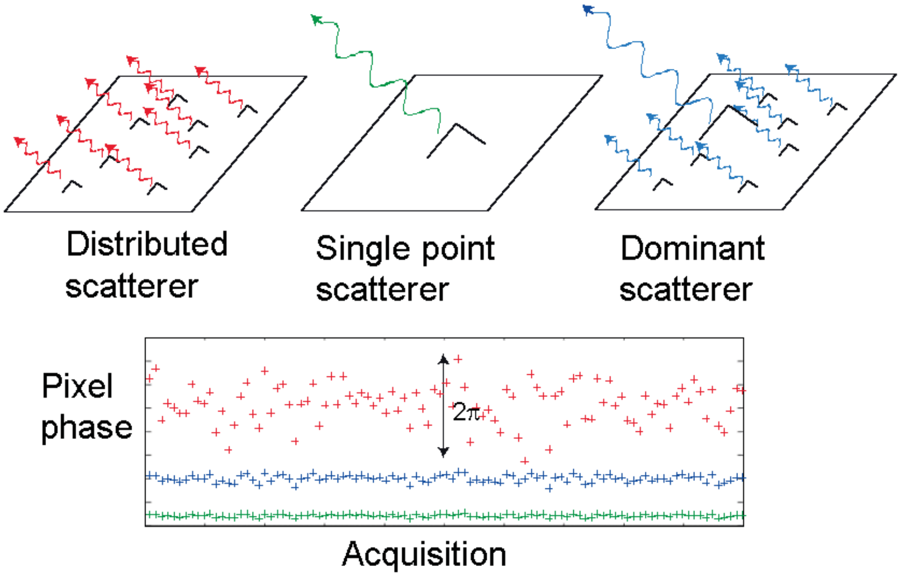

Figure 2.15 Scattering mechanism models for a SAR resolution element (Agram, 2010).

When only distributed scatterers are available in a resolution cell, it is not a PS point (in red case). Scatterers in the cell are with similar strength so that the interferometric phases are randomly distributed. An ideal case is shown in green color in which only single point scatterer locates in the cell. Such kind of scatterers doesn't exist in reality. The resolution element has dominant scatterers is PS point and much smaller phase variation is exhibited in this pixel than that in the distributed scattering pixel (Agram, 2010). Several PSI approaches have been developed in the past years. For instance, Small BAseline Subset (SBAS), the Coherent Pixel Technique (CPT), Stanford Method (StaMPS), Persistent Scatter Paris (PSP) and so on. SBAS and StaMPS will be described briefly as they were used often in this study. SBAS (Small BAseline Subset) method, forms many interferograms with short baselines and derives movements with time (Berardino et al., 2002). Singular Value Decomposition (SVD) is used to connect independent unwrapped interferograms in time, when a least square adjustment is used for estimating the temporal low-pass component of the DEM refinements and deformation signal. Finally, temporal high-pass and spatial low-pass are carried out since the DEM refinements and deformation signal have been removed. The SBAS approach is extended (Lanari et al., 2004) to extend the results with limited spatial resolution caused by multi-looking to 'full resolution' products.

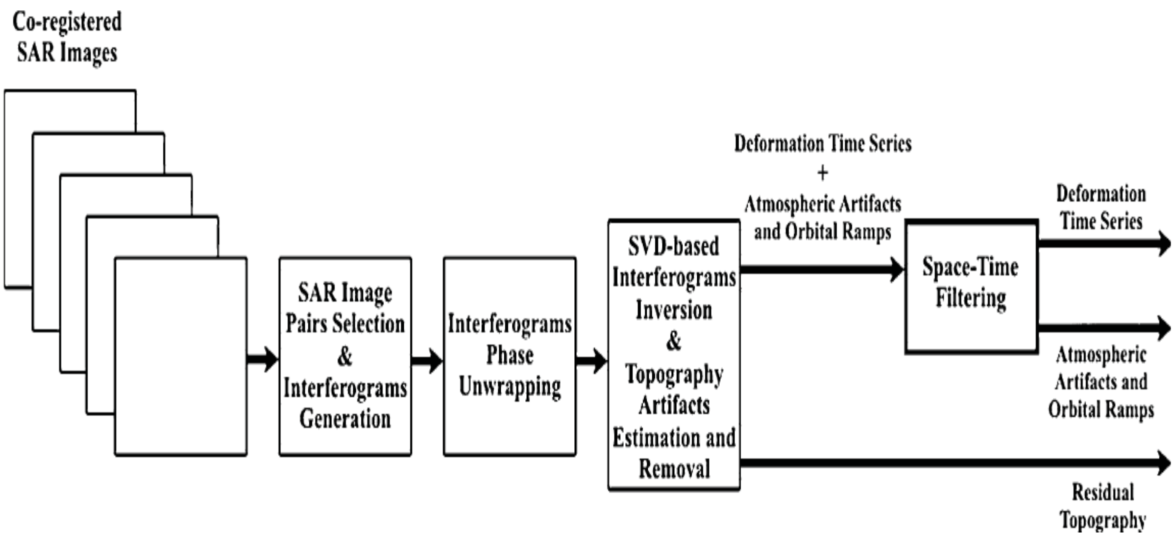

Figure 2.16 Block Diagram for SBAS algorithm (Lanari et al., 2007).

The deformation signal is derived from a combination of all small spatial baseline interferograms, in which multiple master images are used. By only using interferograms with short temporal baselines, Small Temporal BAseline Subset (STBAS) is proposed and it is actually a modification to the SBAS algorithm (Hong et al., 2010). It is suggested (Osmanoglu, 2011) that, in SBAS processing baseline parameters can be set to 25% of the critical baseline (about 400m), and around 1 year for temporal baseline, if the aim is deformation analysis.

StaMPS is the abbreviation of Stanford Method for Persistent Scatterers implemented by (Hooper et al., 2004, Hooper, 2006). In contrast to the former PSI method, StaMPS has shown its strong ability for application to non-urban areas (Hooper et al., 2007). Subsequently, an extended version (Hooper et al., 2008) which is called StaMPS/MTI (Multi-Temporal InSAR) includes a small baseline method, and a MTI method which combined both PS and SBAS methods.

Two start points are available in the PS/MTI processing. The first one is to start with the raw data by calling ROI_PAC (Repeat Orbit Interferometry Package) developed at JPL/Caltec. ROI_PAC was written in C and Fortran programming languages and could be controlled by Perl scripts. The second is from single-look complex (SLC) images. Images are imported directly into DORIS (Delft Object-oriented Radar Interferometric Software) and used to form interferograms. DORIS was developed by the Delft Institute of Earth Observation and Space Systems (DEOS), Delft University of Technology (Kampes et al., 2003). Nowadays, the first case is supported when using ERS, ENVISAT and ALOS data (level 0 data). The second case is possible for ERS, ENVISAT, RADARSAT-1 and TerraSAR-X data (SLCs). The processing of StaMPS can be divided into three parts: interferogram generation (by ROI_PAC or DORIS), PS identification (selection), Filtering and phase unwrapping (displacement estimation).

As (Sousa, 2009) presented in Fig. 2.17, StaMPS selects the master scene that minimizes the sum de-correlation. Generally, four terms are considered during this selection. They are temporal baseline, spatial perpendicular baseline, Doppler centroid baseline and thermal noise. Persistent scatterer identification in StaMPS is quite different from other PSI methods in which analysis of pixel amplitude variability is applied. StaMPS estimates the PS probability for each pixel in the stack of interferograms by the combination of amplitude and phase analysis (Hooper, 2006). Firstly, amplitude is analysed to obtain PS candidates. Secondly, with the help of phase analysis, the PS probalility of all candidate pixels are estimated. After that, the pixels with high amplitude dispersion and dropped in the first step will be estimated again.

The interferometric phase of a pixel in a differential interferogram can be represented (Hooper et al., 2004) by:

$$\emptyset_{\mathrm{int,x,i}} = \emptyset_{\mathrm{def,x,i}} + \emptyset_{\epsilon,\mathrm{x,i}} + \emptyset_{\mathrm{atm,x,i}} + \emptyset_{\mathrm{orb,x,i}} + \emptyset_{\mathrm{n,x,i}} \tag{2.5.1}$$

where $\emptyset_{\mathrm{int,x,i}}$ is the interferometric phase of the xth pixel in the ith interferogram, $\emptyset_{\mathrm{def,x,i}}$ is the phase change due to the deformation, $\emptyset_{\epsilon,\mathrm{x,i}}$ is the residual phase due to DEM error, $\emptyset_{\mathrm{atm,x,i}}$ is the phase difference due to atmospheric delay between acquisitions, $\emptyset_{\mathrm{n,x,i}}$ is the noise term (thermal noise, coregistration errors and so on). PS points are identified when the $\emptyset_{\mathrm{n,x,i}}$ part is subtle to be accepted.

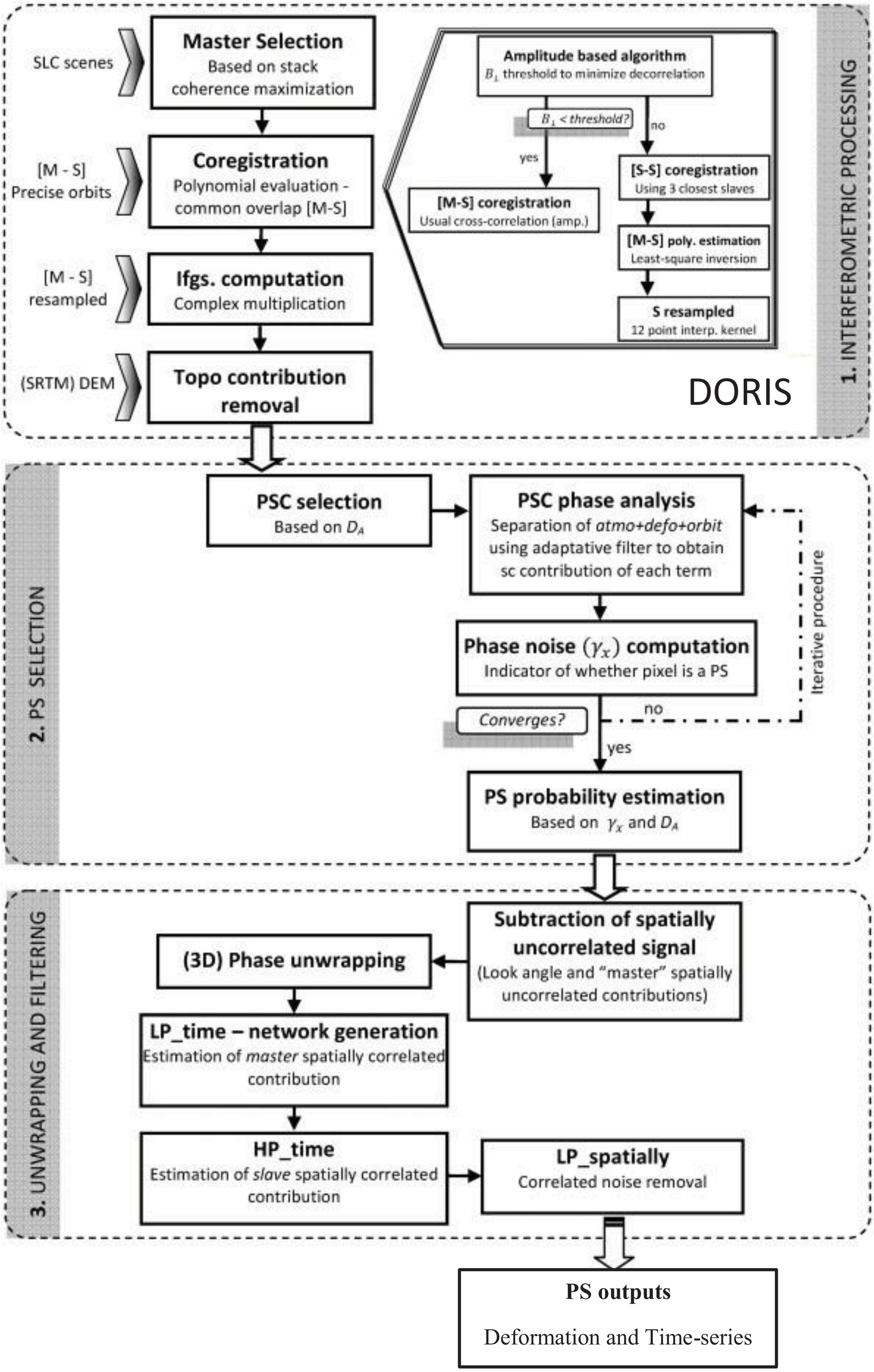

Figure 2.17 Flow chart of StaMPS processing (Sousa, 2009).

Following, the spectral characteristics assumed for each of the phase components is shown (Hooper, 2006, Agram, 2010) in Table 2.1.

Once the PS points are selected, StaMPS will isolate the deformation signal from these phase parts above in each pixel. StaMPS implemented a band-pass filter to estimate the spatially correlated components. Apparently, atmosphere and orbital errors are not able to be distinguished because they have similar characteristics in both spatial and temporal domains. More detailed materials would refer to (Hooper, 2006).

Table 2.1 spectral characteristics for phase componets of a pixel observed in the interferogram (Hooper, 2006, Argam, 2010).

	Component	Spatial Properties	Temporal Properties
$\phi_{defo,x,i}$	Deformation	Low freq	Low freq
$\phi_{atm,x,i}$	Atmosphere	Low freq	High freq
$\Delta\phi_{orb,x,i}$	Orbital errors	Low freq	High freq
$\phi_{n,x,i}$	Scatterer noise	High freq	High freq
$\phi_{\epsilon,x,i}$	DEM Error	High freq	Correlated with baseline

The accuracy of the PSI technique depends on the spatial and temporal baselines, the sensor and so on. As Adam et al. presented in 2009, the accuracy of PSI could be better than 1 mm/year, in the case where the deformation is linear. The SBAS technique has a comparable accuracy.

The advantage of the use of PSI and SBAS methods is that the deformation of many thousands of points over a scene can be determined very quickly and at very low cost when compared to the effort needed to perform a ground survey of points at the same density (Liu et al., 2012). PSI and SBAS methods can be applied to whole cities or regions at a time and are able to report on deformation due to local and man-made geological causes, as well as the deformation of individual buildings that may be due to settlement or thermal expansion, for example. On the other hand, PSI approach requires a stack of SAR images that are not always available. One has to note that there is a prerequisite for PSI: persistent scatterers are available and selected after evaluation of amplitude and phase stability.

2.6 GPS System

GPS is a satellite navigation system that developed by the U. S. Department of Defense (DOD) in 1970s. Originally, 24 satellites were designed but new satellites are always in progress. Until December of 2012, totally 32 satellites are in GPS constellation. These satellites are at the altitude of 20,000 km above the Earth and distributes in 6 orbital planes. The 6 orbital planes' inclination is approximately 55° (tilt relative to Earth's equator) and are arranged to make sure that at least 6 satellites are always visible from everywhere on the Earth. The orbital period is around 11 hours and 58 minutes. GPS system broadcasts coded satellite signals that can be received and processed by GPS receivers. Position (in three dimension), velocity (in north, east and up directions) and time in UTC (Universal Time Coordinated) are provided to users.

GPS system consists of three segments:

- The space segment: The operational satellite constellation (now 32 satellites) transmitting signals.
- The control segment: Ground-based control stations distribute in Colorado Springs (Master Control Station), Ascension Island, Cape Canaveral, Diego Garcia and Hawaii, Kwajalein. The main tasks are satellite tracking, orbit computations. This information is gathered in the Master Control Station (MCS) and then passed to the satellites. Hence, the satellites can transmit the so-called ephemeris in the navigation messages modulated on L1 carrier wave.
- The user segment: All equipment and techniques on the ground for scientific and commercial users.

The GPS satellite signal is a combination of the three components: navigation message, carrier wave and ranging codes. GPS system transmits two L-band carrier signals L1 and L2, when the frequency of L1=1575.42 MHz, and L2=1227.6 MHz. The carrier waves are modulated with two kinds of codes, as well as the navigation messages. The two distinct GPS ranging codes are the Coarse Acquisition (C/A) code which is modulated onto L1 and the Precise (P) code which is modulated onto both L1 and L2. The P code was designed for the military and other authorised users only.

Two types of measurements are available by using GPS signals in this system.

- The pseudo-range observable
- The carrier phase observable

2.6.1 The Pseudo-Range measurement

In principle, a code is generated in the satellite and receiver simultaneously. The coded is send by the satellite and received by the receiver. Then the difference between the received code and the generated code in the receiver can be calculated. This difference is in proportion to the distance between the satellite and receiver and called Pseudo-Range (PR). Normally, the receiver's time is less accurate than the satellite's as the receiver clock does not have comparable quality with satellite clock. If we define the explicit time frames of a receiver (τ), a satellite (t), and the GPS system time (T), then the observational equation can be derived (Bingley, 2008):

$$T = t + \delta t \qquad (2.6.1.1)$$

$$T = \tau + \delta\tau \qquad (2.6.1.2)$$

where $\delta\tau$ and δt are receiver clock and the satellite clock offsets respectively.

Above are the relationships among the receiver time, the satellite time, and the system time.

If we multiply the difference between the time of reception τ_r (in receiver time frame) and the time of transmission t^s (the satellite time frame) by the speed of the light (c) in vacuo, the pseudo-range is:

$$PR_r^s = c(\tau_r - t^s) \qquad (2.6.1.3)$$

And the true range ρ is the difference between the time of reception in GPS system time frame T_r and the time of transmission in the system time frame T^s by the speed of the light (c) in vacuo:

$$\rho_r^s = c(T_r - T^s) \qquad (2.6.1.4)$$

Equation (2.6.1.4) could be expressed by combining (2.6.1.1) and (2.6.1.2):

$$\rho_r^s = c((\tau_r + \delta\tau_r) - (t^s + \delta t^s)) \qquad (2.6.1.5)$$

And then gives:

$$\rho_r^s = c(\tau_r - t^s) - c(\delta\tau_r - \delta t^s) \qquad (2.6.1.6)$$

Substituting equation (2.6.1.3) into equation (2.6.1.6) gives:

$$PR_r^s = \rho_r^s - c(\delta\tau_r - \delta t^s) \qquad (2.6.1.7)$$

Then we add defined time frames into equation (2.6.1.7):

$$PR_r^s(\tau_r) = \rho_r^s(T^s, T_r) - c(\delta\tau_r(\tau_r) - \delta t^s(t^s)) \tag{2.6.1.8}$$

In addition, other terms should be included, such as the ionospheric and tropospheric delay ($dion_r^s$ and $dtrop_r^s$), a satellites' ephemeris $deph_r^s$, and the residual v_r^s. Finally, the expression of pseudo-range measurements is:

$$PR_r^s(\tau_r) = \rho_r^s(T^s, T_r) - c\big(\delta\tau_r(\tau_r) - \delta t^s(t^s)\big) + deph_r^s + dion_r^s + dtrop_r^s + v_r^s \tag{2.6.1.9}$$

2.6.2 The Carrier Phase measurement

Comparing to the pseudo-ranges measurements, carrier phase offers more precise observations. Because the resolution of carrier waves is several decimetres when that of codes is 30 meters (P code) or 300 meters (C/A code). The carrier phase observed between the satellite and the receiver consists of an integer ambiguity part (a number of cycles) and the fractional part of the wavelength.

By modifying the PR observable equation, the basic carrier phase equation is rearranged:

$$\phi_r^s(\tau_r) = \frac{f}{c}\rho_r^s(T^s, T_r) - f\big(\delta\tau_r(\tau_r) - \delta t^s(t^s)\big) + N_r^s \tag{2.6.2.1}$$

where $\phi_r^s(\tau_r)$ is the carrier phase observable, N_r^s is the integer ambiguity, f is the frequency.

The full equation of carrier phase observable is formed by adding the error terms:

$$\phi_r^s(\tau_r) = \frac{f}{c}\rho_r^s(T^s, T_r) - f\big(\delta\tau_r(\tau_r) - \delta t^s(t^s)\big) + N_r^s + \frac{f}{c}deph_r^s - \frac{f}{c}dion_r^s + \frac{f}{c}dtrop_r^s + \frac{f}{c}v_r^s \tag{2.6.2.2}$$

The term of $\frac{f}{c}dion_r^s$ is negative because the carrier wave is advanced by the ionosphere.

2.7 PPP

Precise point positioning (PPP) is a GNSS positioning technique processing both un-differenced carrier-phase and pseudo-range measurements brought from a single receiver by fixing known satellite orbits and clocks of centimeter-level accuracy (Zumberge et al. 1997). These high accurate clock and orbit data are provided by global GNSS networks such as the International GNSS Service (IGS). The main difference between relative positioning and PPP is how to deal with the clocks and ambiguity modelling (Leighton, 2010), from a theoretical point of view. In relative positioning, the clock biases and the ambiguity are eliminated by differencing. However, in PPP, those are considered as unknows and estimated by applying a stochastic model and then filters, for example, the Square-Root Information Filter (SRIF).

In PPP processing, $\delta t^s(t^s)$ and $deph_r^s$ are removed by using high precision orbit and clock products. The ionospheric advance can be eliminated using dual frequency receiver. The ionospheric irregularities can be removed using a model included in the orbit products (Feltens and Schaer, 1998). Besides, the hydrostatic tropospheric delay is predictable and the wet delay is estimated as unknown with mapping functions.

Thus, the PPP observable model is derived by (Kouba, 2009):

$$PR_r^s(\tau_r) = \rho_r^s(T^s, T_r) - c\delta\tau_r(\tau_r) + MZPD_r^s + v_r^s$$

(Pseudo-Range) (2.7.1)

$$\phi_r^s(\tau_r) = \frac{f}{c}\rho_r^s(T^s, T_r) - f\delta\tau_r(\tau_r) + N_r^s + \frac{f}{c}MZPD + \frac{f}{c}v_r^s$$

(Carrier Phase) (2.7.2)

where M is the mapping function, ZPD is the zenith path delay.

PPP technique has several advantages:

- PPP does not need any reference stations before the positioning or surveying, which makes the work much simpler.
- PPP is able to provide precise positioning produces (Table 2.2) on a global scale. PPP would work even in open oceans (Geng et al., 2010).
- PPP estimates several unknowns accurately which may be useful for other fields. For example, ZWD products could be of interests to meteorology.

Table 2.2 RMS of the differences between PPP results and ground truths (Geng, 2010).

Measurements	Mode	RMS (cm)		
		East	North	Up
Dual-frequency	Daily static	<0.5	<0.5	<1.0
	Hourly static	~4.0	~2.0	~3.0
	Post-processing kinematic	~5.0	~4.0	~10.0
	Real-time kinematic	<10.0	<10.0	<20.0
Single-frequency	Post-processing kinematic	~25.0	~25.0	~50.0
	Real-time kinematic	~40.0	~40.0	~50.0

2.8 Summary

In this chapter, radar history and radar techniques with regard to geodesy have been reviewed. The fundamental of InSAR, DInSAR were briefly presented followed by the more advanced InSAR technique PSI/SBAS. Besides, GPS system and PPP processing were reviewed, as relevant technique is going to be employed in this study.

Chapter 3 Study of Atmospheric Effects

3.1 Introduction to the Atmosphere

3.1.1 Component of the atmosphere

Atmosphere of our earth is made up of different gases, such as Nitrogen, Oxygen, Argon, and so forth. The major gas components which have various physical properties are shown below (Lutgens and Tarbuck, 2001).

Table 3.1 Composition of the atmosphere (Li, 2005).

Constituent	Symbol	Percent by volume
Nitrogen	N_2	78.084
Oxygen	O_2	20.946
Argon	Ar	0.934
Carbon dioxide	CO_2	0.037
Neon	Ne	0.00182
Helium	He	0.000524
Methane	CH_4	0.00015
Krypton	Kr	0.000114
Hydrogen	H_2	0.00005
Water vapour	H_2O	0-4
Aerosols		0.000001

More than 99% of the volume of dry air (clean) consists of two gases, nitrogen and oxygen. The inert gas argon and several other gases take up the remaining 1% of dry air. However, the composition of the atmosphere is not keeping the same. In fact, it is changing from place to place, and from time to time. It is presented (Ahrens, 2000; Lutgens and Tarbuck, 2001) that the CO_2 concentration measured at Hawaii's Mauna Loa Observatory had risen more than 15% since 1958. Another good example is water vapour, which may arise to 4% of the Earth's atmosphere in warm tropical areas while decrease to a fraction of one percent in cold arctic area (Li, 2005). Besides of dry air and water vapour, there are liquid and solid particles such as hydrometeors in the atmosphere as well.

3.1.2 Structure of the atmosphere

Atmosphere is horizontally stratified, because of the Earth's gravity. Here is a general description of atmosphere (Fig. 3.1) taken from Aspen Global Change Institute (AGCI).

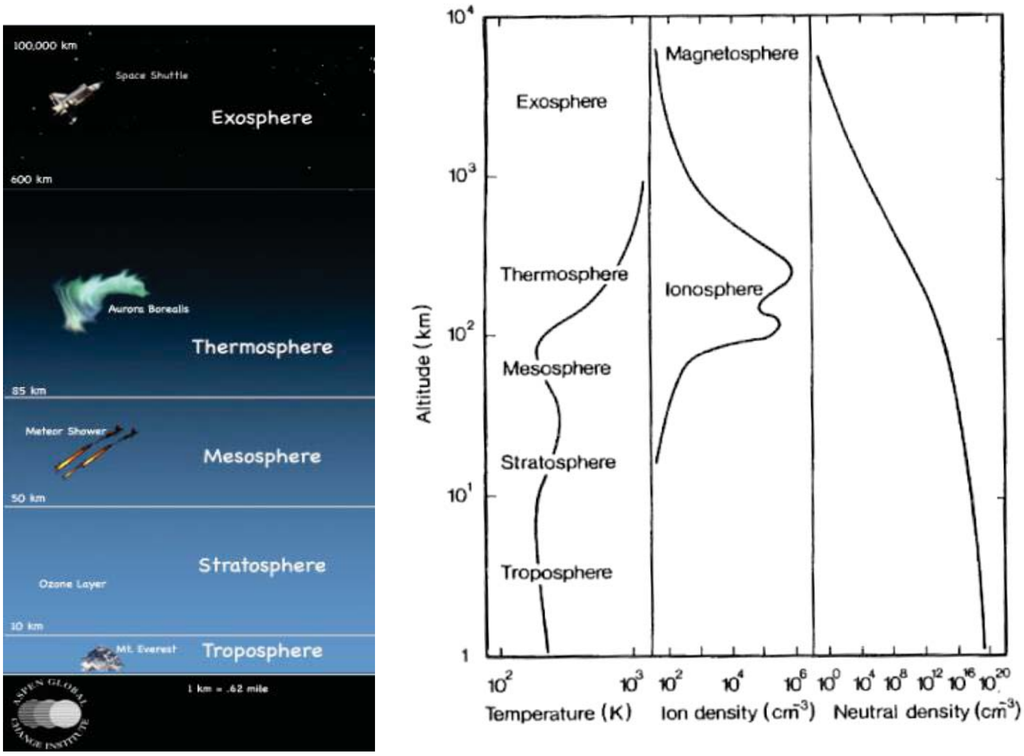

Figure 3.1 Left: Structure of the atmosphere (Adapted from AGCI). Right: Schematic representation of the atmosphere (Rees, 1989).

Normally, people divide atmosphere into troposphere, stratosphere, mesosphere, thermosphere and exosphere, by its temperature profile.

The troposphere locates on the bottom, where the temperature decreases with altitude. Normally, the air temperature decreases 6.5°C per kilometre (so-called temperature lapse rate). The average depth of the troposphere is approximately 12 km. It is deeper in the tropics, up to 16 km, and shallower in the polar region, at 9 km or less. The troposphere contains 80% of the atmosphere's mass and 99% of its water vapour and aerosols. Therefore, all of the weather phenomenons occur in the troposphere. The top of the troposphere is called tropopause, which is a temperature inversion.

The layer above the troposphere is stratosphere. The temperature in stratosphere increases with altitude and reaches about 0°C at 50 km height, where is the top of stratosphere. Most of ozone is in the stratosphere and it is affected by ultraviolet (UV) and increase the temperature. About 19% mass of the Earth’s atmosphere is in this layer.

Above the stratosphere is mesosphere, where the temperature again decreases with height. The top of mesosphere is located about 85 km above the Earth’s surface. It is called mesopause, where the temperature decreases to about -90°C.

Above the mesopause is the thermosphere. The temperature increases with altitude and may reach to 1500°C because Oxygen molecules absorb energetic solar rays and make the atmosphere quite hot. Aurora happens in this layer.

Above 600 km height of the Earth’s surface, there is exosphere. In fact, it is hard to separate exosphere from thermosphere exactly, because the boundary between exosphere and thermosphere is vague. Molecules in the exosphere will escape the Earth’s gravity and fly to the space if they have enough energy. Space shuttles fly in this area.

On the other hand, the atmosphere can also be divided into ionosphere and plasmasphere or magnetosphere according to electrical properties (Rees, 1989). From Rees’ figure, the thermosphere and a part of mesosphere are overlapping to the ionosphere. In fact, ionosphere extends from 50 km height to 1500 km height above the Earth's surface. There are a lot of ions, which are atoms or molecules have got or lost electrons, and free electrons in ionosphere. Ionosphere can be divided into D (80~90 km), E (90~140 km), F1 (140~200 km) and F2 (200~1000 km) layers with different properties of free electrons. Neutral atmosphere, which means non-ionised, has two components. One is the stratosphere when the other is troposphere.

Table 3.2 Layers in the ionosphere (adapted from Odijk, 2002 and Li, 2005).

Layer	Height	Electron density [m^{-3}], Day	Electron density [m^{-3}], Night
D	80~90 km	10^{10}	• (Disappear)
E	90~140 km	10^{11}	$5\cdot10^{9}$
F_1	140~200 km	$5\cdot10^{11}$	• (Goes up to F2)
F_2	200~1000 km	10^{12}	10^{11}

3.2 Atmospheric Effects on Microwave propagation

3.2.1 Microwave propagation delay due to troposphere

The velocity of microwave signals will be affected (refraction) by the atmosphere. In order to discuss neutral atmospheric delay, this part will include both the components due to the stratosphere and troposphere. The reason is the troposphere contains the main mass of the neutral atmosphere and nearly all of the water vapour as discussed before.

The ray bending and the velocity of light (microwave) change between different media.

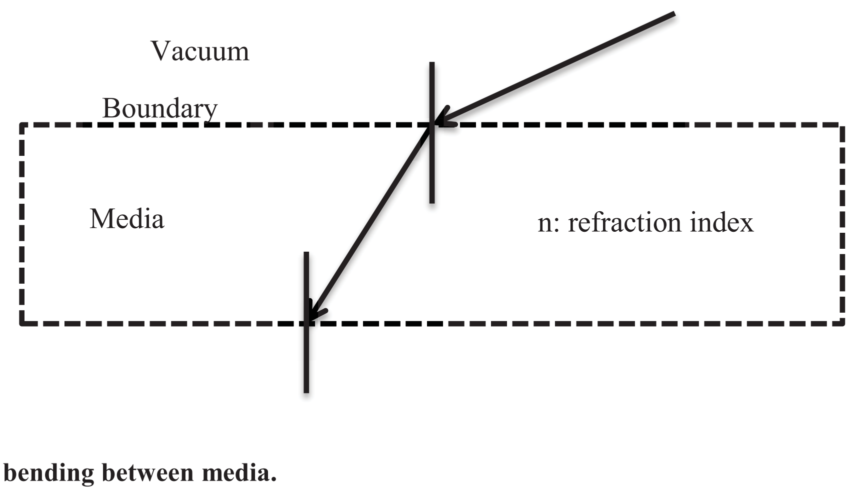

Figure 3.2 Ray bending between media.

The refractive index is:

$$n = \frac{c_0}{c} \qquad (3.2.1.1)$$

where c is the speed of light in some medium and c_0 is the speed of light in vacuum.

However, the refractive index is often expressed in term of the refractivity N, and $\mathrm{N} = 10^6(\mathrm{n}-1)$. That means the refractive index is scaled, in order to make it easier to handle.

In fact, the reason of atmosphere delay is the increased travel path length of microwave signals in atmosphere. The excess path length is expressed as (Davis, 1985):

$$\Delta L = \int_S [n-1]ds + S - G = 10^{-6}\int_S N ds + S - G \quad (3.2.1.2)$$

Where N is the scaled refractive index, $\mathrm{S} = \int_S \mathrm{ds}$ is the curved ray path, s is the position along this ray path, G is the straight line path. According to this equation, the atmospheric delay can be estimated. $10^{-6}\int_S \mathrm{Nds}$ part is the delay due to the signal's reduced propagation velocity, which is affected by the refractive index. $\mathrm{S}-\mathrm{G}$ part is the geometric delay, which comes from the bending of the signal. Normally, people ignore the geometric delay when the elevation angles of rays are bigger that 15˚. Based on GPS observations, the tropospheric effect (delay) on GPS signal is around 2.3 m in zenith direction at sea level, when in near horizon direction at sea level is 20 - 30m.

3.2.2 Microwave propagation delay due to the ionosphere

Due to the free electrons, atoms and molecules which are charged positively, the ionosphere affects microwave propagation with various frequencies, either lower than 3 KHz or higher that 30GHz. The most important parameter of ionosphere that affects microwave signals is Total Electron Content (TEC), which is the total number of electrons calculated along a path. The unit of TEC is electrons per square meter. Ionosphere is related to solar activities because the ionization is determined by the solar radiation. Normally, the electron density changes with time in a day, and reach to a peak at around 2 pm and a nadir at mid-night (local time). Besides, sunspots, which appear periodically, always influence the electron density.

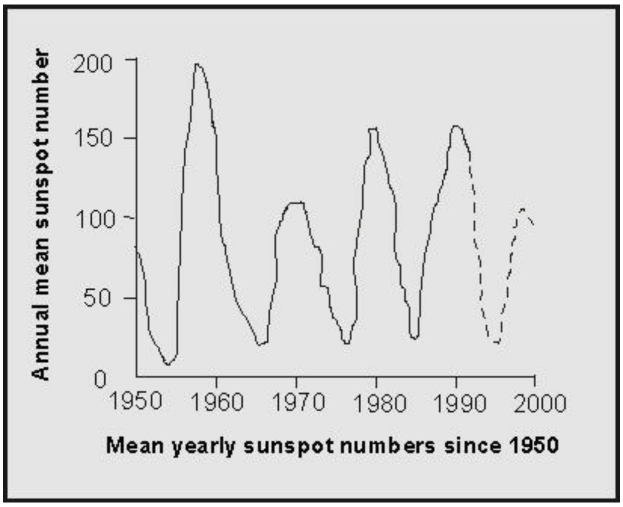

Figure 3.3 Sunspot activities from 1950 to 2000. (Klobuchar, 1991).

The ionosphere is characterized by dispersion and its refractive index of microwaves is a function of frequency and the density of free electrons. It was given with a first-order form that (Klobuchar, 1996) the phase refractive index is:

$$n \approx 1 - \frac{e^2}{8\pi^2 m_e \varepsilon_0}\frac{N_e}{f^2} \approx 1 - 40.3\frac{N_e}{f^2} \quad (3.2.2.1)$$

Where e is elementary charge, $\mathrm{m_e}$ is the mass of an electron, ε_0 is the permittivity of vacuum, f is the microwave frequency, and $\mathrm{N_e}$ is the electron density (per m^{-3}).

By integrating over the propagation path s, the ionospheric effect on range measurement with code is:

$$\delta R_{ION} \approx \frac{40.3}{f^2} \int_s N_e ds \tag{3.2.2.2}$$

Where δR_{ION} is ionospheric effect, f is the microwave frequency.

In range measurement with code, people can determine the range (R) on both frequencies L_1 and L_2 (Seeber, 1993):

$$R = R_1 - \delta R_{1,ION} \tag{3.2.2.3}$$

$$R = R_2 - \delta R_{2,ION} \tag{3.2.2.4}$$

Substituting (3.2.2.2) to (3.2.2.3) and (3.2.2.4), range correction for L_1 by code measurement is:

$$\delta R_{ION} = \frac{R_1 - R_2}{1 - (\frac{f_1^2}{f_2^2})} \tag{3.2.2.5}$$

Corresponding equations for carrier phase measurement can be derived in the same way. Ambiguity terms $N(L_1)$ and $N(L_2)$ were included.

$$\delta\emptyset_{ION}(L_1) = \frac{f_2^2}{f_2^2 - f_1^2}(\emptyset(L_1) - N(L_1) - \frac{f_1}{f_2}(\emptyset(L_2) - N(L_2)) \tag{3.2.2.6}$$

This is so-called ionospheric phase advance for L_1 observations. By integrating both L_1 and L_2 observation, the ionoshperic free linear combination is given:

$$\emptyset(L_0) = \frac{f_1^2}{f_1^2 - f_2^2}\emptyset(L_1) - \frac{f_2^2}{f_1^2 - f_2^2}\emptyset(L_2) \tag{3.2.2.7}$$

According to equations above, the ionospheric advance can be eliminated mostly when dual frequency receivers are used. If consider the frequency only (assume the orbit heights are the same), we calculate that ionospheric effect on signals of SAR satellite with X band (f_X = 9.6 GHZ for TerraSAR-X) is 3 times less than that with C band (f_c = 5.331 GHz for ENVISAT) , and 56 times less than that with L band (f_L = 1.275 GHz for ALOS). This estimation is validated by Hanssen's work list in the table below.

Table 3.3 Ionospheric delay for different bands (Hanssen, 2001)

band	f_0 [GHz]	θ_{inc}	$\frac{\partial \delta^{t_i}_{p,iono}}{\partial \mathrm{TECU}}$ [m]	$\delta^{t_i}_{p,iono}$ [m]	
				Solar min	Solar max
X	9.6	30°	−0.005	−0.10	-0.50
C	5.3	23°	−0.015	−0.31	-1.54
L	1.25	39°	−1.241	−6.40	-31.99

$\delta^{t_i}_{p,iono}$, one-way ionospheric delay. The factor $\partial\delta^{t_i}_{p,iono}/\partial\mathrm{TECU}$ shows the sensitivity of the SAR data for ionospheric disturbances. Solar minimum and solar maximum conditions correspond with 20 and 100 TECU, respectively.

According to the research carried out in JPL (Tong et al., 2009) that people used the TEC difference to make ionospheric correction. It was presented that the typical values is 0.2 TEC then the direct effect is typically around one fringe (12 cm) at L-band (2-way) with 34 degree look angle. Therefore, ionospheric effect on X-band should be minuscule (< 2 mm) under the same conditions. One has to note that the orbit height of TerraSAR-X is 178 m lower than that of ALOS but both of them fly in F_2 layer of ionosphere.

3.3 Atmospheric Correction in SAR images

In the last decade, a lot of approaches have been suggested and applied to reduce atmospheric effects in SAR interferograms. Most current SAR satellites are at the orbits within ionosphere. For example, the altitude of TerraSAR-X is about 514 km. That means the transmitted signals do not pass through the whole ionosphere, so that neither ionospheric models nor GPS-derived ionosphere delay can be used for eliminating ionospheric effects in SAR interferogram. Fortunately, the ionospheric effects is inverse proportional to f^2. As calculated in the last section, the ionospheric effect to TerraSAR-X is imperceptible that can be ignored. Hence, what we will study here is only the effect due to troposphere.

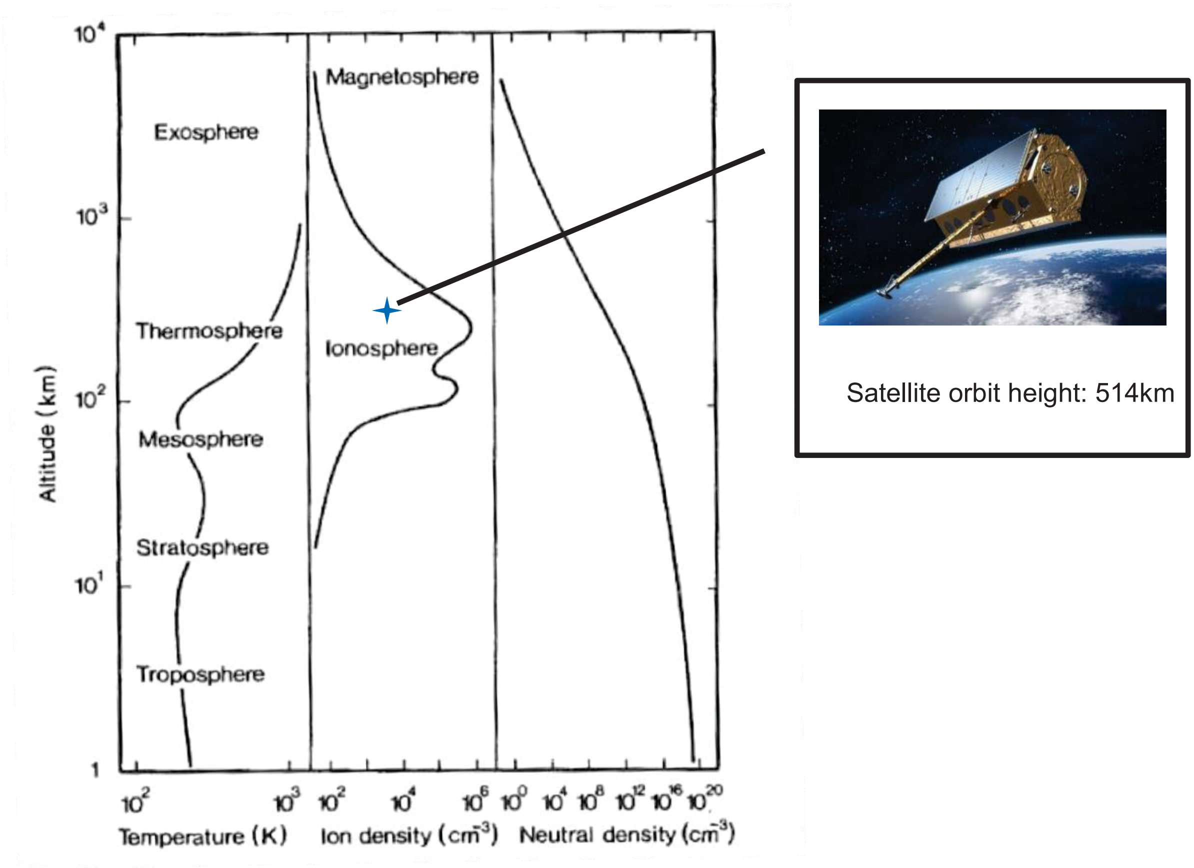

Figure 3.4 TerraSAR-X in ionosphere (Adapted from Rees, 1989).

3.3.1 Models derived from meteorological data

Several empirical models are applied for the mitigation of the tropospheric effect. The most common models are Hopfield (Hopfield, 1969) and Saastamoinen (Saastamoinen, 1972). Besides, there are some other models such as UNB3 (Collins, 1999) and so on.

Hopfield model assumes the neutral atmosphere as two layers, which are the dry and wet one (Fig. 3.5). The temperature lapse rate in the wet layer is set as 6.5 ˚C per kilometer. The total delay modeled by Hopfield model can be expressed as:

$$ZTD = 10^{-6}k_1\frac{P_o}{T_o}\frac{H_D-h}{5}+10^{-6}[k_3+273(k_2-k_1)]\frac{e_o}{T_o^2}\frac{H_w-h}{5} \tag{3.3.1.1}$$

$$H_D = 40136 + 148.72(T_o - 273.15)m \tag{3.3.1.2}$$

Where H_D, H_w, P_o, T_o, e_o and h are height of day layer, height of wet layer, pressure at the site (mbar), temperature on the ground (T), surface vapor pressure (mbar), height of site on the geoid, respectively. $k_1 = 77.6\,K/mbar$, $k_2 = 71.6\,K^2/mbar$, $k_3 = 3.747 \times 10^5\,K^2/mbar$, H_w is 11000m (Qu, et al., 2008).

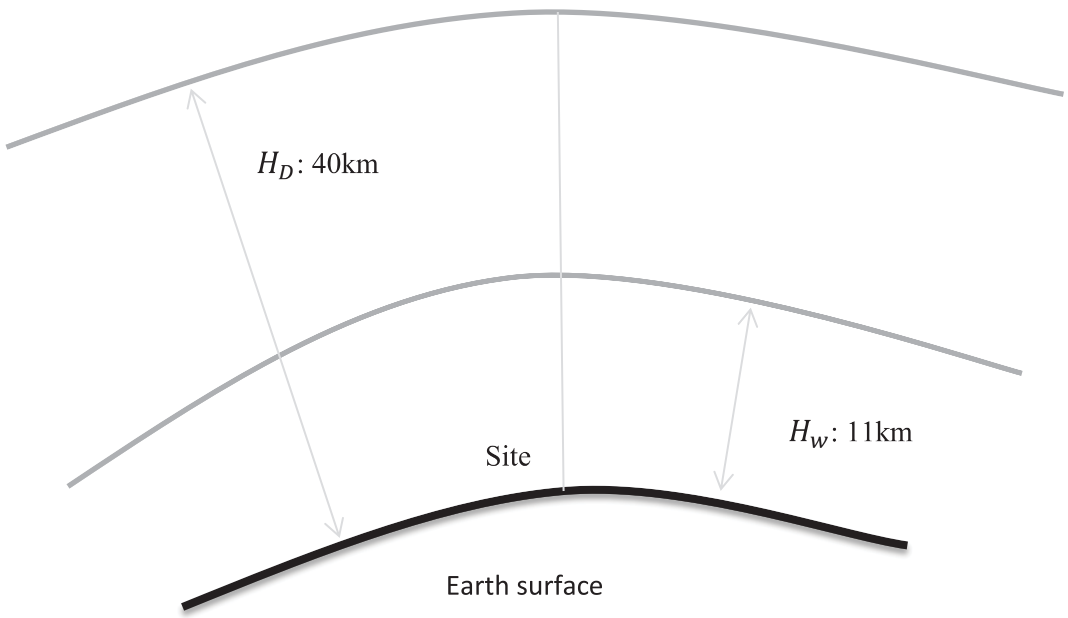

Figure 3.5 Dry and wet layers defined in Hopfield model.

Saastamoinen descripts the air as three layers. In the first layer, from earth surface to 10km height tropopause, the temperature lapse rate is -6.5 °C per kilometer. From tropopause to stratopause which is 70km height, the temperature is constant. Above 70km is ionosphere.

The expression zenith hydrostatic delay in Saastamoinen model is:

$$ZHD = (2.277 \pm 0.0024)\frac{P_s}{f(\varphi,H)} \tag{3.3.1.3}$$

$$f(\varphi, H) = 1 - 0.00266\,cos(2\varphi) - 0.00028H \tag{3.3.1.4}$$

Where ZHD is the zenith hydrostatic delay (in mm), P_s is the surface pressure in hPa, φ is the latitude of the site, and H is the station height above the geoid (in km). Normally, the ZHD value is around 2.3 m. The expression zenith wet delay in Saastamoinen model is:

$$ZWD = 0.002277(\frac{1255}{T_0} + 0.05)e_0 \tag{3.3.1.5}$$

Where ZWD is the zenith wet delay, T_0 is the temperature on surface (in degrees Kelvin), and e_0 is the surface water vapour partial pressure (in hPa). The wet delay is varying from a few cm to 20 cm in a year at mid-latitudes (Elgered, 1993), which are much less than the hydrostatic delay.

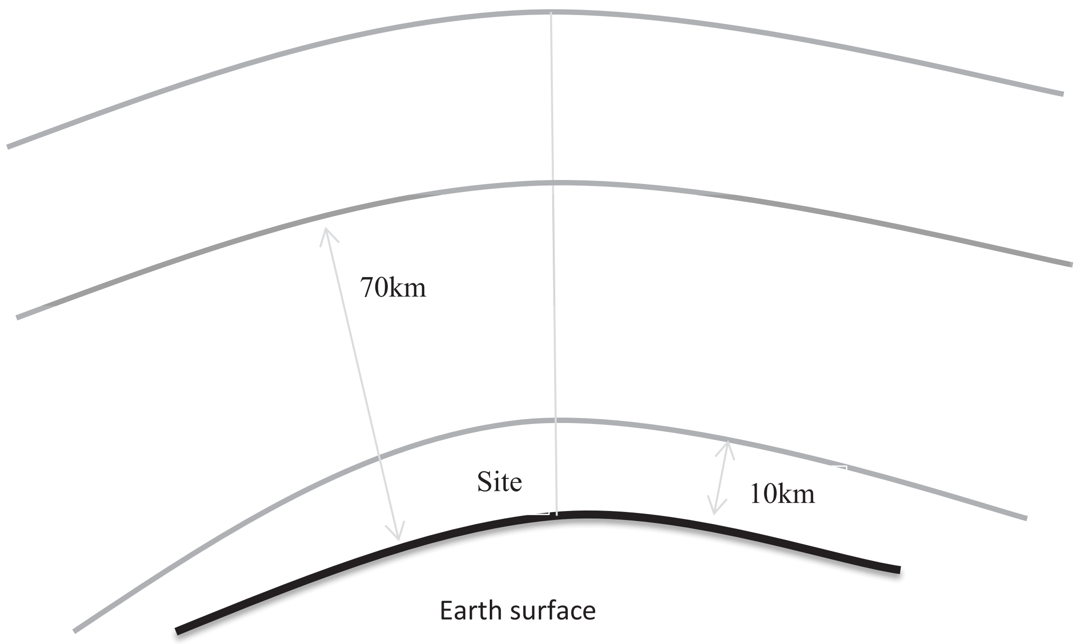

Figure 3.6 Layers defined in Saastamoinen model.

Many other models are proposed, such as taking into account humidity and type of climates. Anyway, people can estimate ZWD using meteorological models with accuracy of 2 to 5 cm (Baby et al., 1988). Besides, such models are able to remove the "stratification effect" but not able to remove the "turbulent effect" (Webley, 2003).

3.3.2 GPS Estimation

As discussed in chapter 2, GPS processing can derive atmospheric products. The Pseudo-Range Observable is:

$$PR_r^s(\tau_r) = \rho_r^s(T^s, T_r) - c[\delta\tau_r(\tau_r) - \delta t^s(t^s)] + deph_r^s + dion_r^s + dtrop_r^s + v_r^s \qquad (3.3.2.1)$$

PR_r^s is the pseudo-range between receiver r and satellite s, ρ_r^s is the true geometric range, $deph_r^s$ is the errors in satellite's ephemeris, $dion_r^s$ is the signal delay biases of ionosphere, $dtrop_r^s$ is the the signal delay biases of troposphere and v_r^s is the observation residual.

If we define $\phi_r^s(\tau_r)$ is the carrier phase observable, N_r^s is the integer ambiguity, f is the frequency. The Carrier Phase Observable then is:

$$\emptyset_r^s(\tau_r) = \frac{f}{c}\rho_r^s(T^s, T_r) - f[\delta\tau_r(\tau_r) - \delta t^s(t^s)] + N_r^s + \frac{f}{c}deph_r^s + \frac{f}{c}dion_r^s + \frac{f}{c}dtrop_r^s + v_r^s \qquad (3.3.2.2)$$

Applying PPP technique:

$$PR_r^s(\tau_r) = \rho_r^s(T^s, T_r) - c\delta\tau_r(\tau_r) + MZPD_r^s + v_r^s$$

(Pseudo-Range) (3.3.2.3)

$$\phi_r^s(\tau_r) = \frac{f}{c}\rho_r^s(T^s, T_r) - f\delta\tau_r(\tau_r) + N_r^s + \frac{f}{c}MZPD + \frac{f}{c}v_r^s$$

(Carrier Phase) (3.3.2.4)

where M is the mapping function, ZPD is the zenith path delay.

By using high precision orbit and clock products, $\delta t^s(t^s)$ and $deph_r^s$ are removed. When using dual frequency receiver, the ionospheric advance can almost be eliminated. Subsequently, the hydrostatic tropospheric delay is predictable and the wet delay is estimated as unknown with mapping functions. In fact, the tropospheric delay was calculated with the receiver clock and site position. The second, the tropospheric delay and receiver clock were estimated when the site position was fixed to the average value. Because height estimates is highly correlated with ZWD estimates (Li, 2005). Therefore, tropospheric delays are estimated from GPS and can be used to reduce atmospheric effects on InSAR. Sometimes a spatial interpolation is necessary. A comparison between GPS-derived products and radiosondes (Li, 2005) showed 6.2 mm agreements of ZWD estimations were achievable. The disadvantages of GPS for atmospheric corrections in SAR interferograms are:

- GPS networks are too sparse in most part of the world.
- GPS-derived zenith delay is an average value of 5 or 10 minutes, and average of several satellites' paths.
- Artefacts with small spatial scales are not possible to be removed as GPS is not able to determine them (Hanssen, 2001).

3.3.3 Pair-wise Logic Approach

A linear combination, or titled as pair-wise logic approach, was applied to remove the atmospheric signals (Massonnet et al., 1995), which requires at least two interferograms with a common SAR images. As Hanssen discussed (2001), if there is an atmospheric anomaly in the common SAR image, it will affect both interferograms. Therefore, people can remove the atmospheric anomalies by summing or subtracting these two interferograms. However, two disadvantages are in this approach (Li, 2005): Firstly, sometimes it is not easy to find a common SAR images with atmospheric effects for two interferograms. Secondly, the deformation rate is assumed as constant, in order to be extracted.

3.3.4 Numerical Model

Numerical model is a powerful tool for atmospheric research, as well as theoretical studies, observational studies and laboratory studies. There are lots of numerical atmosphere model in the world now, such as Global Forecast System (GFS) developed by National Oceanic and Atmospheric Administration (NOAA), and Global Environmental Multiscale Model (GEM) developed by the Meteorological Service of Canada (MSC), and so on. For example, the European Centre for Medium-range Weather Forecasts (ECMWF) is a numerical dataset for Europa, and supplies weather data with temporal resolution of 12 hours and spatial resolution of 2.5 degrees.

An experiment, which has been done by Shimada (2000), used the global objective analysis data (GANAL) in Japanese Meteorological Agency to correct JERS-1 interferograms. The accuracy for detecting surface deformation was double improved nearly, from 4.04 cm to 2.04 cm.

Comparing to ECMWF and GANAL, the local numerical dynamic model (NH3D) used by Wadge et al. (2002) is more accurate for km-scale features. It was well applied in Mt. Etna and shown agreement with GPS results and ERS-2 interferogram. However, Webley pointed out in 2003 that the NH3D model is very sensitive to the initial data.

3.3.5 Multi-temporal InSAR Techniques

Due to the limitations such as de-correlation and atmospheric effects in conventional InSAR, multi-temporal InSAR techniques have been developed in the past years. Normally, multi-temporal InSAR techniques analyze 'persistent scatterers' which are isolated coherent points in both persistent scatterer (PS) and small baseline subset (SBAS) methods. In multi-temporal InSAR processing, the phase contribution from different components: deformation, atmosphere, orbits errors, topographic errors, and noise, can be estimated by considering their time-space behaviors (discussed in chapter 2). Atmospheric Phase Screen (APS) is estimated in each interferogram. Apparently, the atmosphere is uncorrelated with baseline, but high spatially correlated in the interferogram. In fact, the atmospheric errors can be estimated simultaneously with the deformation signal and the orbital errors, because they are all spatially correlated.

Some relevant tests were carried out. One experiment showed the (Root Mean Square) RMS of atmosphere estimation using multi-temporal InSAR is around 0.25 to 1.35 radians, when 41 ERS images over Pomona, California were processed (Ferretti et al., 2000). However, one should keep in mind that the estimated APS contains contributions from two resources, the atmospheric errors and the orbit errors. Besides, another shortcoming of this technique is that large stacks of images are required. The third, this technique relies on both the number and distribution of PS points, and sometime PS points are not available due to vegetation or deformation features.

3.4 Mapping functions of tropospheric delay

Normally, tropospheric delay in the zenith direction can be modelled or estimated. As for determining tropospheric at arbitrary elevation angle, a larger number of mapping functions have been employed, when some assumptions were made. The main idea is that the delay in slant directions is related to that in zenith direction.

$$STD = ZHD \times m_h(\varepsilon) + ZWD \times m_w(\varepsilon) \tag{3.4.1}$$

Where STD is the total slant delay, ZHD is the hydrostatic delay, ZWD is the wet delay, $m_h(\varepsilon)$ and $m_w(\varepsilon)$ are the mapping functions for ZHD and ZWD, and ε is the elevation angle (Davis et al., 1985).

As mentioned, lots of mapping functions have been suggested. Several of them are descripted here.

3.4.1 Chao Mapping Function

In 1972, a method based on daily surface and radiosonde balloon measurements was proposed for tropospheric calibration (Chao, 1972). This model was applied widely in many years. Chao considered hydrostatic and wet parts separately and independent from meteorology observations.

$$m(\varepsilon) = \frac{1}{sin(\varepsilon)+\frac{a_i}{tan(\varepsilon)+b_i}} \tag{3.4.1.1}$$

When $i = 1$ for hydrostatic part, and $a_1 = 0.00143$, $b_1 = 0.0445$.

$i = 2$ for wet part, and $a_2 = 0.00035$, $b_2 = 0.017$.

3.4.2 Niell Mapping Function (NMF)

Niell mapping function (NMF) is one of the most famous mapping functions. NMF is based on one year of radiosonde profiles of the northern hemisphere (Niell, 1996). The Niell hydrostatic mapping function is:

$$m_h(\varepsilon) = \frac{1+\frac{a}{1+\frac{b}{1+c}}}{sin(\varepsilon)+\frac{a}{sin(\varepsilon)+\frac{b}{sin(\varepsilon)+c}}} + \Delta M_h(\varepsilon)H_s \tag{3.4.2.1}$$

$$\Delta M_h(\varepsilon) = \frac{1}{sin(\varepsilon)} - \frac{1+\frac{a_{ht}}{1+\frac{b_{ht}}{1+c_{ht}}}}{sin(\varepsilon)+\frac{a_{ht}}{sin(\varepsilon)+\frac{b_{ht}}{sin(\varepsilon)+c_{ht}}}} \tag{3.4.2.2}$$

$$g(\varphi_i, DoY) = g_{avg}(\varphi_i) + g_{amp}(\varphi_i)cos[2\pi\frac{DoY-28}{365.25}] \tag{3.4.2.3}$$

Where φ is the latitude, H_s is the height above the sea level, DoY is the day of the year, a_{ht}, b_{ht}, c_{ht} are constants, $g_{avg}(\varphi_i)$, $g_{amp}(\varphi_i)$ are constants for given tabular latitudes and given coefficients a, b, c. And a, b, c are determined by Equation (3.4.2.3).

The wet mapping function is the function of latitude:

$$m_w(\varepsilon) = \frac{1+\frac{a}{1+\frac{b}{1+c}}}{sin(\varepsilon)+\frac{a}{sin(\varepsilon)+\frac{b}{sin(\varepsilon)+c}}} \tag{3.4.2.4}$$

Where the coefficients a, b, c are related to the site latitude.

Different from mapping functions proposed before, Niell mapping function added a correction part $\Delta M_h(\varepsilon)$. Niell mapping function decreases very sharply when the elevation angle is low, but slowly with high elevation angles. Different mapping functions, including the simplest one Cosecant Mapping Function (CMF)$1/\sin(\varepsilon)$, agree with each other very well at high elevation angles (Li, 2005).

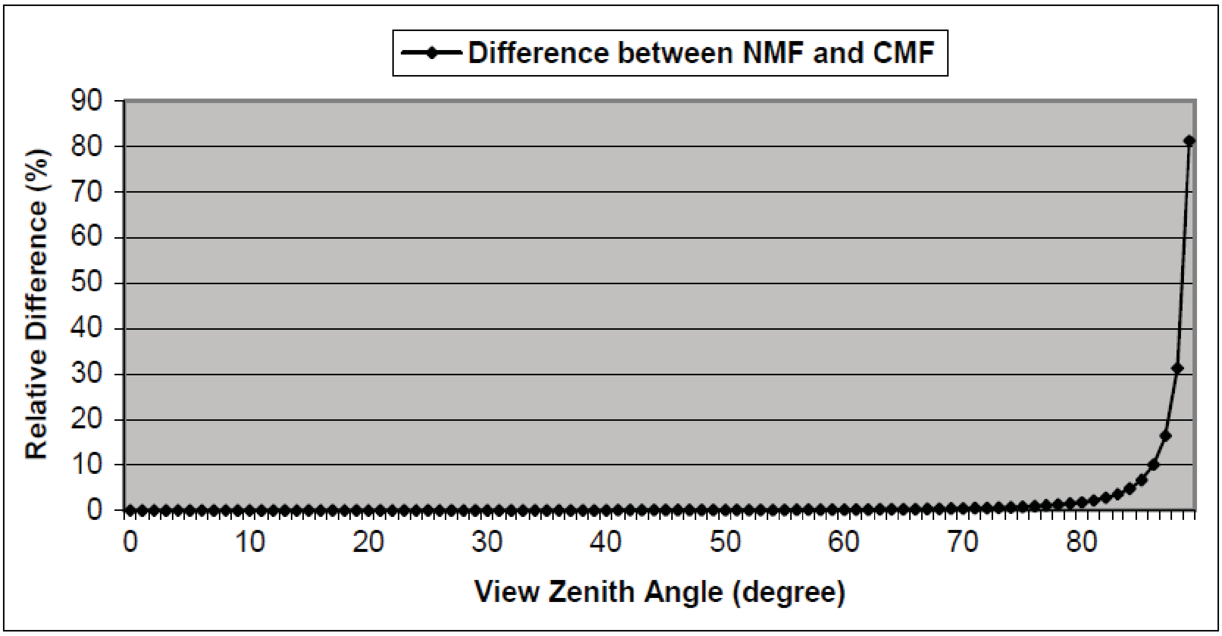

Figure 3.7 Relative differences between NMF and CMF. (Li, 2005).

It is presented that at the HERS IGS GPS station with latitude of 50.90 °N, the relative difference is 0.1% at an elevation angle of 67 ° (view zenith angle 23 °, which is the incidence angle of ERS-1/2), and 0.4% at 20 °. Until the elevation angle reach to 13 °, the difference decreases to 1%.

3.4.3 Vienna Mapping Function and Vienna Mapping Function-1 (VMF1)

In recent years, numerical weather models (NWM) has often been applied to improve mapping functions. Vienna Mapping Function (Boehm, et al., 2004) was investigated from the 40 years empirical data of the European Centre for Medium-Range Weather Forecasts (ECMWF). VMF uses the same Equation as NMF used, but determines these coefficients a, b, c from raytracing through NWM.

$$m(\varepsilon) = \frac{1+\frac{a}{1+\frac{b}{1+c}}}{sin(\varepsilon)+\frac{a}{sin(\varepsilon)+\frac{b}{sin(\varepsilon)+c}}} \qquad (3.4.3.1)$$

The coefficients a, b, c are different for the hydrostatic and wet components.

Therefore, VMF can be understood as a more rigorous NMF. A brief description of rigorous determination of the coefficients in VMF is here.

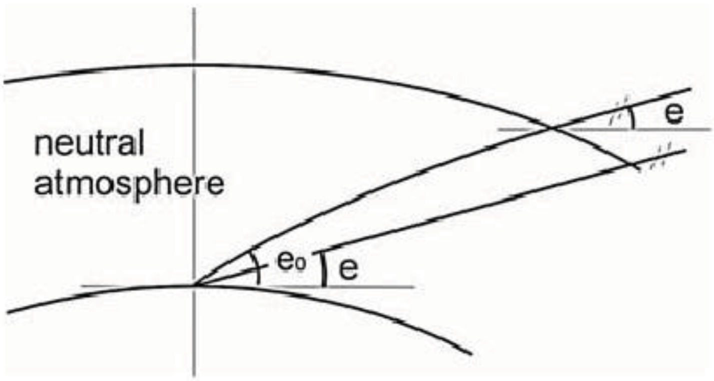

Figure 3.8 Bending of the ray in the neutral atmosphere. (Boehm, 2004).

The e in vacuum, so-called outgoing elevation angle, is smaller than the initial elevation angle e_0. At each site when ECMWF data are available, the hydrostatic mapping function, wet mapping function, and the outgoing elevation angles are determined at 10 initial elevation angles, which are 90°, 70°, 50°, 30°, 20°, 15°, 10°, 7°, 5° and 3.3°. For the continued fraction form in Equation (3.4.2.1), the coefficients a, b, c are estimated by least square processing. It was presented (Boehm, et al., 2004) that these coefficients are sufficient to map the zenith delays even down to elevation angle of 3° with residuals less than 2 mm. In 2006, an improved version of VMF so-called VMF1 was proposed (Boehm, et al., 2006a). By using ECMEF data as well, VMF1 redetermined the b, c coefficients and used the best coefficients available for the dydrostatic mapping functions. As for the coefficient a, it is derived by inverting the continued fraction form and depend on the day of the year, unlike VMF.

3.4.4 Global Mapping Function

The VMF1 is the most accurate and reliable mapping function providing global geodetic results (Boehm, et al., 2006b). However, the VMF1 is only available at some locations such as IGS (International GNSS Service) sites and IVS (International VLBI Service for Geodesy and Astrometry) sites. Therefore, the Global Mapping Function (GMF) was developed (Boehm, et al., 2006b) based on VMF1. The coefficients used in GMF are derived from an expansion of the VMF1 parameters into a global grid. According to the validation of mapping functions carried out (Boehm, et al., 2006b), the agreement between VMF1 and GMF is very good. But in GMF and NMF comparison, the station height differences up to 10mm can be found in the northeast China and Japan. This is the most advanced mapping function and hence will be used in this research.

3.5 Road Map and Related Work

In this atmospheric study, both GPS estimation (PPP) and multi-temporal InSAR technique (PSI) will be chosen as the approaches for atmospheric correction. Saastamoinen model and Hopfield model are going to be applied for ZHD estimation. As for mapping atmospheric delay between zenith and slant direction, GMF will be handled.

Several excellent experiments have been done by KIT (Hinz, 2011) and so on, who applied PPP to derive ZWD from GPS observations and then mapped it to the radar line-of-site for obtaining Slant Wet Delay (SWD). On the other hand, Atmosphere Phase Screen (APS) on relevant images was estimated by InSAR. The comparison of derived SWD from both systems indicated a good agreement.

3.6 Summary

This chapter gives an introduction of the structure and components of atmosphere, and its effects to the signal propagation with regard to GPS and InSAR. Furthermore, a brief overview of existing approaches for atmospheric correction is presented. In this study, GPS estimation and multi-temporal InSAR (PS method) are focused on to eliminate the atmospheric delay, especially the wet delay. They are going to be performed in Chapter 4.

Chapter 4 Application to Urban Area

Since the industrial age, cities' rapid developments gave challenges to geologists and engineers. Construction of subway and skyscrapers and so on bring subsidence to cities as well as underground water extraction. Comparing to other movements happened in volcanos or mining areas, land movements in urban area are usually relative smaller. However, due to people's livelihoods in urban area, such 'small' movements require people attach importance to absolutely. InSAR and relevant techniques have been widely applied to urban area in the past ten years. The result showed that InSAR or PS-InSAR is quite sensitive to small displacements. Hence, InSAR may be a good choice for monitoring urban areas. On the other hand, we have to pay attention to error resources when using InSAR in urban areas, because errors could be easy to contaminate the deformation signals when they are very weak.

In this chapter, an application of InSAR technique to urban area will be presented. Errors, especially that due to atmospheric effects, will be eliminated using different methods, in order to obtain the clear deformation signal finally.

4.1 Introduction

Düsseldorf is a German city lies southwest of the Ruhr urban area, and in the middle of the Rhine-Ruhr metropolitan region (Wikipedia). The altitude of Düsseldorf ranges from 165 m (the top of Sandberg) to 28 m (Wittlaer borough).

Figure 4.1 Location of Düsseldorf shown in Google earth.

According to the record (The Weather Channel), the average annual temperature in Düsseldorf is 10.6 °C. As for the average yearly precipitation, it goes to 797 centimetres. In Düsseldorf, the summer is short and the winter is snowy like most German cities. Düsseldorf is the seventh largest city in Germany and more than 0.5 million people live here. Besides, Düsseldorf has prosperous businesses, as well as a number of famous universities and research institutes.

4.2 Activity

In 2011, the urban tunnel project so-called "Wehrhahnlinie" in Düsseldorf was carried out. The hydro-shield tunnelling process was applied and started in April 2011 and ended in December 2011. The shield tunneling was done by shield machine "Turborine". The outer diameter of the tunnel is constant as 9.50 m. In this process, reinforcement steel fiber concrete and rebar were executed (Mark et al., 2012).

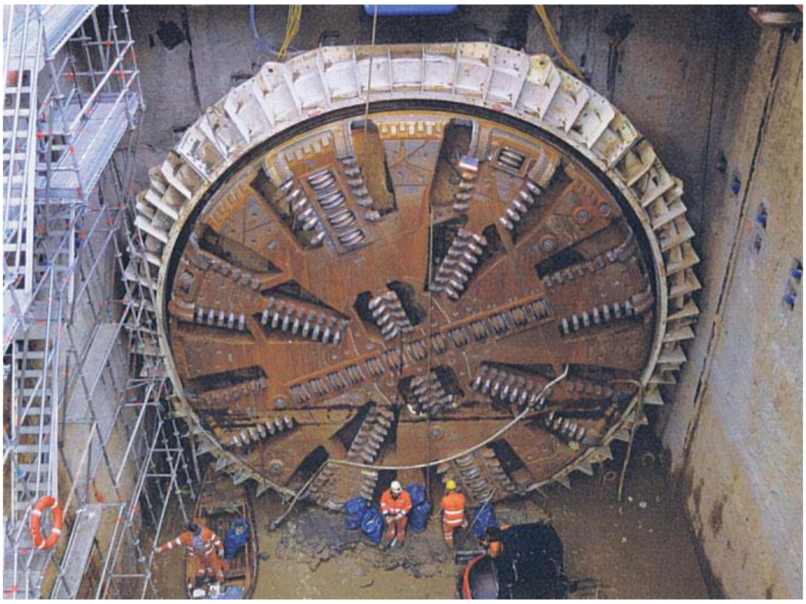

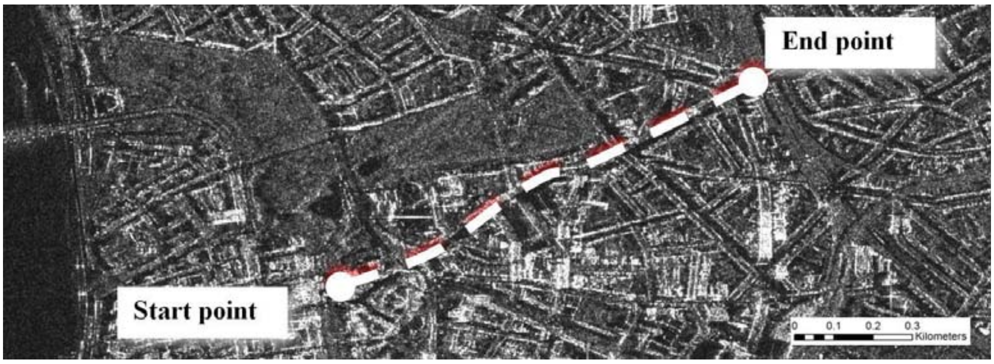

Figure 4.2 Upper: Shield machine "Turborine" arriving in the target shaft (Mark et al., 2012).

Below: Position of construction shown on radar image (Krivenko et al., 2012).

4.3 SAR data

In this study, 20 TerraSAR-X images in Strip Map (SM) mode with HH polarization from 07 Jan 2011 until 31 Oct 2011 were used. This data set was provided by DLR with project ID CAL1140. As well as parameters of TerraSAR-X data, the list of acquisition time and baseline information of SAR data set is shown as below:

Table 4.1 Parameters of TerraSAR-X data.

Nominal orbit height at the equator	514 km
Revisit time (orbit repeat cycle)	11 days
Radar carrier frequency	9.65 GHz (X band)
Wavelength	3.11 cm
Polarizations	HH, VH, HV, VV
Incidence angle range for StripMap / ScanSAR modes	20° - 45° full performance
Maximum achievable resolution (in range)	0.65 m - 1.5 m @ 300 MHz (advanced mode)
Azimuth resolution	1 m - 16 m

Table 4.2 TerraSAR-X data set used.

NO.	Date	Bperp (m)
1	07 Jan 2011	62
2	18 Jan 2011	27
3	29 Jan 2011	-11
4	09 Feb 2011	-55
5	20 Feb 2011	153
6	14 Mar 2011	-104
7	16 Apr 2011	-6
8	19 May 2011	83
9	30 May 2011	151
10	10 Jun 2011	0
11	02 Jul 2011	85
12	13 Jul 2011	34
13	04 Aug 2011	35
14	15 Aug 2011	281
15	26 Aug 2011	82
16	06 Sep 2011	18
17	17 Sep 2011	-14
18	28 Sep 2011	87
19	20 Oct 2011	55
20	31 Oct 2011	290

The coverage of TerraSAR-X strip map image is 30 km width and 50 km length (Fig. 4.3). The Düsseldorf city locates at the north-east corner in the SAR image in which the Rhine river is visible.

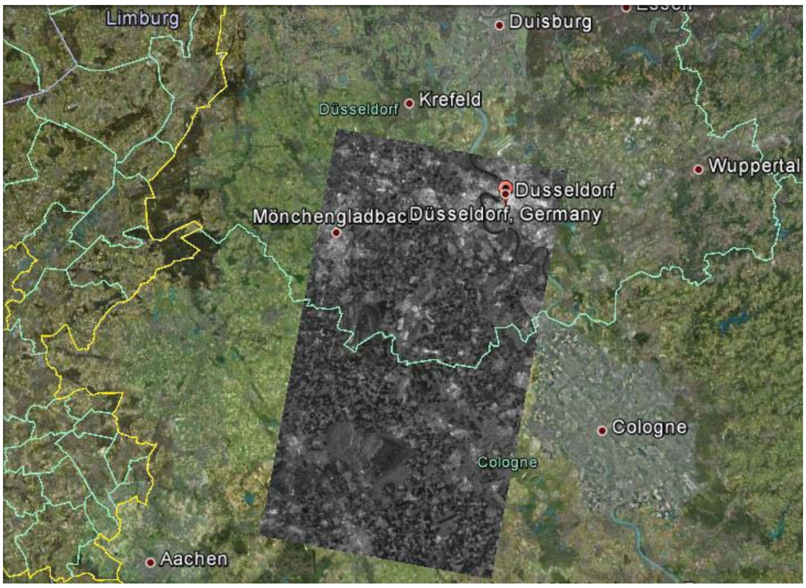

Figure 4.3 TerraSAR-X image covering Düsseldorf shown in Google earth.

4.4 GPS Observations

In this study, observations from 5 Continuous GPS (CGPS) stations are selected according to the SAR image coverage. They are Düsseldorf-G2, Viersen-G2, Essen-G2, Hagen2-G2 and Frimmersdorf-G2 CORS stations (Fig. 4.4).

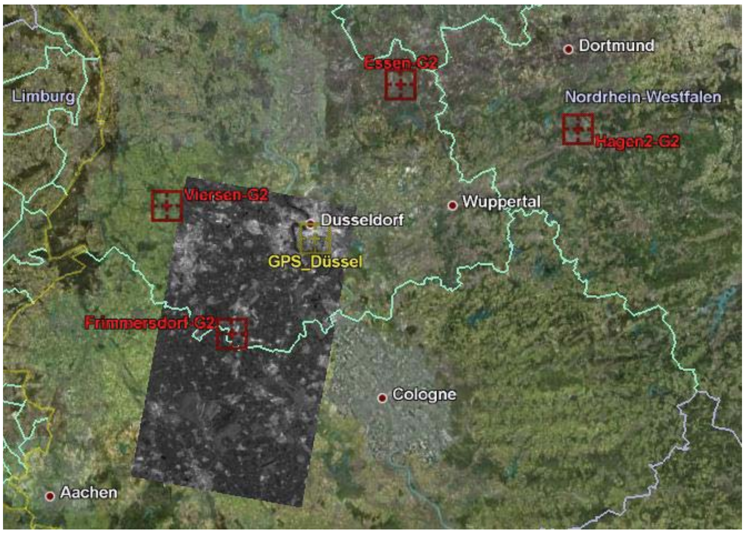

Figure 4.4 GPS stations shown on Google Earth.

At each site, 24 hours observations per day are acquired by TRIMBLE NETR5 receivers. Receiver Independent Exchange (RINEX) data with 15 seconds interval in Hatanaka format were kindly provided by Bezirksregierung köln. From Jan 2011 to Oct 2011, GPS observations at the dates when TerraSAR-X passed (Tab. 4.1) were collected. Two of these CORS stations are covered by the SAR image. GPS observations are used for interpolation test and comparison of atmospheric correction with PSI approach.

4.5 Terrestrial measurements

In order to monitoring the subsidence due to the tunnel excavation, terrestrial measurements were carried out by the State Capital of Düsseldorf, which could be used for the comparative analysis with InSAR products as well.

4.6 Data Analysis

We processed both SAR images and GPS data. InSAR processing will provide the time series of displacements during the time span of monitoring. ZWD was estimated by InSAR processing. Furthermore, GPS was tried to derive the ZWD and the obtained values were compared to those of InSAR-derived. With the help of atmospheric correction, the time series of displacements was improved when comparing to the ground truth (leveling).

4.6.1 SAR data processing

Totally, 32 interferograms were formed from the 20 TerraSAR-X images list before in our estimation (Table 4.3). This selection based on minimizing the temporal and spatial de-correlations. The city centre of Düsseldorf is the AOI (area of interest). The radar images were cropped to the AOI and a SRTM DEM covering this area was resampling into SAR geometry. PSI, particularly StaMPS was the InSAR approach applied here. People would refer to chapter 2 for more details of processing chain. Firstly, DORIS processed this data set and provided interferograms. Subsequently, a combined MTI (multi-temporal InSAR) which integrated both PS and SBAS methods in StaMPS was used for time series analysis (Fig. 4.5). The area around (with 20 m radius) GPS station in Düsseldorf was set as the reference area. Phase correction for DEM errors was carried out as well as for atmosphere and orbit errors, by high pass and low pass filters.

Table 4.3 Interferograms formed in SBAS processing.

Interferogram Pairs	B*temp* (d)	B*perp* (m)
07-Jan-2011 to 18-Jan-2011	11	-34
07-Jan-2011 to 29-Jan-2011	22	-75
18-Jan-2011 to 29-Jan-2011	11	-40
18-Jan-2011 to 09-Feb-2011	22	-84
18-Jan-2011 to 20-Feb-2011	33	126
29-Jan-2011 to 09-Feb-2011	11	-44
09-Feb-2011 to 14-Mar-2011	33	-49
14-Mar-2011 to 16-Apr-2011	33	99
16-Apr-2011 to 19-May-2011	33	91
19-May-2011 to 30-May-2011	11	68
19-May-2011 to 10-Jun-2011	22	-84
19-May-2011 to 02-Jul-2011	44	2
30-May-2011 to 10-Jun-2011	11	-152
30-May-2011 to 02-Jul-2011	33	-65
10-Jun-2011 to 02-Jul-2011	22	86
10-Jun-2011 to 13-Jul-2011	33	34
02-Jul-2011 to 13-Jul-2011	11	-52
02-Jul-2011 to 04-Aug-2011	33	-51
13-Jul-2011 to 04-Aug-2011	22	1
04-Aug-2011 to 26-Aug-2011	22	47
04-Aug-2011 to 06-Sep-2011	33	-18
15-Aug-2011 to 26-Aug-2011	11	-201
26-Aug-2011 to 06-Sep-2011	11	-64
26-Aug-2011 to 17-Sep-2011	22	-96
26-Aug-2011 to 28-Sep-2011	33	5
06-Sep-2011 to 17-Sep-2011	11	-32
06-Sep-2011 to 28-Sep-2011	22	69
06-Sep-2011 to 20-Oct-2011	44	36
17-Sep-2011 to 28-Sep-2011	11	101
17-Sep-2011 to 20-Oct-2011	33	68
28-Sep-2011 to 20-Oct-2011	22	-33
20-Oct-2011 to 31-Oct-2011	11	239

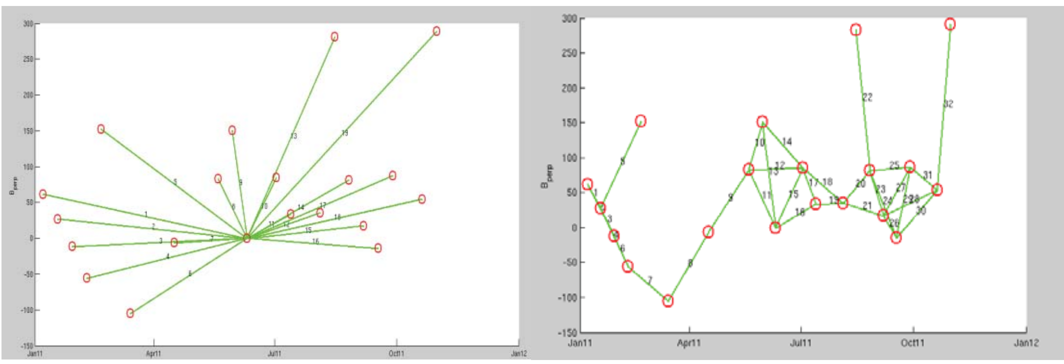

Figure 4.5 Baselines of PS (left) and SBAS (right) methods used.

4.6.2 GPS data processing

Precise Point Positioning (PPP) technique was applied in order to estimate the atmospheric effects. For each GPS station, 24 hours data on the days having SAR passed were processed using PPP. As presented in Chapter 2 already, unlike applying differencing in relative positioning, PPP treats parameters such as the ZWD and the receiver clock as unknowns. These unknowns are evaluated through statistical models. In this study, GNSS-Inferred Positioning System and Orbit Analysis Simulation Software (GIPSY-OASIS) developed by the Jet Propulsion Laboratory (JPL) was used for GPS data processing. JPL's Automatic Precise Positioning Service (APPS), which is known as Auto-GIPSY, and the Canadian Spatial Reference System (CSRS) Precise Point Positioning (PPP) service (CSRS-PPP) were used for the validation of results.

Prior to PPP analysis, we carried out pre-processing checks. Usually, one step is to convert data to RINEX format by TEQC. However, RINEX data in Hatanaka format were provided here so that that conversion could be omitted. In this case, GLONASS data involved in files were rejected. Then TEQC was run for editing data and quality checks.

The Perl script gd2p.pl is the main part when using GIPSY-OASIS for static or kinematic positioning. Various models and augmentation products were applied in the processing strategy.

4.6.2.1 Orbits and Clocks

The script gd2p.pl will download and use JPL’s final orbit/clock products automatically. JPL generates these products from the FLINN network. FLINN stations are better equipped than normal IGS stations. Because FLINN stations have hydrogen maser clocks (some with rubidium or caesium clocks), which are able to provide stable time reference. As well as JPL’s clock products, JPL’s fiducial free orbits are offered.

Table 4.4 JPL's Precise Orbit and Clock Products in GIPSY Format.

(JPL website, available on 4th March 2013).

Product	Latency	3D RMS (cm)	Product Location
Ultra-Rapid	< 2 hours	5	**ftp://sideshow.jpl.nasa.gov/pub/JPL_GPS_Products/Ultra**
Rapid	Next-Day	3.5	**ftp://sideshow.jpl.nasa.gov/pub/JPL_GPS_Products/Rapid**
Final	< 14 days	2.5	**ftp://sideshow.jpl.nasa.gov/pub/JPL_GPS_Products/Final**

4.6.2.2 Troposphere Mapping

GMF was incorporated into GIPSY and it was used in this processing to map both the hydrostatic and wet troposphere to zenith. GMF, which is the global version of VMF1, utilizes 40 years empirical data from ECMWF. GMF is dependent on the date and latitude.

4.6.2.3 Zenith Wet Delay of Troposphere

ZWD can be estimated in GIPSY processing after removing the zenith hydrostatic delay using an atmospheric model. ZHD in Saastamoinen model is:

$$ZHD = P \cdot 0.00227 \cdot e^{(-0.000116 \cdot h)} \qquad (4.6.2.3.1)$$

where P is the pressure and h is the height of the GPS station above the ellipsoid.

In this case a standard pressure was applied then apriori hydrostatic delay is equal to $1.013 \times 10^3 \times 0.00227 \times e^{(-0.000116 \cdot h)}$ meters.

ZWD was determined in GIPSY as a parameter when the FLINN non-fiducial products were fixed. If the station coordinates, ZWD and other unknowns are calculated, they will be used as inputs for the following iteration (normally 2 or 3 times are sufficient).

4.7 SAR Results and Discussion

Some previous results of these data sets have been presented (Mark et al., 2012). In that study, people used commercial software, and PSI was applied by using single master approach. However, we combined both PSI (single master) and SBAS (multi-master) methods for InSAR processing as mentioned before based on open-source software packages. Figure 4.6 shows the PSI result for AOI. After the whole selection and processing, 787,991 PS points which are scattered over $12.3\ \text{km}^2$ remained. In this velocity map, DEM errors, atmosphere effect, orbit errors and noises were estimated and already filtered out.

The PSI result was shown in Figure 4.6, the units are mm/year with negative values being away the satellite and positive values being towards the satellite in the line of sight. Evidently, the north-west corner and the south-east corner of AOI are clumpy so that some small part without PS point can be seen. However, the density of PS point is $64064/\text{km}^2$ which is extremely high.

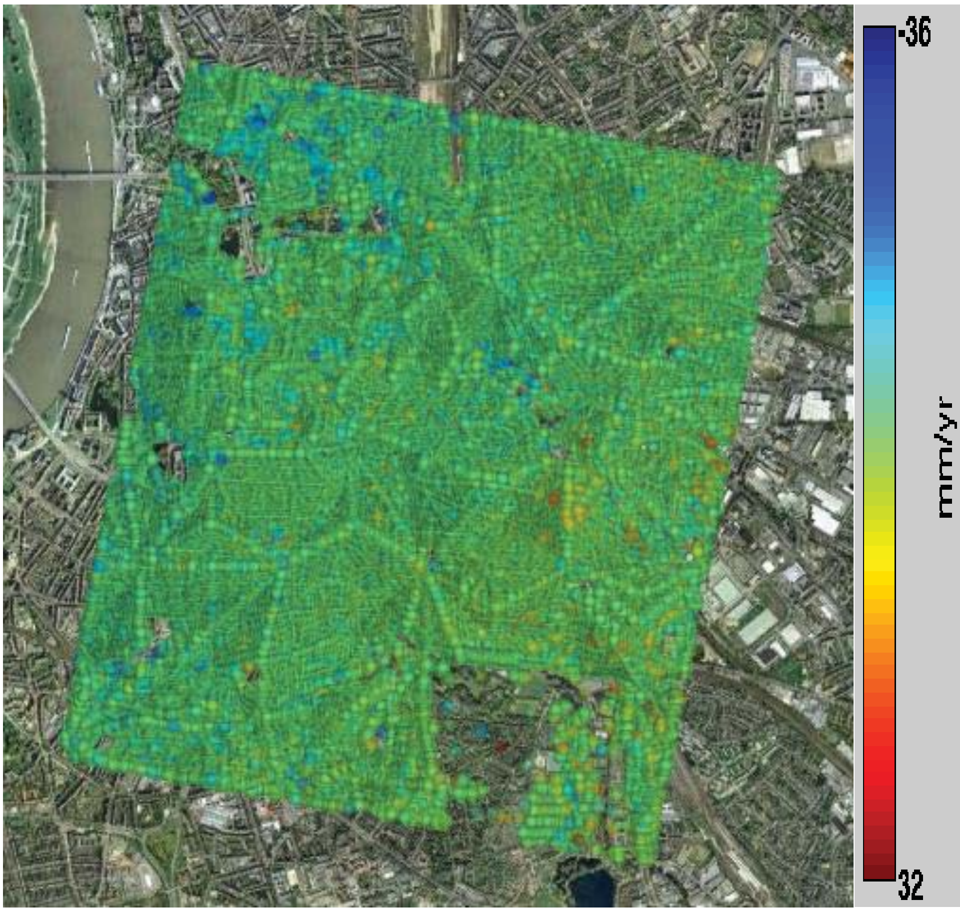

Figure 4.6 Düsseldorf velocity map by PSI.

According to the velocity map, the velocity rates are generally flat over the whole map, which is reasonably expected in Düsseldorf. Some areas are of topographic effects or something else but not real deformation signals, for example, in the east-central of AOI. These effects may be caused by long baseline pairs in PS processing as they are exist in PS step but eliminated when only short baseline pairs formed in SBAS step. However, they are shown in the final velocity map because PS points from PS and SBAS processing chains are remained and then combined. What considered in this study is the area with tunnelling activities as shown in Figure 4.2. Especially the area in Figure 4.7, where the control point locates in is focused on.

Figure 4.7 PS points covered AOI. The red star is the control point.

Blue points are PS1, PS2 and PS3 respectively.

Mostly, PS points close to the 'Wehrhahnlinie' tunnel are stable, however with some interesting exceptions. In this construction, compensation injections were carried out in some cases. A number of buildings on the ground along the tunnel line could benefit from compensation injections to avoid damages which would have happened due to the subsidence caused by excavation. The velocity map indicates that some points in that area have positive displacements (points with yellow and red colours) which may be induced by such injections. In a more in-depth discussion, time series analysis of some points with uplift behaviour in this area follows. Figure 4.8 shows the phase history of three persistent scatterers. These first two points lie in the area near to the start point of tunnelling when the third one is close to the end point. From January until April 2011, an extensive amount of points with uplift that similar to PS1 and PS2 can be seen in the area adjacent to the start point. On the contrary, in the area close to the end point of tunnelling, a cluster of points with apparent subsidence behaviour (PS3 in Figure 4.7) can be found (-6 to -10 mm/year), which have been verified that because of a replacement of the original pavement.

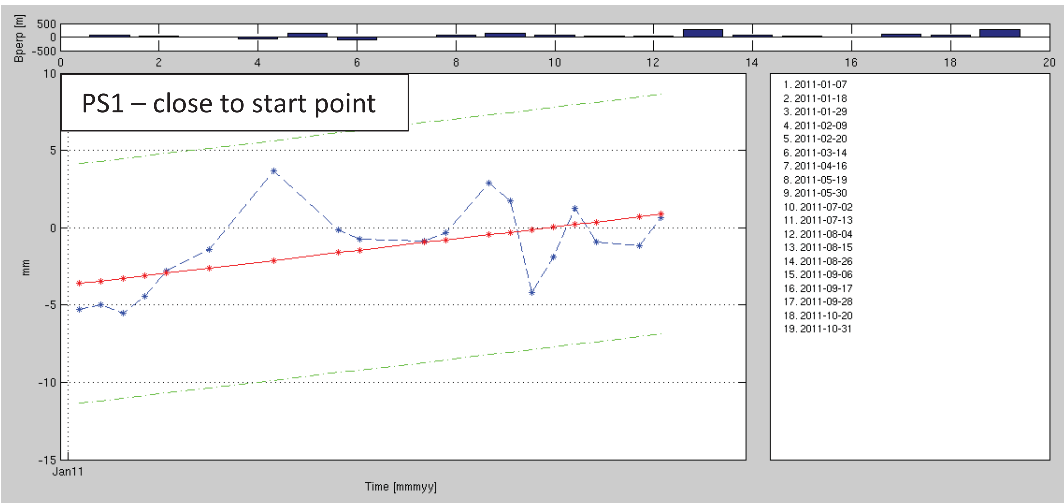

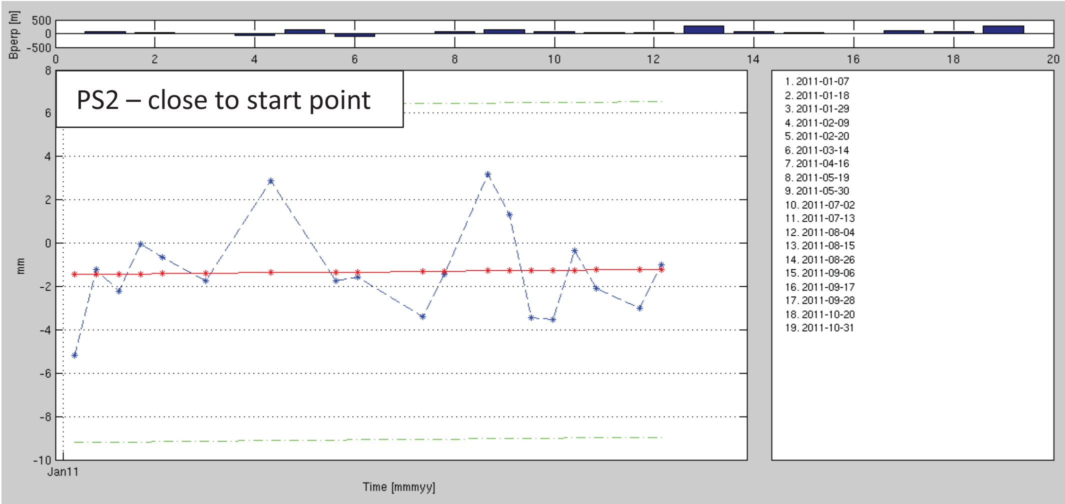

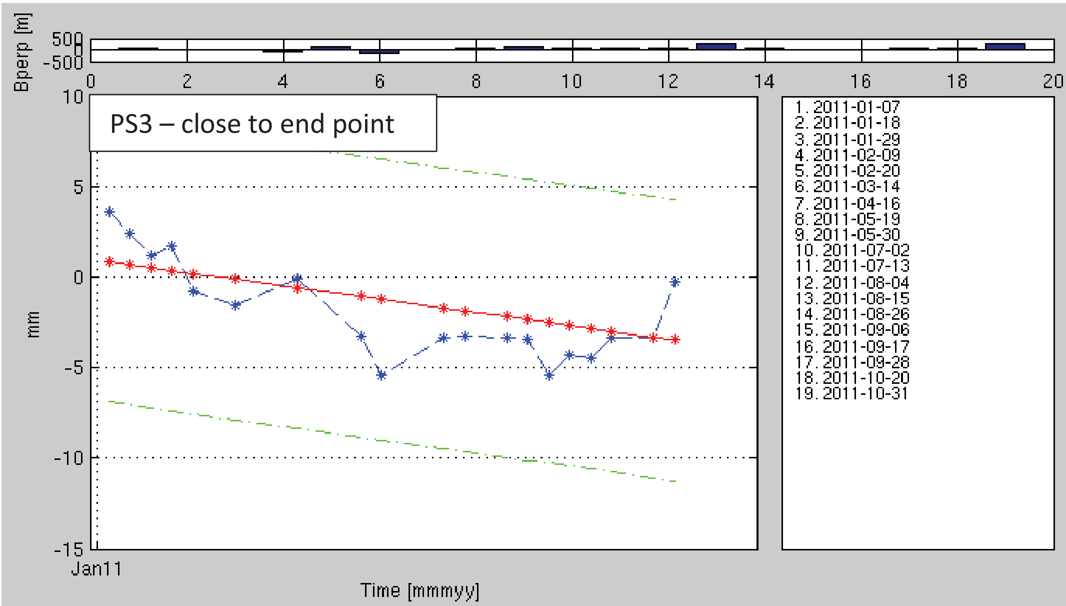

Figure 4.8 Time series of three PS points.

Getting along with the tunnelling, levelling provided by the State Capital of Düsseldorf was used for monitoring the effect of this underground activity. Therefore, we use the levelling result to validate PS-InSAR approach here. For comparative analysis, the persistent scatterer (PS1) was chosen with some small phase jumps corrected, due to the close (with the distance of 20 m) distance to the geodetic benchmarks. In order to convert the deformation in LOS to vertical direction, the directional cosines in analytic geometry was applied. In other words, the directional cosines actually are the percentages of the real displacement along three directions: vertical, N-S and E-W. The actual movements are always underestimated if only using LOS displacements. In this study, the movements were assumed as purely vertical based on a priori knowledge. As the incidence angle is around 35 degree, we found an underestimation of 19% of purely vertical movements by using the LOS values. PSI and levelling (Fig. 4.9 and Fig. 4.10) show comparable results below with very few discrepancies.

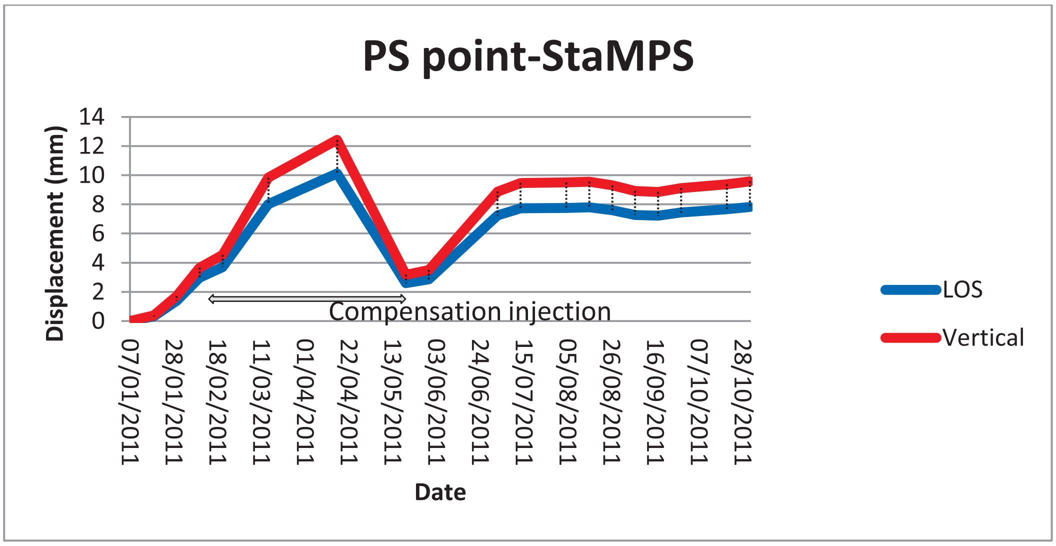

Figure 4.9 Time series of one PS point in LOS (in blue colour) and converted into vertical (in the red colour) with directional cosines.

It is significant that the ground surface started to uplift since compensation injections began. Subsequently, the ground surface went down slightly when the TMB (Tunnel Boring Machine) passed the area and later supporting stopped. Finally, the ground came back to be stable but at a higher level than that before the tunnelling.

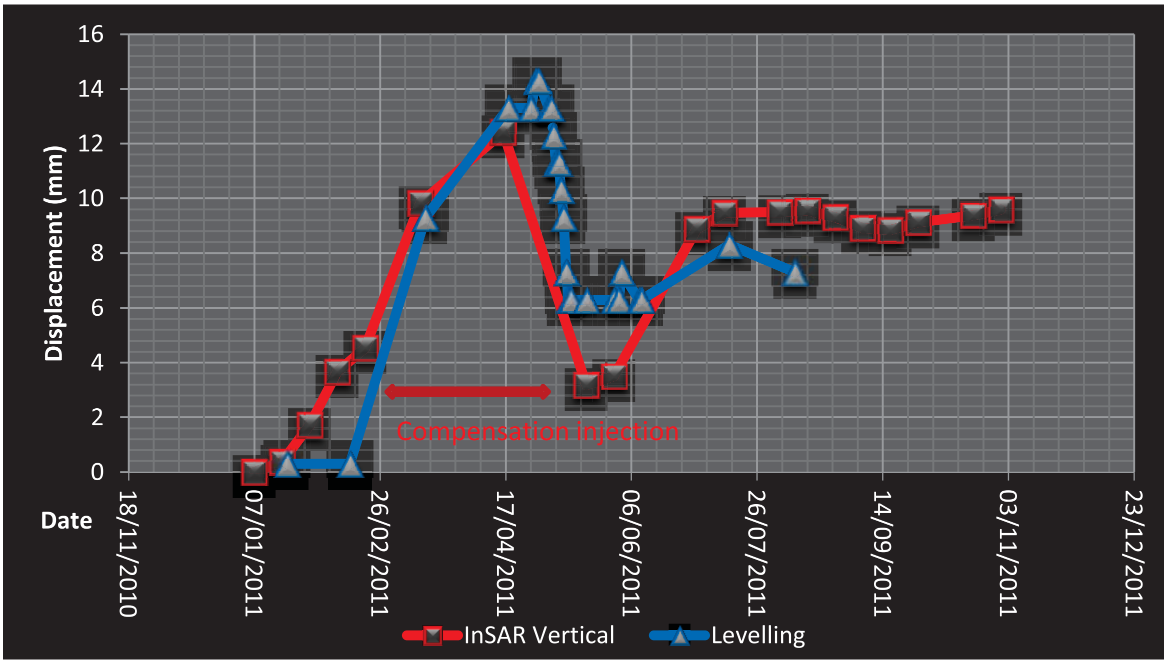

Figure 4.10 Comparison of time series derived by InSAR and levelling.

4.8 GPS Results and Discussion

The ZWD time series at Düsseldorf GPS station sampled at the TerraSAR-X acquisition dates are shown below. For each day, 24 hours GPS observations were processed by GIPSY with the sigma of 0.001m. The Y axis shows the ZWD in meters. Surface meteorological data used in this processing were taken from GPT (Global Pressure and Temperature) model. GPT is an empirical model to determine pressure and temperature from the day of the year and the station coordinates (Boehm et al., 2007). The Matlab source codes of GPT are available online: http://mars.hg.tuwien.ac.at/~ecmwf1/gpt.m.

Figure 4.11 and 4.12 presented ZWD time series at each SAR acquisition date derived by PPP using GPS data at station Düsseldorf. The X axis indicates the observation time (hours) when Y axis indicates zenith wet delay (meters).

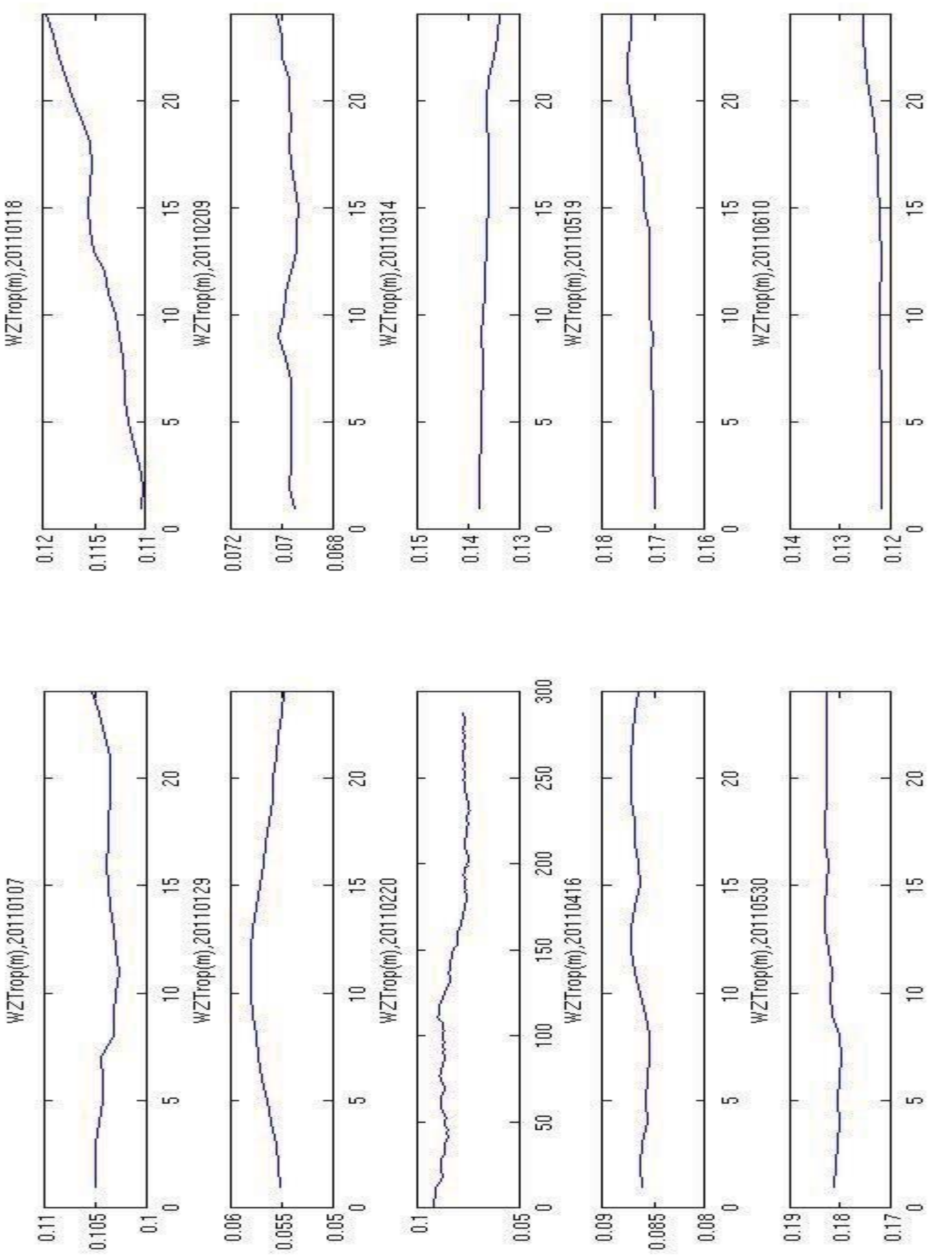

Figure 4.11 ZWD time series during 2011 (January to June).

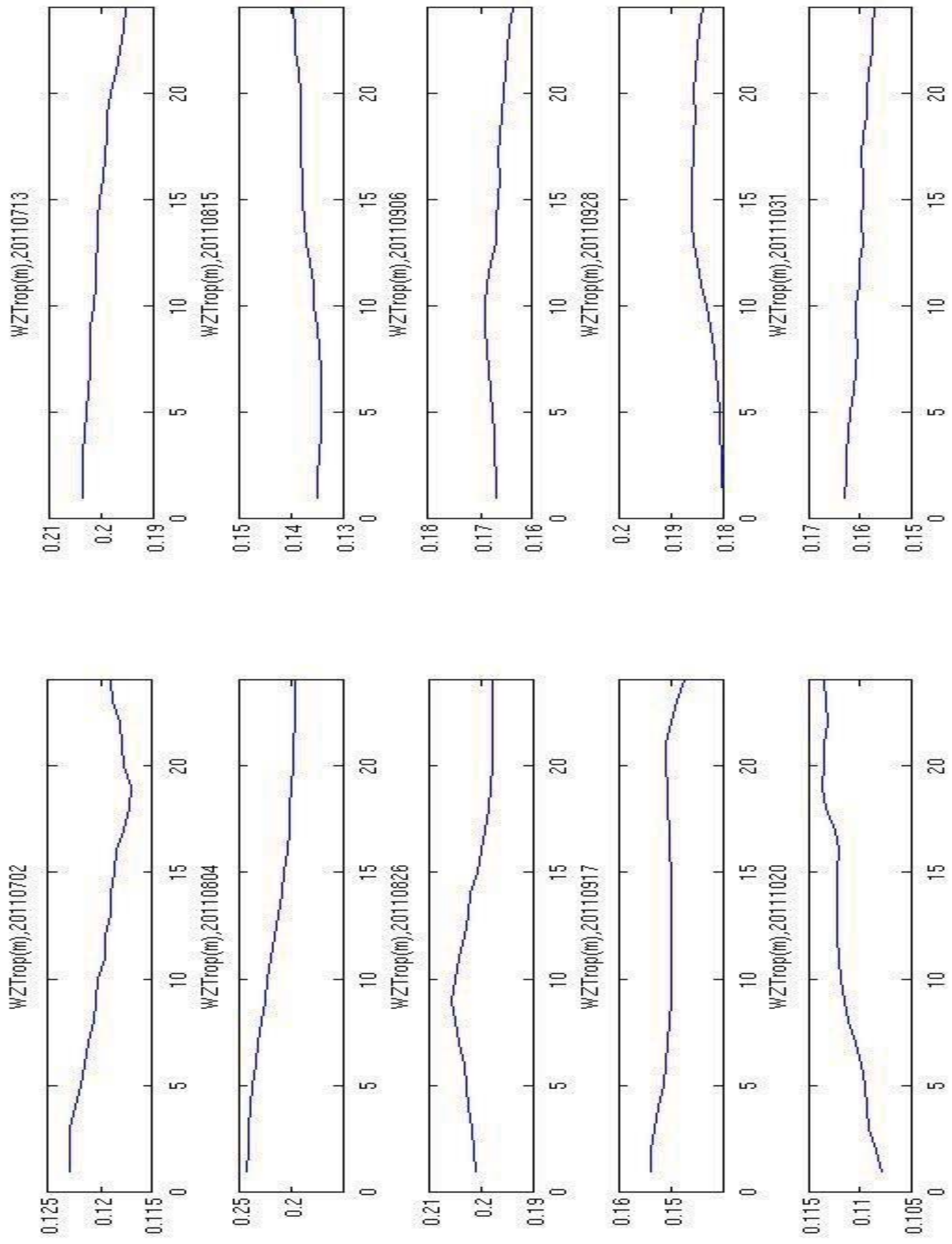

Figure 4.12 ZWD time series during 2011 (July to October).

According to GPT model, ZHD at Düsseldorf station is expected to have slight variations in one year. Therefore, changes in ZTD estimated here mainly indicated the variations of ZWD. In figure 4.13, the X axis is observation time in hours while Y axis indicates ZTD in meters. Apparently, the ZTD in summer time and winter time are quite different. Comparing results at all five GPS stations, ZTD have higher values during summer time (20110804) than in winter time (20110129) generally.

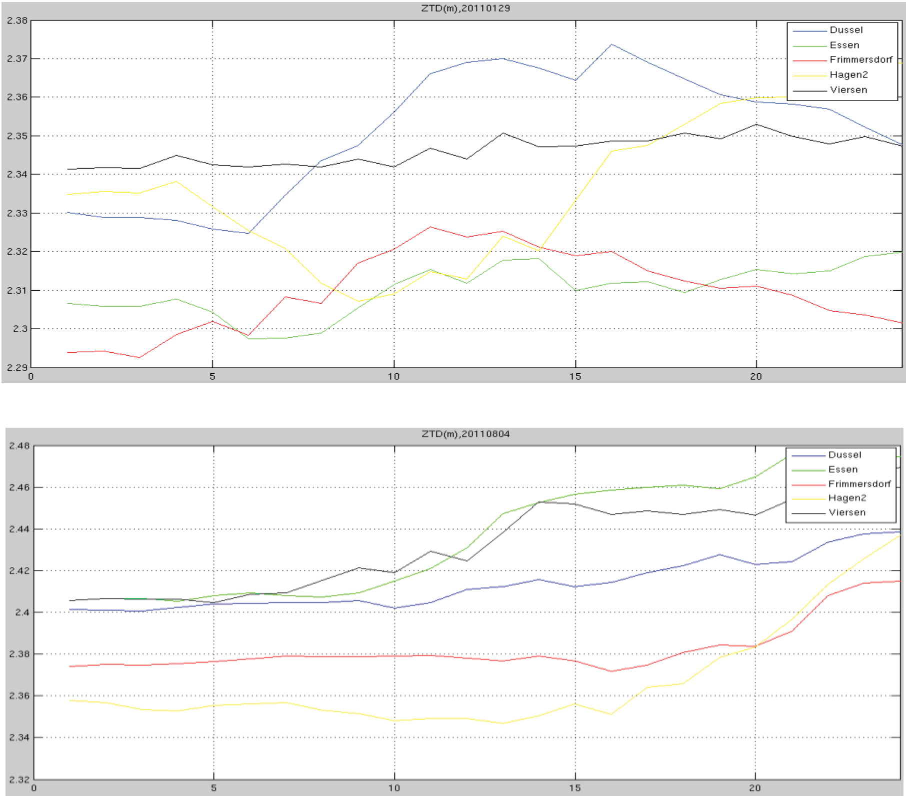

Figure 4.13 Time series of ZTD calculated at 5 sites. The upper graph plots ZTD variations during a day in winter while the lower one in summer.

Additionally, Figure 4.14 shows the ZWD at Düsseldorf station during nearly one year. The sampling time is at 05:50 UTC when the TerraSAR-X satellite takes images at this area. We can see a general trend that ZWD increases from winter time to summer and reaches to the highest point in summer, and then starts to decrease from summer to winter.

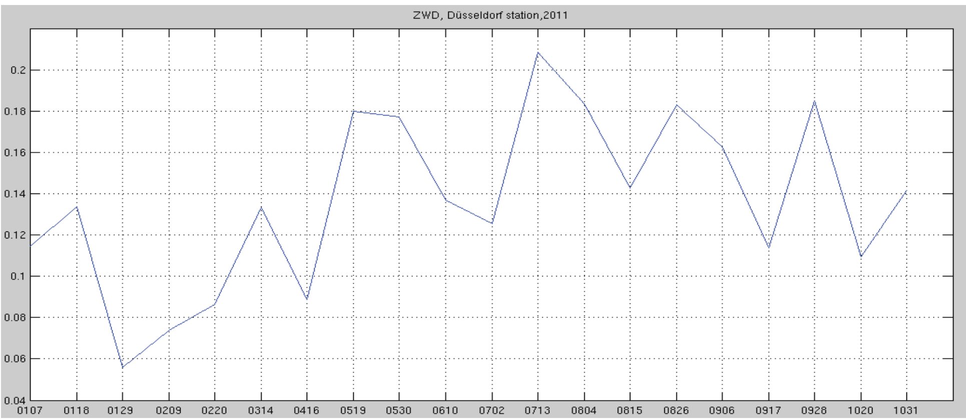

Figure 4.14 Time series of ZWD at Düsseldorf site during one year. X axis indicates the dates when Y axis indicates ZWD in meters.

Corresponding to the dates of SAR acquisitions, GPS-derived ZWD at 05:51am (average value of 5 minutes) on 18th Jan and 29th Jan, 2011 were estimated and then differenced. Subsequently, interpolation was carried out using values at 5 stations. There are lots of interpolation methods such as Krige, Ordinary Kriging and Inverse Distance Weighting (IDW) method, while IDW was used here.

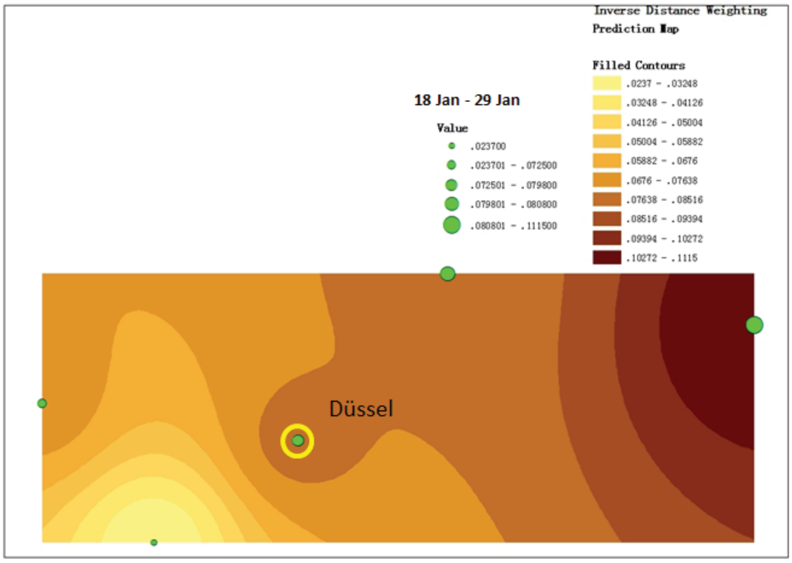

Figure 4.15 Differenced ZWD retrieved from GPS on 18th Jan and 29th Jan, 2011.

We also tested the accuracy of IDW by interpolating ZWD values of the other four adjacent stations to obtain the objective ZWD at station Düsseldorf. The result shown the interpolated value is 0.055866 m when the true value is 0.0798 m, with a consistency of 71%.

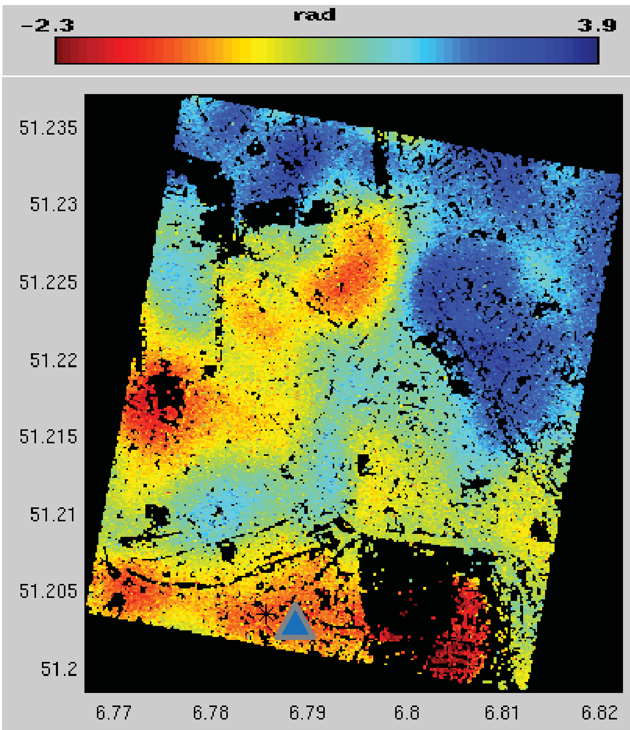

Figure 4.16 APS retrieved from InSAR on 18th Jan and 29th Jan, 2011. Blue triangle indicates the Düssel-GPS station.

The atmospheric effect caused by dry gases is comparatively stable so that it could be eliminated during InSAR processing. The Atmosphere Phase Screen (APS) evaluated from PSInSAR processing is mainly wet delay in line of sight, which can be mapped to the zenith direction by the relationship $ZWD = SWD \times \cos\theta_{inc}$. As long as the Slant Wet Delay (SWD) estimated by PSInSAR has been converted to ZWD, we are able to compare it with the ZWD derived by PPP.

In order to validate PPP estimation carried out in this study, parts of RINEX files were processed by CSRS-PPP service as references. According to ZTD retrieved from InSAR on 18th Jan and 29th Jan, 2011 by CSRS-PPP, ZWD difference could be calculated to be 0.078 m, which indicated a good agreement with that estimated by GIPSY (0.0798 m).

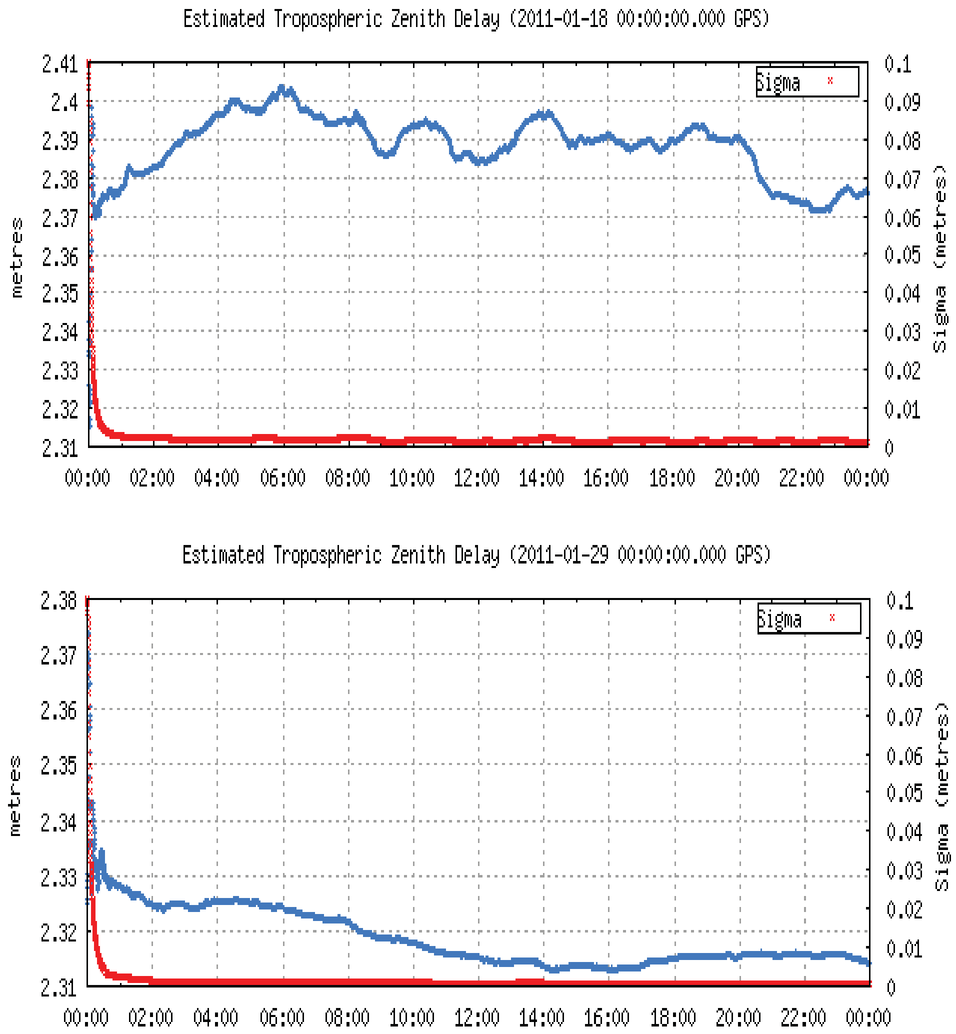

Figure 4.17 ZTD retrieved from InSAR on 18th Jan and 29th Jan, 2011 by CSRS-PPP.

The comparison between differenced ZWD derived from PPP and InSAR at the Düssel-GPS station was done. PPP-derived ZWD is much bigger than the InSAR one. We surmised several possible reasons:

- Various weather conditions on these two days may lead to ZWD changes at totally different degrees that are too various to be detected by InSAR correctly. The mean temperature on 18th Jan was 7.1°C and −2.2°C on 29th Jan. Besides, 7.5 hours Sunshine was observed on 29th Jan but nothing on 18th Jan.
- More likely, part of ZWD delay correlated to elevation was eliminated during interferometric processing.

4.9 Summary

Evaluation of InSAR application to urban area was presented in this chapter. Totally 32 interferograms were formed from the 20 TerraSAR-X images and processed by SBAS-InSAR method integrated in StaMPS. The aim is to monitor the effect to ground surface of a tunneling in Düsseldorf city in 2011. The comparison between time series retrieved from SBAS-InSAR and from leveling of a control point indicated good consistency. It is therefore no doubt that InSAR is able to detect insignificant movements (in the order of mm) in urban area, by restraining various error resources. Moreover, we tested if GPS-derived ZWD could be used for reducing atmospheric effect based on five GPS stations. The result of this test is smaller than PSInSAR derived. The reason could be that some ZWD delay was removed as, e.g., elevation error, during InSAR processing as it is correlated to elevation. However, there is a potential of integration of two techniques because InSAR is able to measure ZWD over an area but with relative values between different passes, when GPS/PPP can do the complementary measurement: to measure ZWD on dispersed points but with absolute values.

Chapter 5 Application to Mining Area

5.1 Introduction

Xishan coal mine is located in Shanxi Province, China. There are eight active mines in this area, with a total coverage of 304.8 square kilometers. This coal mine is owned by Xishan Coal and Electricity Power Group Company Limited, which is China's largest and the world's second largest coking coal production enterprise. These eight mines can be divided into two parts, the front part with four mines (left part in the figure) and back part with three (with red colour). In this research, we will study the front part only.

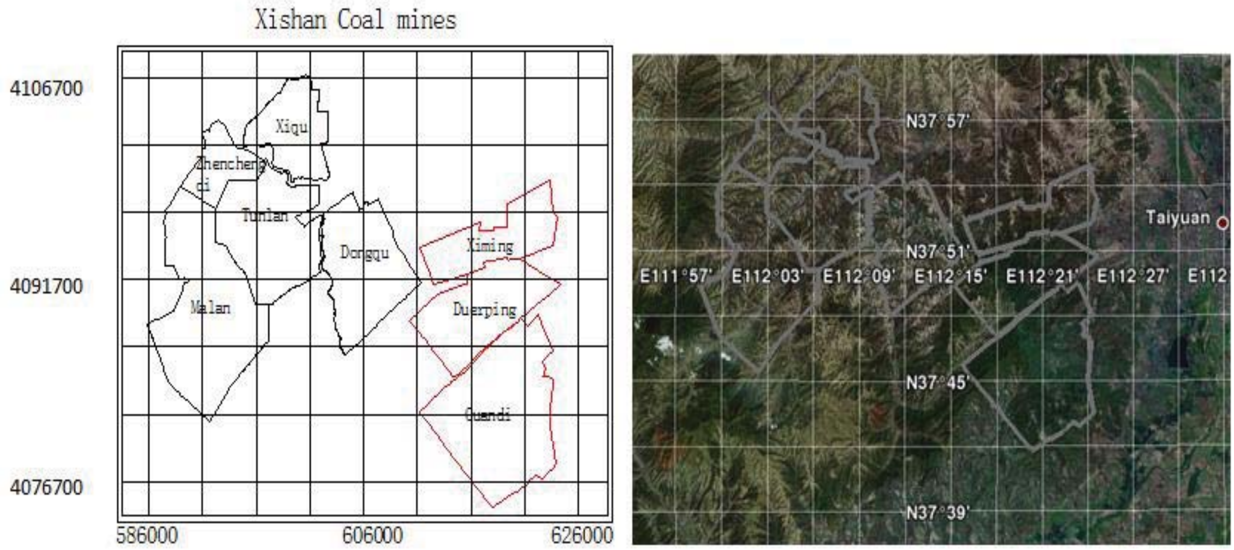

Figure 5.1 Left: xishan coal mines (in UTM), Taiyuan, Shanxi Province. Right: coal mines on google earth.

5.2 Geography

Three-quarters of this area feature large mountains with steep slopes and ravines, which are mainly composed of Carboniferous, Permian sandstone, shale and Quaternary loess (Liu et al., 2012). Landslides, debris flows and avalanches are quite common in this area. The highest altitude is 1736 m while the lowest is 729 m in this area (Fig. 5.2). As the relative altitudes among these mountains are 500m to 800m, SAR images of such area will are greatly distorted by the oblique imaging geometry of a side-looking radar, often causing layover and shadow effects.

Rather than threes, grasses and bushes are common in this area, and mountains are with big relative altitudes (Fig. 5.3). They may affect the signal of TerraSAR-X as its wavelength is relative short.

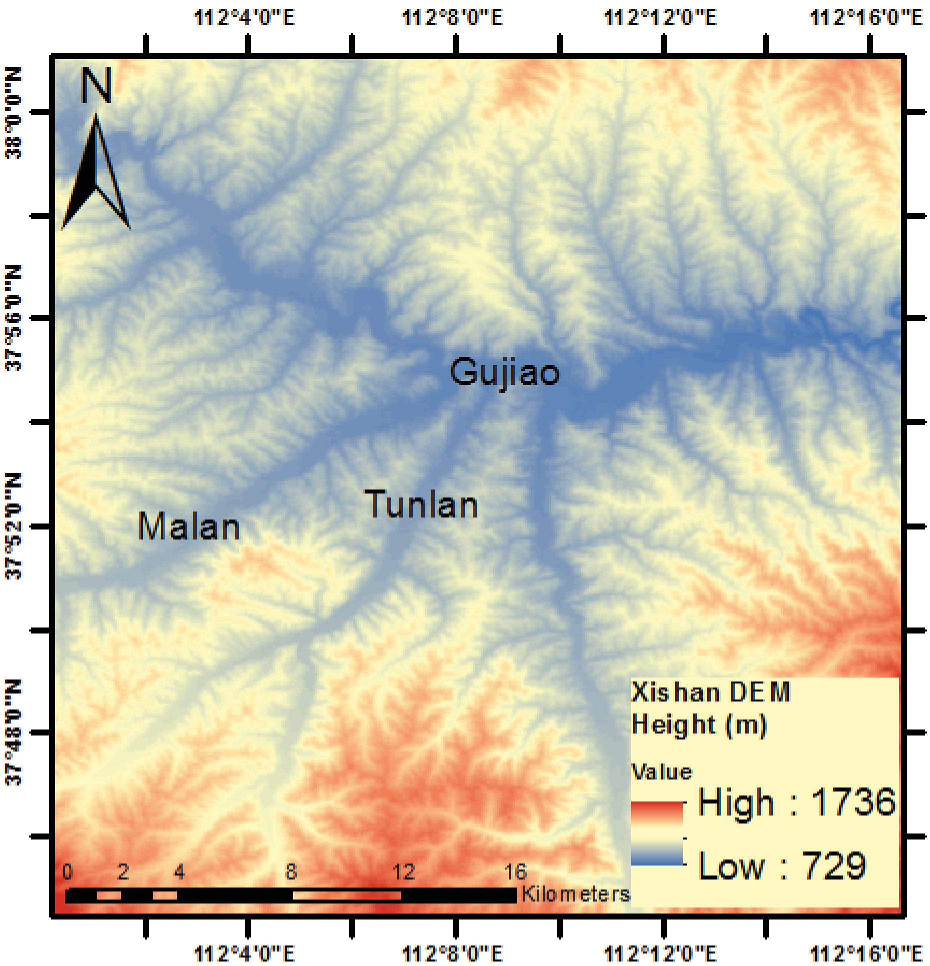

Figure 5.2 Digital Elevation Model of the research area cropped from SRTM.

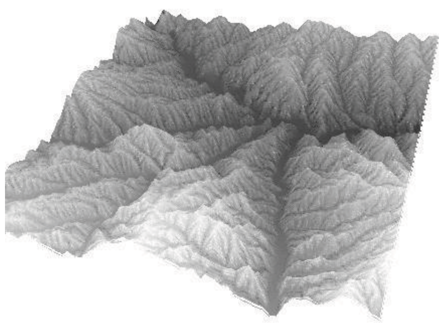

Figure 5.3 Left: Xishan's geography shown by 3-D DEM (5 times exaggerated); Right: A view of Xishan's geography.

5.3 Climate

Like the whole Taiyuan region, this coal mine area experiences a semi-arid climate. Most of the year's rainfall concentrated in the July and August when summer is coming with hot weather. Winter is cold but dry and sunny, sometimes with snow. As aridity is a common problem here, mining activities bring serious challenges to the natural environment.

5.4 Potential Geo-hazards Induced by Mining Process

Due to the poor natural geological environment coupled with intensive mining activities, a lot of geological disasters such as subsidence, landslides, debris flows and avalanches happened in this area.

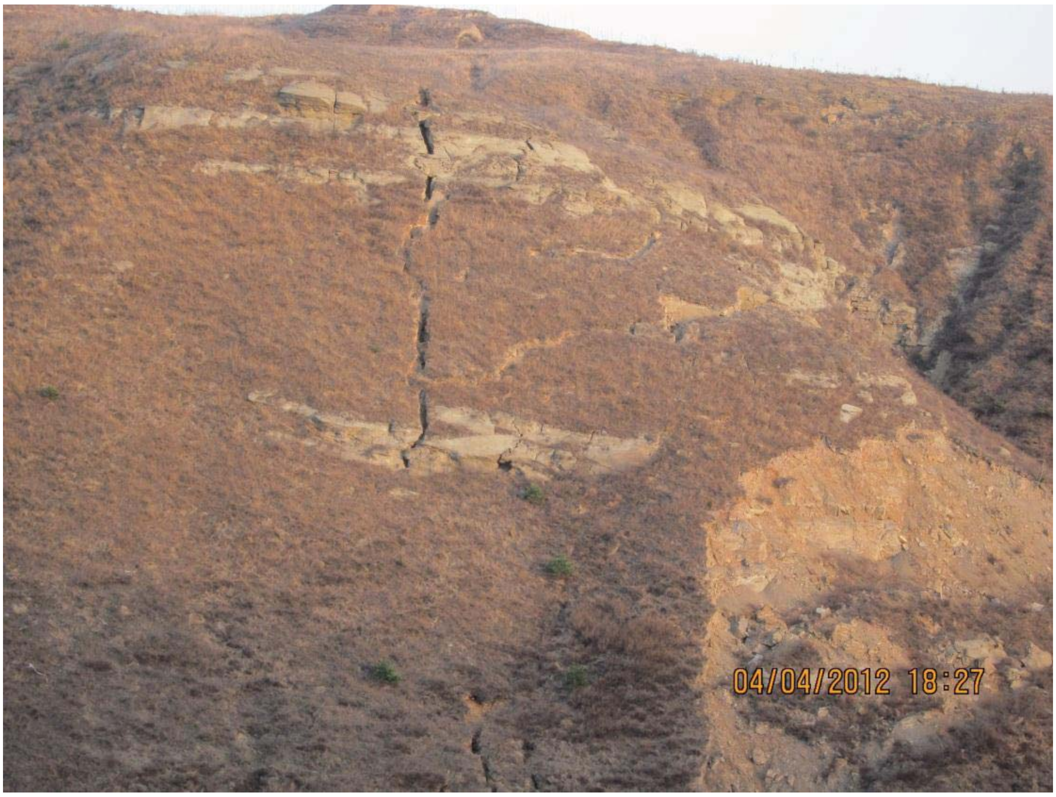

Figure 5.4 One potential geohazard.

In recent years, upper coal seams are depleting and most of the mining activities turned to the lower seams for future work (Liu and Bian, 2012). Therefore, the rock strata and ground surface above are experiencing the second disturbance, so-called repeated mining. The second disturbance always increases and extends damages that new crevices are formed and could lead to discontinuous deformation such as big fractures and steps, which usually arise accidentally and could pose great hazards to the living, production safety and environment. One challenge is that researches on repeated mining in such wide area have not been carried out before and few results can be found in public literatures. In other words, this project is full of research value and a breakthrough can be expected in disclosing laws of large-scale subsidence under repeated coal excavation.

5.5 SAR Data

As mentioned previously, the Japan Aerospace Exploration Agency (JAXA) launched the ALOS satellite in 2006 which contained a Phased-Array L-band SAR (PALSAR). The characteristics of Fine Beam Single Polarisation (FBS) mode of PALSAR are summarised in table 5.1, as FBS is the most common for interferometric applications. Four Level 1.1 Single Look Complex (SLC) ALOS images, provided in CEOS data format were collected from 2008 to 2010 (Liu et al., 2012). Data specifications are shown in Table 5.1.

Table 5.1 Basic characteristics for ALOS PALSAR in FBS mode used.

Frequency	1270MHz (L-Band)
Wavelength	23.6cm
Polarisation	HH or VV
Swath Width	40-70km
Incidence Angle	8-60 degrees
Range resolution	7-44m
Orbit Repeat Cycle	46 days
Orbit Type	Polar, Sun-Synchronous
Orbit Altitude (at Equator)	692km
Precise Orbit Accuracy	< 1m

The baseline characteristics of the four images are shown in Table 5.2 below, the orbital baseline being the distance between the satellite and master positions and the temporal baseline being the time separation between the two. Unlike other sensors, ALOS L1.1 products are not zero-Doppler. The consequence of that is the geometric model used during the processing is slightly different and varies from product-to-product (Liu et al., 2012). Although the variation can be negligible, in general this is not the case and thus a slightly modified processing chain must be applied. An improved algorithm in Punnet was developed by Andrew Sowter in 2010 to cope with this.

Table 5.2 Specifications of ALOS data used.

Acquisition Date	Spatial baseline (m)	Temporal baseline (days)
2008.02.04	1554.62	-690
2008.12.22	-2363.3	-368
2009.12.25(**master**)	0	0
2010.02.09	600.203	46

In addition, 8 ENVISAT ASAR scenes were collected, as listed in Table 5.3 and 5.4. The baselines are controlled so that only pairs with short baselines will be processed. The wavelength of ENVISAT ASAR is 5.6 cm. Both spatial and temporal baselines are shown below (Fig. 5.5).

Table 5.3 Basic characteristics for ENVISAT ASAR data.

Frequency	5.331 GHz (C-Band)
Wavelength	5.6cm
Polarisation	VV, HH,VV/HH, HV/HH, or VH/VV
Swath Width	Up to 100km
Incidence Angle	15-45 degrees
Range Resolution	30 m
Orbit Repeat Cycle	35 days
Orbit Type	Polar, Sun-Synchronous
Orbit Altitude (at Equator)	800 km
Precise Orbit Accuracy	Centimeters

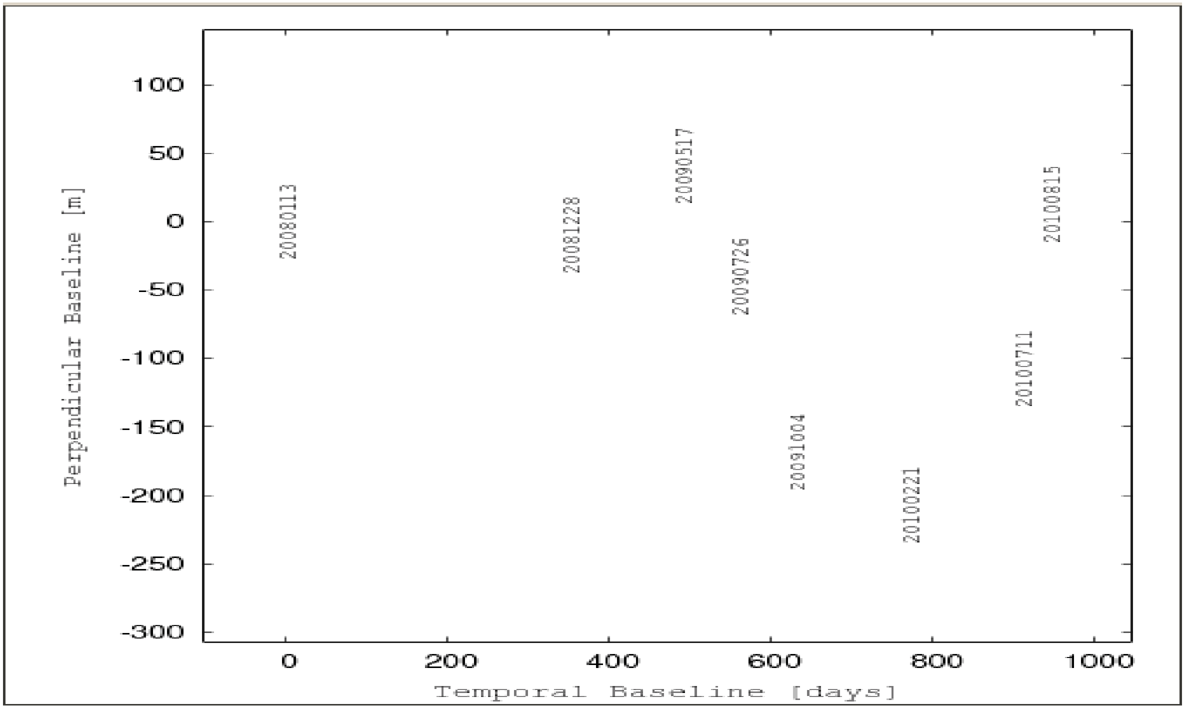

Figure 5.5 Baselines of ENVISAT data set.

Table 5.4 Specifications of ENVISAT data used.

No.	Acquisition Date	Spatial baseline (m)	Temporal baseline (days)
1	2008.01.13	169.949	-630
2	2008.12.28	160.887	-280
3	2009.05.17	207.693	-140
4	2009.07.26	128.783	-70
5	2009.10.04 (**master**)	0	0
6	2010.02.21	-38.919	140
7	2010.07.11	62.2254	280
8	2010.08.15	177.955	315

Table 5.5 and Figure 5.6 are the specifications and baseline information of 21 TerraSAR-X images used in this study. By selecting the image acquired on 2012.05.18 as the master image, baselines of other 20 scenes related to the master image were calculated. According to the estimation, most perpendicular baselines were controlled between -100m to 150m, which are obviously advantageous for deformation monitoring.

Table 5.5 Specifications of TerraSAR-X data used.

No.	Acquisition Date	Spatial baseline (m)	Temporal baseline (days)
1	2012.4.4	32	-44
2	2012.4.15	11	-33
3	2012.4.26	-131	-22
4	2012.5.7	113	-11
5	**2012.5.18 (master)**	**0**	**0**
6	2012.5.29	-22	11
7	2012.6.9	-34	22
8	2012.6.20	154	33
9	2012.7.1	76	44
10	2012.7.12	8	55
11	2012.7.23	165	66
12	2012.8.3	148	77
13	2012.8.14	-7	88
14	2012.8.25	50	99
15	2012.9.5	-56	110
16	2012.9.16	96	121
17	2012.9.27	93	132
18	2012.10.8	86	143
19	2012.10.19	16	154
20	2012.11.10	-15	165
21	2012.11.21	48	176

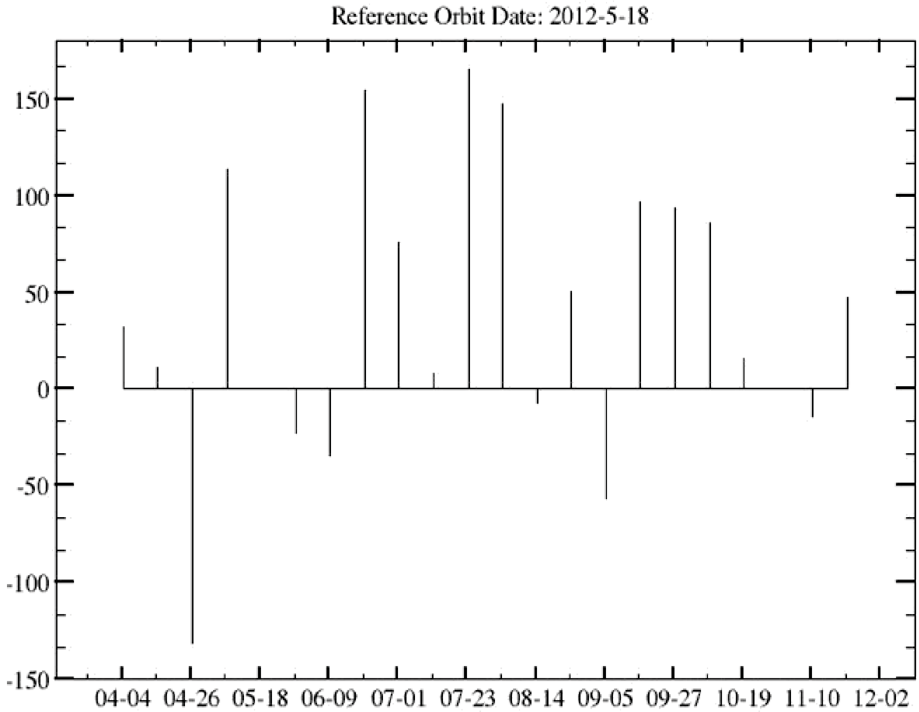

Figure 5.6 Baselines of TerraSAR-X data set.

Due to its high resolution and short revisit cycle (Table 4.1), TerraSAR-X may offer some potential opportunities for earth observation. In order to see how TerraSAR-X can work with big displacements in mountainous area, processing of this data set will be accounted for the major part in this study.

5.6 GPS Observations

GPS surveying was carrying out (Liu and Bian., 2012) when the acquisitions of TerraSAR-X images were ongoing. Besides, Corner reflectors are installed on stopingfaces, which could be useful for checking and enhancing geocoding performance, and orbit refining as well during InSAR processing. All GPS measurements correspond to the corner reflector network. Due to Chinese Surveying Law, the coordinates are not provided. Only the relative displacements measured by GPS were used in the validation of InSAR observation.

Figure 5.7 Left: Concrete fundamental for installing corner reflectors; Right: GPS measurement of a corner reflector.

5.7 Corner Reflector Network

Corner reflector network was used based on two main considerations. Firstly, geocoding is one of the most important issues in InSAR processing, when the aim is detecting the boundary of mining effects. Furthermore, the corner reflectors are able to provide a very stable target response of both amplitude and phase to the satellite-based radar. They could overcome de-correlation effects of conventional InSAR to a certain degree.

In order to reach the maximum radar cross section, orientation of the corner reflectors has to be determined and set, and make sure that the symmetry axis of CRs and the radar sight line are overlapped with each other (Xia, 2008). The azimuth angle β of the radar sight line is:

$$\beta = arcsin\left(\frac{\mp cos\alpha}{cos\xi}\right) \qquad (5.7.1)$$

where α is the inclination of the orbit plane, ξ is the geodetic latitude of the corner reflector. '-' is for ascending and '+' is for descending orbit.

Figure 5.8 Field work of setting up corner reflectors.

Besides, some other points are carefully considered when setting up the corner reflector network, according to the geography and working situation in this area.

- Make sure that the radar can 'see' the corner reflectors at any time. To avoid the radar signals to the corner reflectors being affected by mountains or trees around.
- We should select the locations of corner reflectors that are easy to access for GPS measurements, and make them away from high-tension transmission lines.

Totally, a network with 27 corner reflectors was arrayed. Figure 5.9 shows the distribution of this network, and the pink area means the coverage of front part of Xishan coal mine.

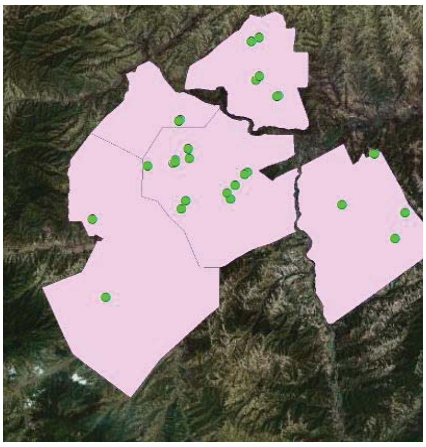

Figure 5.9 Distribution of CR network in Xishan area.

5.8 Data Analysis and Discussion

5.8.1 Topographic analysis with TerraSAR-X data

As with photogrammetry, the images of side look radar have geometric distortions which are caused by topographic relief displacement. They are foreshortening, layover and shadow.

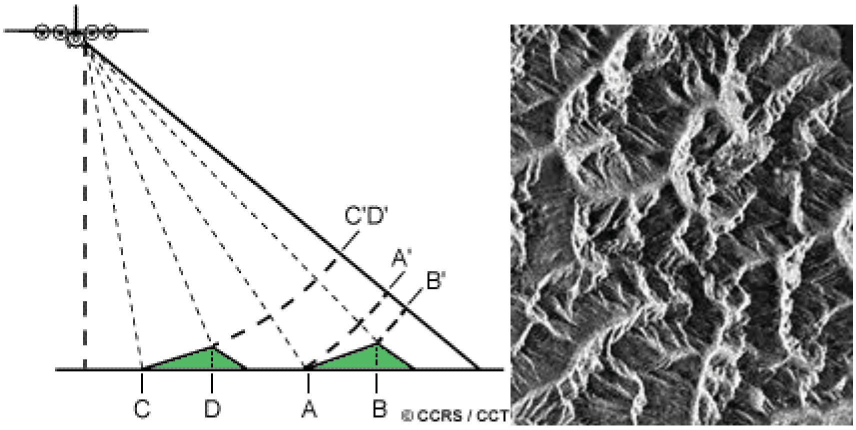

Figure 5.10 Foreshortening. From website of Natural Resources Canada, available on 8th March, 2013.

In the radar image, points A and B will appear much closer (A' to B') than in reality (A to B). In other words, the length of the slope will be compressed. In the extreme case that the radar beam is perpendicular to the slope, point C and D are imaged simultaneously and they are indistinguishable as the path lengths are the same. In practice, the slopes with foreshortening always appear as bright features (Figure 5.10, image on the left).

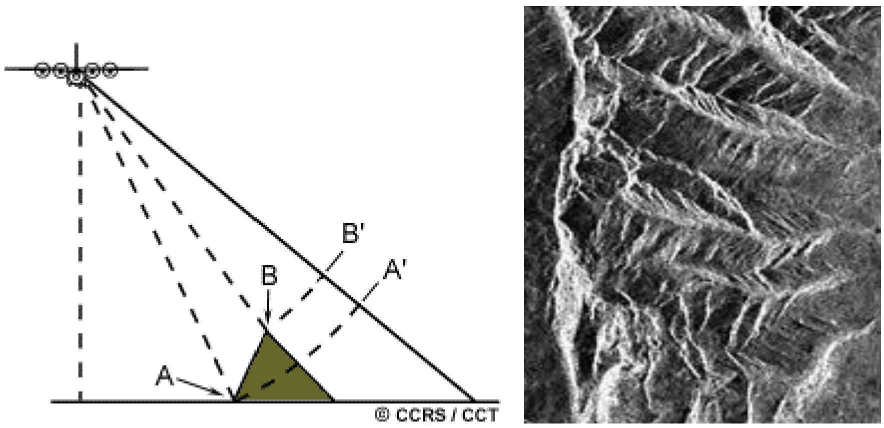

Figure 5.11 Layover. From website of Natural Resources Canada, available on 8th March, 2013.

Figure 5.11 shows the layover effect of a slope. The radar signal reaches the top (B) before it reaches the bottom (A). Consequently, the return signal from the top of the slope (B') will be received before the signal from the bottom (A'). Therefore, the top of the slope lay over the base of the slope. Apparently, layover is a more extreme case of foreshortening. In fact, layover on a radar image looks very similar to foreshortening effects.

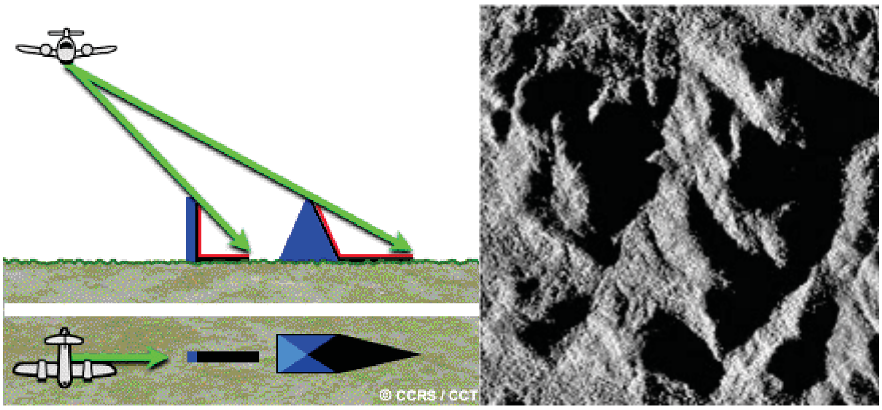

Figure 5.12 Shadow. From website of Natural Resources Canada, available on 8th March, 2013.

Shadow occurs when the radar can't 'see' one side of a feature. Shadowed areas usually appear dark on an image as these regions are unable to be illuminated by the radar and thus no signal is going to be backscattered. Therefore, dark areas in the image are affected by shadow and contain no information (Fig. 5.12).

The topographic analysis included the generation of ortho-images which allows for the integration of the SAR data within GIS and the generation of layover masks, which identify the anomalous areas in the image caused by perspective (Liu et al., 2012). The results for the ENVISAT images are shown in Figure 5.13 in both original slant-range and map coordinates. It is clear from the figure that the amount of distortion caused by the oblique view of the radar is extensive and the severity of the terrain produces a lot of layover. Layover appears in thin lines in the slant range image but, when rectified, occupies a large part of the image. In the presence of layover, no meaningful information can be gathered meaning that no landslide or deformation measurements exist in these areas and the mask should be applied to all results. The shadow mask is not shown as it affected almost a negligible number of pixels.

A comparison between the slant-range and ortho-rectified images showed that there is severe distortion in the imagery. For example, several of the mountain peaks are displaced more than 1km along the ground by foreshortening. In addition, although only around 7% of the slant-range pixels are in layover, this area actually accounts for more than 25% of the area on the map following ortho-rectification. Clearly, layover must be taken into account for any InSAR or PSI analysis of this region.

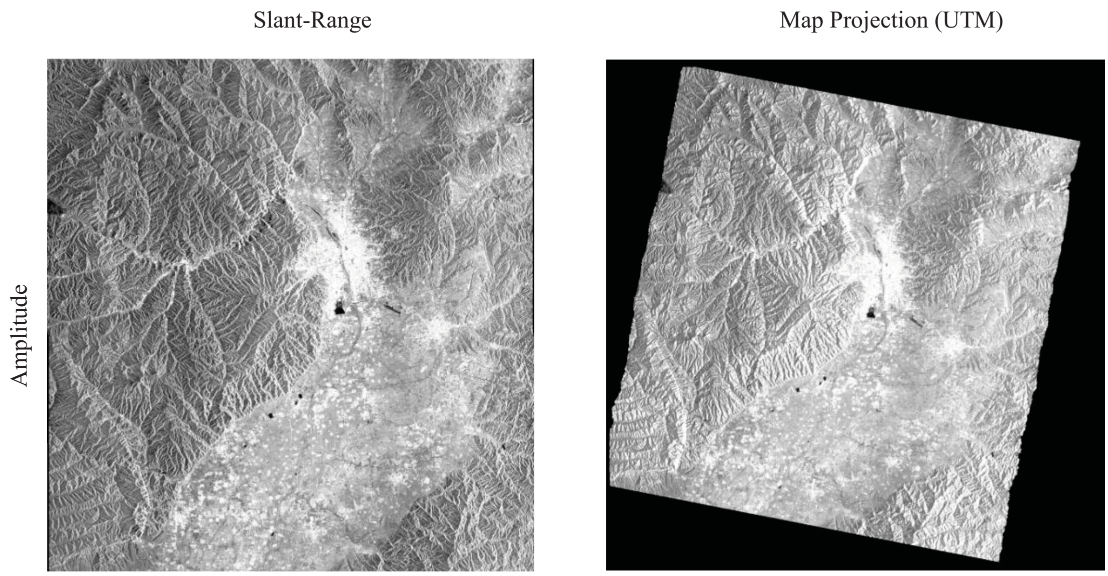

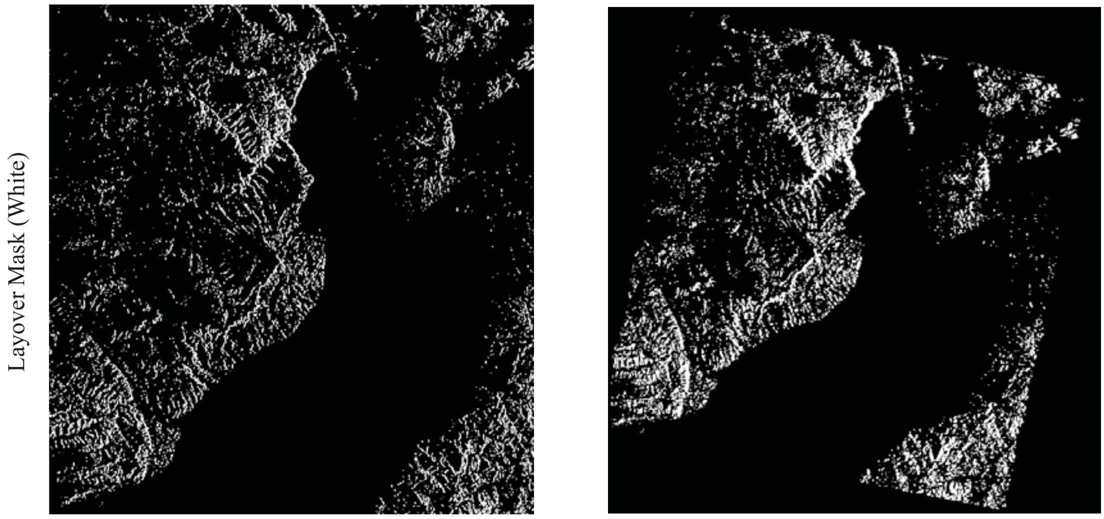

Figure 5.13 Amplitude images and layover masks of the full ENVISAT image (100km x 100km).

As pointed out by Sowter in 2010, due to the extreme influence of terrain variations on the oblique slant-range SAR geometry, mountains always cause problems with SAR data. Hence, it is necessary to orthorectify the images, to correct for perspective distortions and to identify areas of layover and shadow. Figure 5.14 shows the effect of topographic distortion on the SAR data and also the extent of layover in the full scene. The black areas are affected by these layovers.

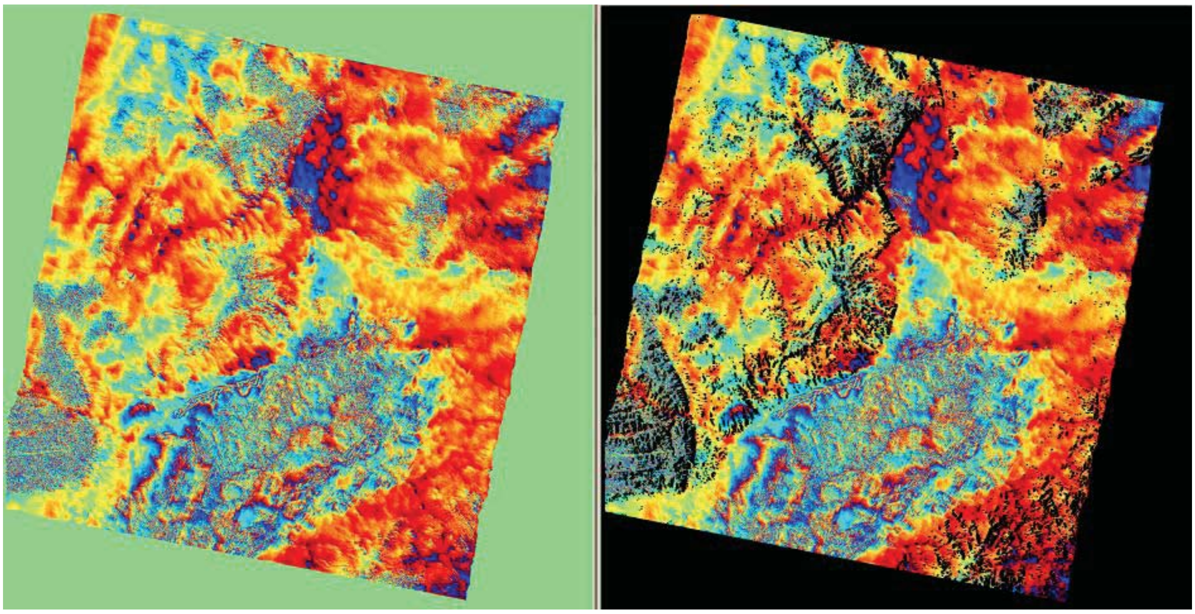

Figure 5.14 Left: Orthorectified interferogram; Right: Orthorectified interferogram with layover. (Pair 2008.12.28-2009.05.17)

Apart from radar image distortions, a more important point is how topography will affect interferogram phase in InSAR processing. In figure 2.6, the phase corrected for the curved earth effect is:

$$\phi_{flat} = -\frac{4\pi}{\lambda} B\cos(\theta_0 - \alpha)\Delta\theta = -\frac{4\pi}{\lambda} B_{\perp 0}\Delta\theta \qquad (5.8.1.1)$$

$$\frac{d\phi_{flat}}{d\theta} = -\frac{4\pi}{\lambda} B_{\perp 0} \quad (5.8.1.2)$$

where $B_{\perp 0}$ is the perpendicular baseline, θ_0 is the look angle, they are both relative to the reference ellipsoid. $\Delta\theta$ is the angular distortion due to the topography, α is the angle of the geometry baseline with respect to the horizontal, B is the baseline, λ is the wavelength. Besides, we can obtain the geometric relationship:

$$h = H - \rho cos\theta \quad (5.8.1.3)$$

$$\frac{dh}{d\theta} = \rho sin\theta \quad (5.8.1.4)$$

where H is the ellipsoid height of S_1, h is the ellipsoid height of point P on the Earth.

By combining equation (5.8.1.2) and (5.8.1.4), one can obtain the equation:

$$\frac{dh}{d\phi_{flat}} = \frac{dh}{d\theta}\frac{d\theta}{d\phi_{flat}} = -\frac{\lambda}{4\pi}\frac{\rho sin\theta}{B_{\perp 0}} \quad (5.8.1.5)$$

Thus:

$$h = -\frac{\lambda}{4\pi}\frac{\rho sin\theta}{B_{\perp 0}}\phi_{flat} \quad (5.8.1.6)$$

People define the altitude of ambiguity h_a as the magnitude of topography. The smaller h_a, the more sensitive the interferogram phase is to height changes.

$$h_a = \left|\frac{\lambda}{4\pi}\frac{\rho sin\theta}{B_{\perp 0}}2\pi\right| = \left|\frac{\lambda}{2}\frac{\rho sin\theta}{B_{\perp 0}}\right| \quad (5.8.1.7)$$

According to equation (5.8.1.7), the interferogram phase is sensitive to the topography when the perpendicular baseline is large. For instance, pair 20120404-20120415 and pair 20120404-20120426 were processed by conventional DInSAR approach. These two pairs have a common master image 20120404, and small variations of time span (11 days). However, the perpendicular baseline of pair 20120404-20120415 is 21 m while that of pair 20120404-20120426 is 142 m. It is logical that pair 20120404-20120426 got much more fringes (Figure 5.15, right) in the interferogram with curved earth effects removed than pair 20120404-20120415.

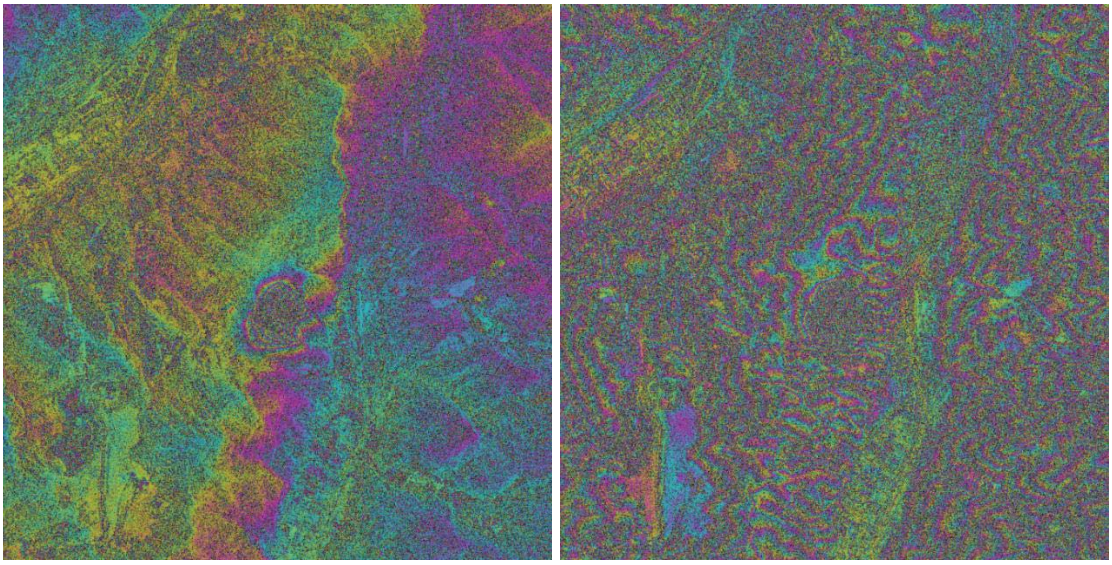

Figure 5.15 Left: flattened interferogram, pair 20120404-20120415, $B_{\perp} = 21$ m. Right: flattened interferogram, pair 20120404-20120426, $B_{\perp} = 142$ m.

Unfortunately, the strong topographic effects could not be eliminated from the interferogram formed by 20120404-20120426 using an external DEM (90 m resolution SRTM here). As a result, deformation signals were contaminated by the topographic effects in the interferogram 20120404-20120426, and subsidence was not able to be detected as clear as in the interferogram 20120404-20120415 (Fig. 5.16, left).

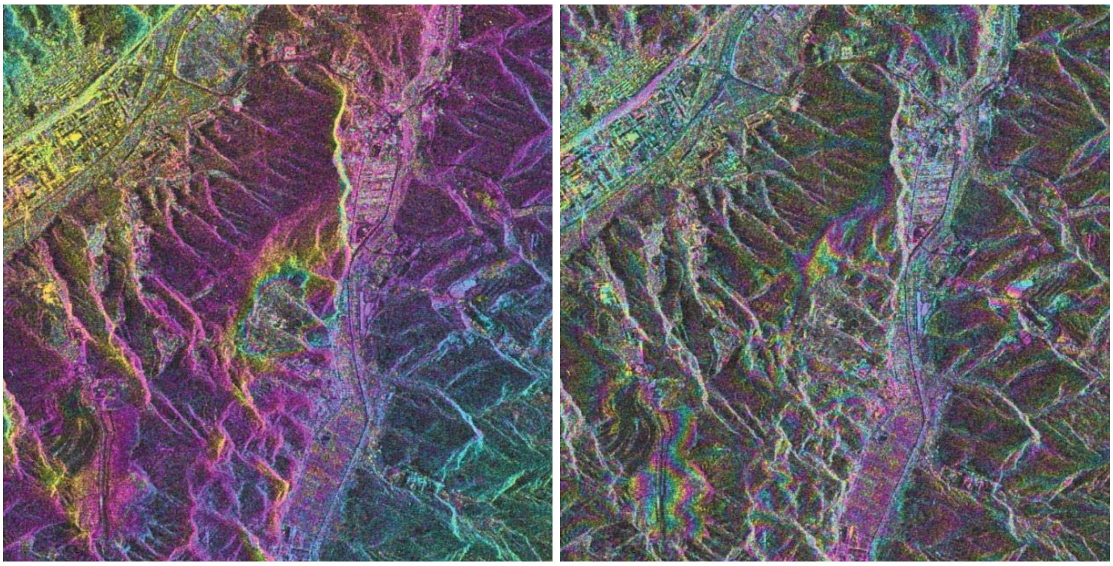

Figure 5.16 Interferograms with topography removed by SRTM DEM, shown with intensity maps. Left: pair 20120404-20120415, $B_{\perp} = 21$ m. Right: pair 20120404-201204206, $B_{\perp} = 142$ m.

5.8.2 De-correlation factors

As discussed before, coherence provides an evaluation of the reliability of the phase values. Several factors limit coherence and result in so-called de-correlation in interferometric images. Particularly, the interferometric coherence loss will be affected by changes in the viewing perspective (spatial or baseline de-correlation), as well as by variations of the reflectivity of the objects (temporal de-correlation).

Temporal de-correlation. Surface changes (deformation) and the change of scatterer characteristics with time lead to temporal de-correlation. For instance, the seasonal changes of vegetation or weather conditions like snowfall may cause big changes in surface characteristics. Thus, InSAR pairs will not be 'coherent' but get 'de-correlation' if surface changes are serious. In our research area, an important source of de-correlation could be rapid subsidence caused by mining activities with high intensities. Because pixels in a radar image are formed by the sum of the many backscatters rather than a single one, temporal de-correlation can also be introduced by the relative movements of the scatterers within one SAR resolution cell, which occurred widely in Xishan. In short, temporal de-correlation results from complex effects of the various characteristics of the surface.

The temporal de-correlation problem can be mitigated by using the information of phase stable targets: rocks, buildings, or even gravel, as the sum phase of the resolution cell will be dominated by one stable scatterer. This is also what PSInSAR approaches normally use. A popular anthropogenic infrastructure, corner reflectors were installed for this purpose in our study. Both passive and active radar reflectors have been used in practice. A passive reflector can be constructed using metal panels directly, when an active reflector requires a receiver and transmit antennas, an amplifier, and power source. Both kinds of corner reflectors performed well in the past experiments so that passive reflector is used more frequently due to its low cost.

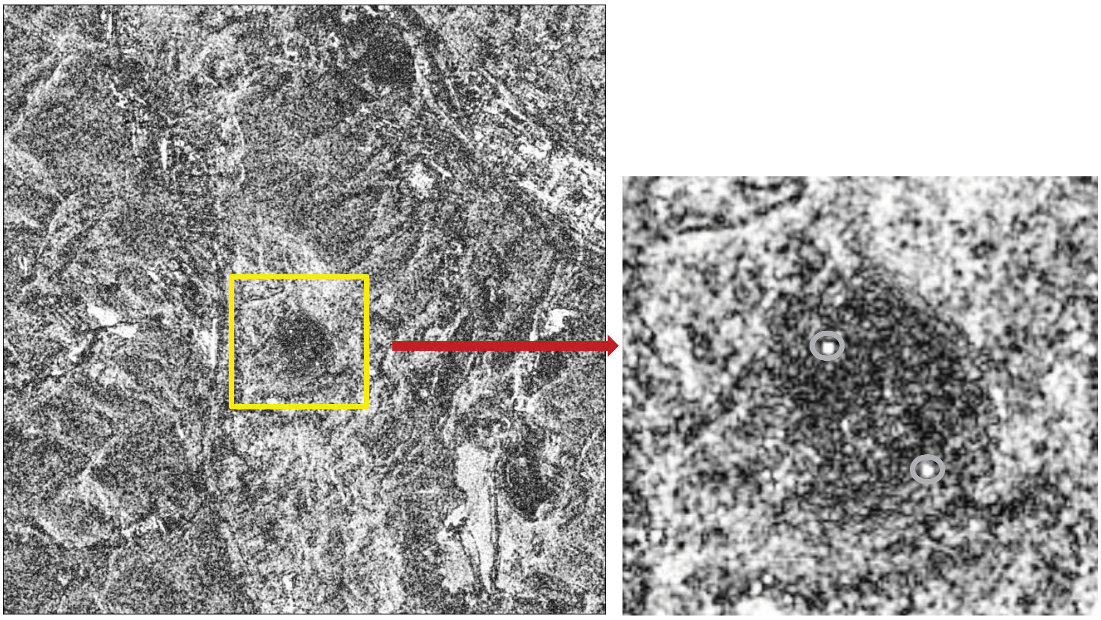

Figure 5.17 Two corner reflectors (bright points) on coherence image, pair 20120404-20120415. Yellow rectangle shows the subsidence area and blue circles indicate the corner reflectors.

Figure 5.17 shows a coherence map of pair 20120404-20120415. Dark colour means low coherence while white colour means high coherence. The central area shown on the map was affected by strong mining activities so that big surface changes occurred and then result in de-correlation problem. However, two bright points locating inside the subsidence area can be easily found. That means, with the help of corner reflectors, deformation signals may be derived correctly even all surrounding area got coherence loss.

One has to keep in mind that corner reflectors will solve the temporal de-correlation problem only in some cases. In the coherence image of pair 20120404-20121121 with a big time span, only one corner reflector but not two as in that of pair 20120404-20120415 can be seen clearly from the image. Besides, most areas in the coherence image of pair 20120404-20121121 are in dark colour which means coherence loss happened for a long time resolution with 220 days.

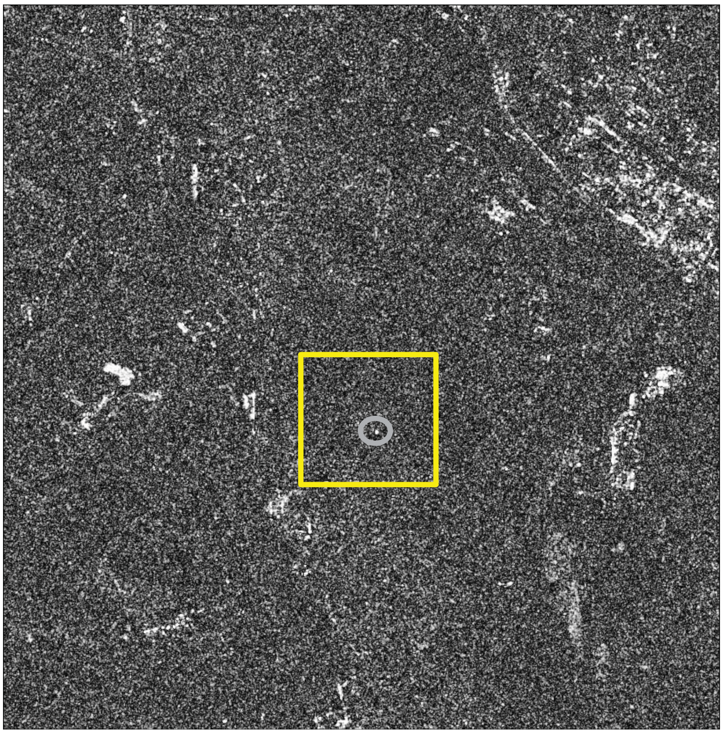

Figure 5.18 Coherence image of pair 20120404-20121121. Yellow rectangle shows the subsidence area and blue circle indicates the corner reflector.

Spatial de-correlation (Baseline de-correlation). As we know, the phase varies with different viewing geometries. The viewing geometries are determined by the orbit positions in different satellite passes, or in other words, the satellite baseline. This maximum baseline that allows satellite observations to be used for InSAR processing is called the critical baseline, which is dependent on the radar wavelength, the resolution, the incidence angle, and also the distance between the satellite and objects. System with higher resolution (e.g. TerraSAR-X) and longer wavelengths (e.g. S-band or L-band radar) are less sensitive to baseline de-correlation.

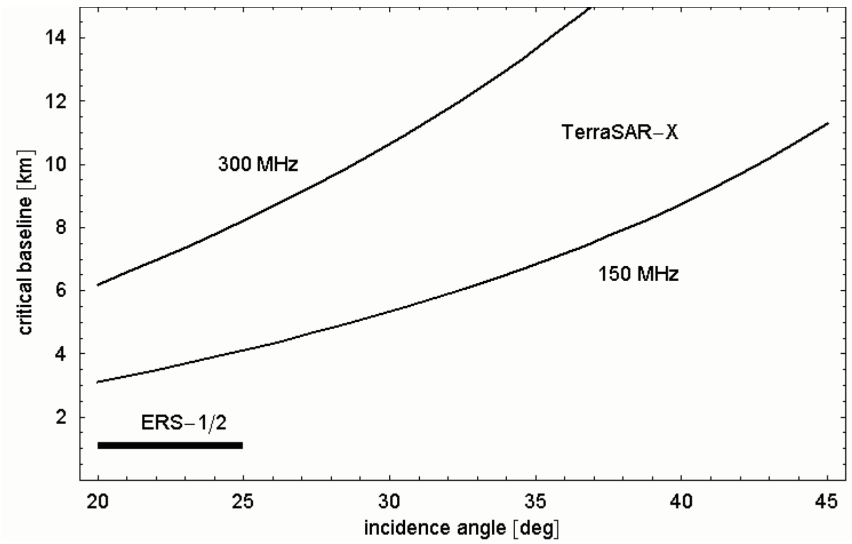

Figure 5.19 Critical Baselines for ERS and TerraSAR-X (Bamler, 2006)

If persistent scatterer that a point target dominates the signal return within a resolution cell is available, then there is no effect from baseline de-correlation. Persistent scatterers, or corner reflectors permit people to use SAR images with larger baselines, and so that improve the time sampling rate.

In Figure 5.19, critical baselines for ERS-1/2 and TerraSAR-X were estimated. Fortunately, all potential baselines in our TerraSAR-X data set with regard to Xishan do not exceed the critical value. Therefore, spatial de-correlation is not a problem as serious as temporal de-correlation in this study.

5.8.3 Archive SAR data analysis

As presented in section 5.5, totally 4 ALOS PALSAR and 8 ENVISAT ASAR archived data were collected during the time span of 2008 to 2010. In order to restrain the spatial and temporal de-correlation, only those pairs with good coherence and good baseline condition were analysed by differential InSAR processing.

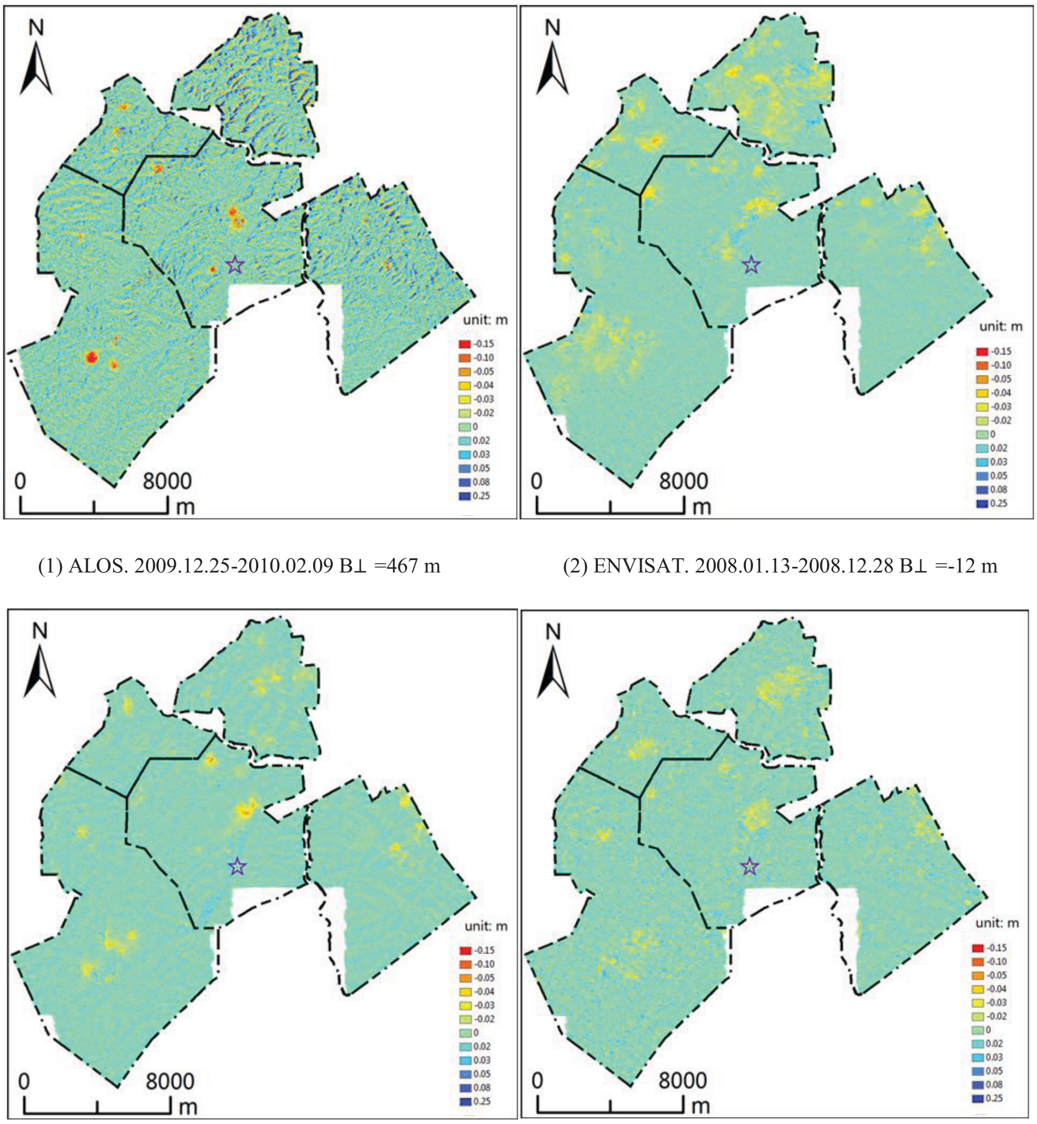

(1) ALOS. 2009.12.25-2010.02.09 B⊥ =467 m

(2) ENVISAT. 2008.01.13-2008.12.28 B⊥ =-12 m

(3) ENVISAT. 2008.12.28-2009.05.17 B⊥=46 m

(4) ENVISAT. 2009.10.04-2010.02.21 B⊥=-42 m

Figure 5.20 Two-Pass DInSAR results with ALOS (1) and ENVISAT (2-4) data. (Liu and Bian., 2012).

Considering both of the baselines and the time spans, subsidence information derived from ALOS using pair 2009.12.25-2010.02.09 (image 1 in Figure 5.20) and from ENVISAT using pair 2009.10.04-2010.02.21 (image 4 in Fig. 5.20) are compared.

In this study, the ALOS data are ascending while ENVISAT are descending. Therefore, in spite of detecting the same displacement, views are different from two images. Besides, L band detected decimeter-level but ENVISAT showed only centimeter-level movements. The reason could be the great phase gradients induced by strong mining activities at this area, when the maximum detectable displacement is one fringe in one pixel. One solution to such problem may be increasing the wavelength and/or reducing the revisit time. According to the information from mining companies, there are several stoping faces being mined during the period of 2009.12.25-2010.02.09. In Figure 5.21 (right), the location of these stoping faces and the time of mining activities are depicted. We see a good correspondence between activities and subsidence.

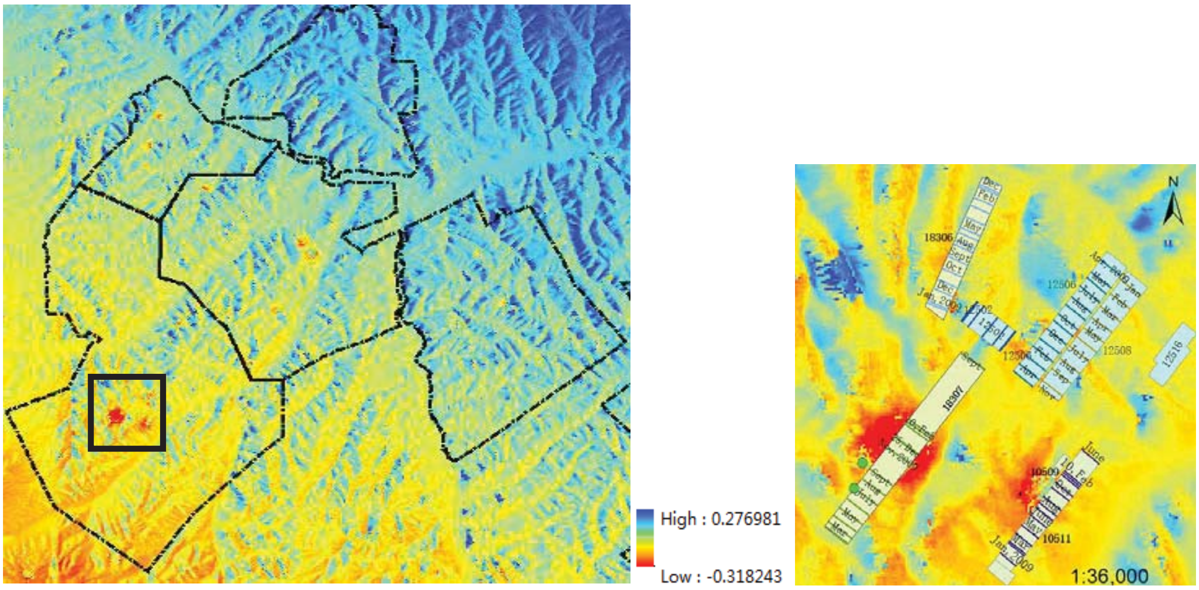

Figure 5.21 Displacement map of ALOS pair 2009.12.25-2010.02.09 (Left) and overlaid with stoping faces (Right).

5.8.4 TerraSAR-X data analysis

As for programmed data, 21 scenes in strip map mode were provided by DLR under the scientific proposal LAN1185. Steep incidence angles were used so as to avoid strong shadow effects in this mountainous area.

Table 5.6 TerraSAR-X parameters used in this study.

Imaging mode	Stripmap	**Incidence angle**	24.766°-28.035°
Polarizations	HH	**Orbit**	Descending
Wavelength	3.1cm	**Imaging area**	30km×50km
Azimuth resolution	3m	**Range resolution**	1.7-3.5m

In the archive data analysis, we have obtained a general impression of the rapid and large deformation in Xishan. Due to the big phase gradients, deformation signals could not be derived by phase unwrapping correctly. On the other hand, persistent scatterers candidates are absent in many regions when applying PSInSAR processing. It is easily explicable that many blank areas (without PS point) appeared in Figure 5.22, because such areas were suffering strong subsidence, and the ground surface changes severely so that no phase-stable point is selectable. In these bland areas, no information can be obtained even we know such areas may coincide with the mining activities.

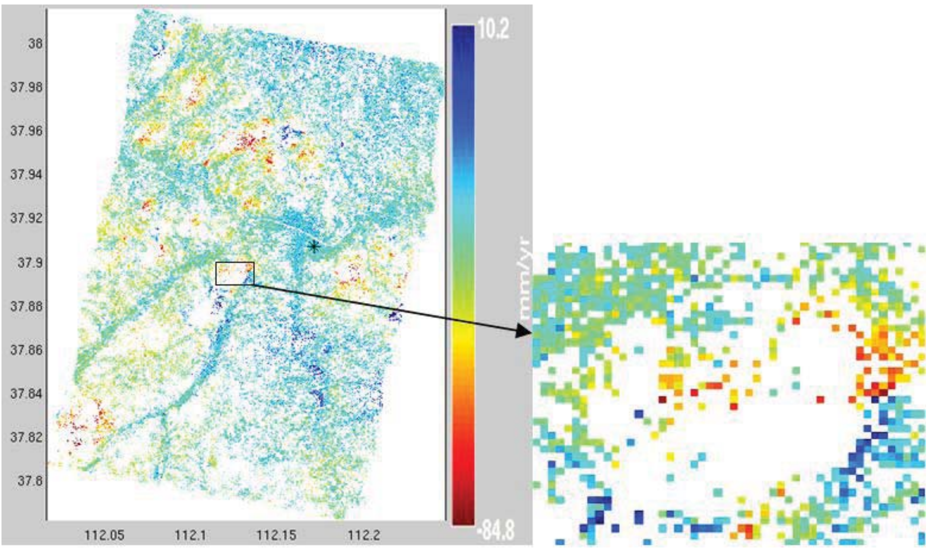

Figure 5.22 Persistent scatterers generated by PSInSAR using TerraSAR-X data set (Left) and an example of blank area (Right).

Table 5.7 TerraSAR-X pairs formed in this study.

Pairs	Master	Slave	$B_{temporal}$/day	B_{perp}/m
1	2012-04-04	2012-04-15	11	18
2	2012-04-15	2012-04-26	11	141
3	2012-04-15	2012-05-07	22	-101
4	2012-04-15	2012-05-18	33	10
5	2012-05-07	2012-05-18	11	113
6	2012-05-18	2012-05-29	11	22
7	2012-05-29	2012-06-09	11	12
8	2012-06-09	2012-06-20	11	-182
9	2012-06-20	2012-07-01	11	78
10	2012-07-01	2012-07-12	11	68
11	2012-07-12	2012-07-23	11	-155
12	2012-07-12	2012-08-14	33	12
13	2012-08-03	2012-08-14	11	152
14	2012-08-03	2012-08-25	22	96
15	2012-08-14	2012-08-25	11	-58
16	2012-08-25	2012-09-05	11	107
17	2012-08-25	2012-09-16	22	-46
18	2012-09-16	2012-09-27	11	3
19	2012-09-27	2012-10-08	11	7
20	2012-10-08	2012-10-19	11	71
21	2012-10-19	2012-11-10	22	30
22	2012-11-10	2012-11-21	11	-61

In this study, we combined DInSAR and time series analysis to 21 scenes time-ordered images. All GAMMA-related results and mining maps were provided by Zhenguo Liu in CUMT. The main aim is to find out the precise locations of deformation areas, which is an essential parameter for mining engineering. The basis flow of data analysis here includes combination of interferometric pairs, interferogram generation and time series analysis.

1. Combination of interferometric pairs.

As already discussed in section 5.8.2, the quality of final interferogram is mainly dependent on if master and slave images are with good coherence. Furthermore, strong topographic effects come with large spatial baselines should be considered carefully. Similar to what people do in SBAS or STBAS processing, we used pairs with small temporal and spatial baselines only to form interferograms. As in Table 5.7, totally 22 pairs were selected. One should note that connections between different pair should be ensured.

2. Interferogram generation.

In the following, DInSAR analysis is applied. The 90m SRTM Digital Elevation Model (DEM) was used throughout to aid in the interpretation and unwrapping of the interferograms. We processed all possible pairs and then abandoned inteferograms with low quality due to temporal and/or spatial decorrelations, or with big baseline errors. The analysis of individual interferograms illustrated the influence of topography on the interferometric phase. Large scale relief maps were collected and used to generate high resolution digitial elevation model (DEM), which was then used during DInSAR processing to compensate topography phase, and aid the interpretation and unwrapping of the differential interferograms. An adaptive filtering technique was applied to differential interferograms to clarify the fringes and to reduce noise. Interferograms are much smoother after filter. However, filters must always be used with care and we should keep in mind that filtering can remove more subtle effects.

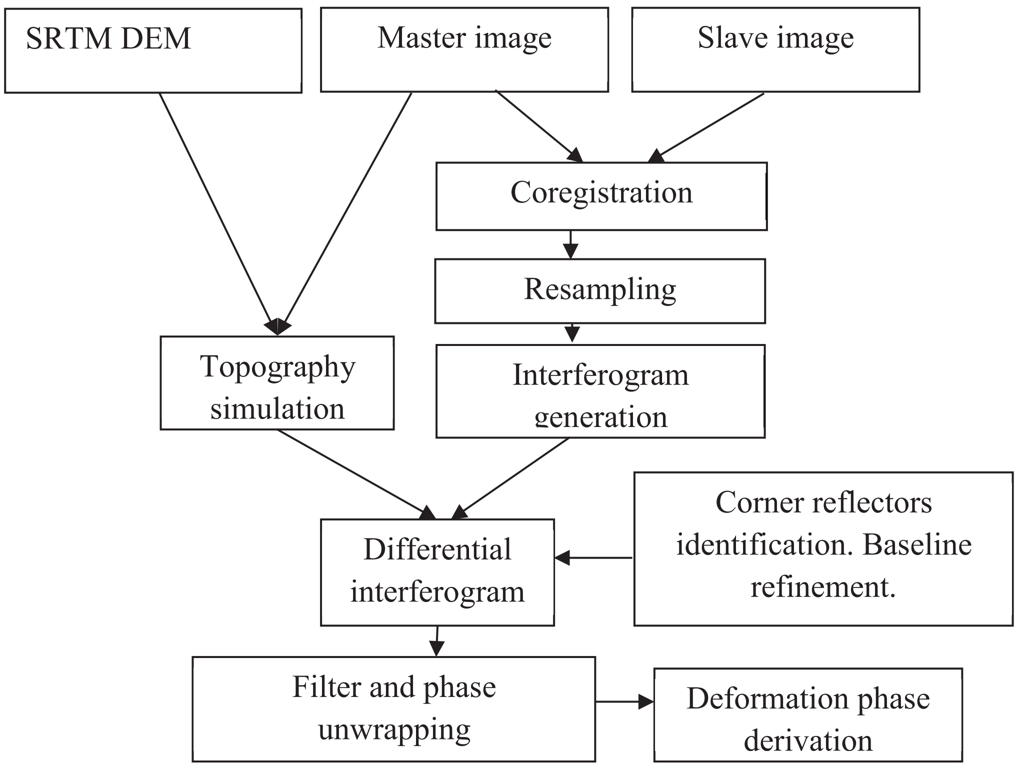

Figure 5.23 DInSAR flow chart in this study.

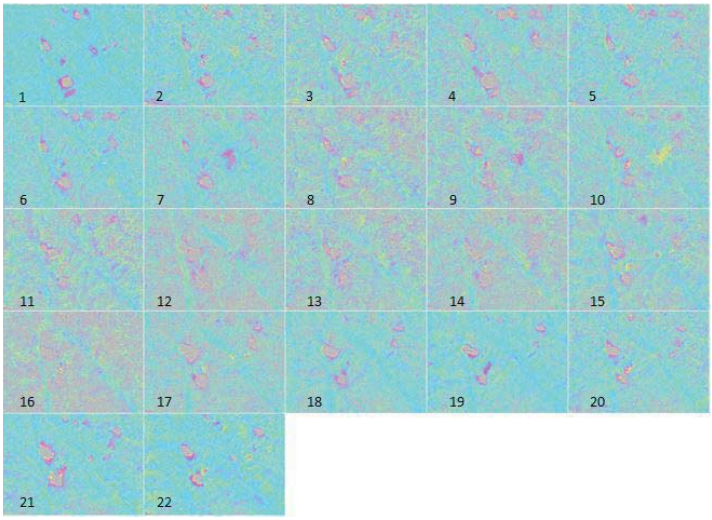

Figure 5.24 Interferograms generated by DInSAR using TerraSAR-X data set.

As showed before, corner reflectors can be identified from intensity maps or coherence maps easily. Hence, corner reflectors with GPS surveying could be considered as ground control points and used for baseline refinement, although the conventional baseline estimation may be already quite good because high precise orbits were provide by DLR. As for phase unwrapping, the Minimum Cost Flow (MCF) approach was chosen. All interferograms are after unwrapping.

3. Time series analysis.

Time series analysis was carried out when 22 scenes of interferogram were ready. The first acquisition, 20120404, was used as the reference (the start point of time series analysis). Therefore, the deformation phases on all other dates are related to that on 4th April, 2012. A sequence of cumulative subsidence phases were estimated and then converted into height changes.

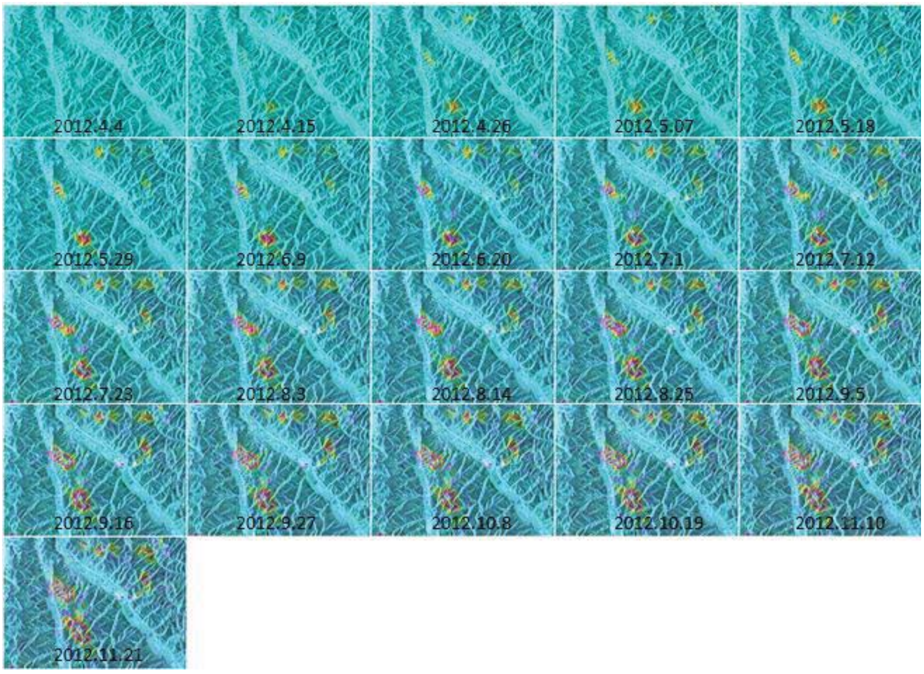

Figure 5.25 Time-ordered cumulative subsidence maps generated by time series analysis using TerraSAR-X data set. The deformation range is from 0 to 40cm.

5.8.5 InSAR - GPS measurements comparison

During the period of SAR data acquisitions, GPS surveying was carried out on stoping faces simultaneously. Due to the high reliability of GPS measurements, we compared it with InSAR results to verify the applicability of InSAR in such a challenging situation.

A control point which locates in border region of subsidence area of Tunlan mine was chosen for this comparative analysis. According to the time series of displacements, the control point moved -2.284 m in vertical direction from 4th April 2012 to 21st Nov 2012 (Fig. 5.26).

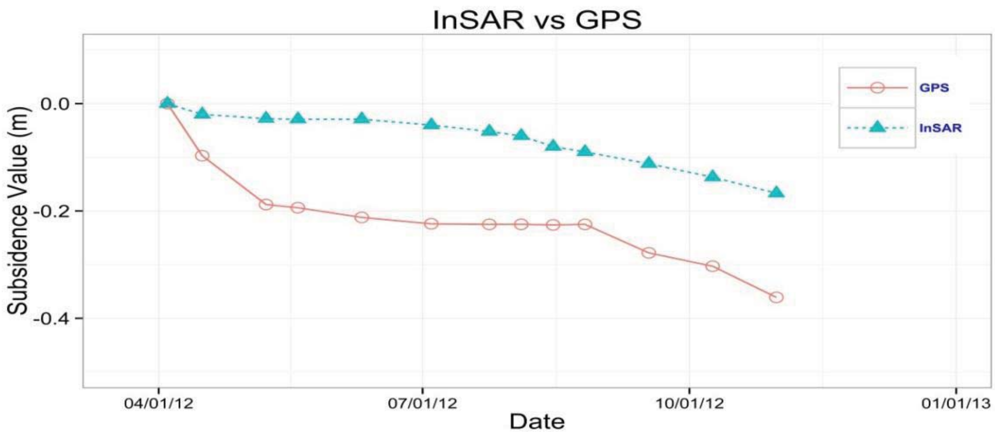

Figure 5.26 Two corner reflectors (CR1, CR2) shown on optical image (Upper) and displacements of CR1 during 220 days derived by GPS and InSAR respectively (Lower).

The InSAR derived subsidence is much smaller than this value. The reason could be:

- During the repeated mining progress, the ground surface was suffering from strong subsidence with big gradient. Therefore, the deformation gradient is far beyond the frontiers of InSAR's maximum Detectable Deformation Gradient (DDG).
- Xishan coal mines locate in a mountainous area full of vegetation, which causes coherence loss. Furthermore, the local time of TerraSAR-X pass was at 06:40 am, when the dew gather on the bushes and leaves in the summer (from July to September in Shanxi). The latter is another possible reason of coherence loss as well. Therefore, the number of available pairs for generating interferogram is reduced.

The maximum Detectable Deformation Gradient (DDG) was defined by Massonnet et al., in1998 and expressed as:

$$D_x = \frac{\lambda}{2\mu} \qquad (5.8.4.1)$$

where $\frac{\lambda}{2}$ is half of the wavelength and μ is the pixel size.

Furthermore, the full definition of the maximum Detectable Deformation Gradient (DDG) in terms of the coherence value is defined (Baran et al., 2005) as:

$$DDG = D_x + \frac{\gamma - 1}{500} \tag{5.8.4.2}$$

where γ is the coherence value.

For example, for TerraSAR-X, the DDG is 6×10^{-3} when the ground pixel size is 2.6m × 2.6m, and coherence value is 1. In this case, no more than 60cm displacement can be measured correctly over 100m long distance on the ground. One has to note it is a theoretic value of DDG that only valid under ideal conditions, but in practice there are always noises in the SAR system and only lower coherence value can be obtained so that a much smaller deformation gradient can be detected by InSAR.

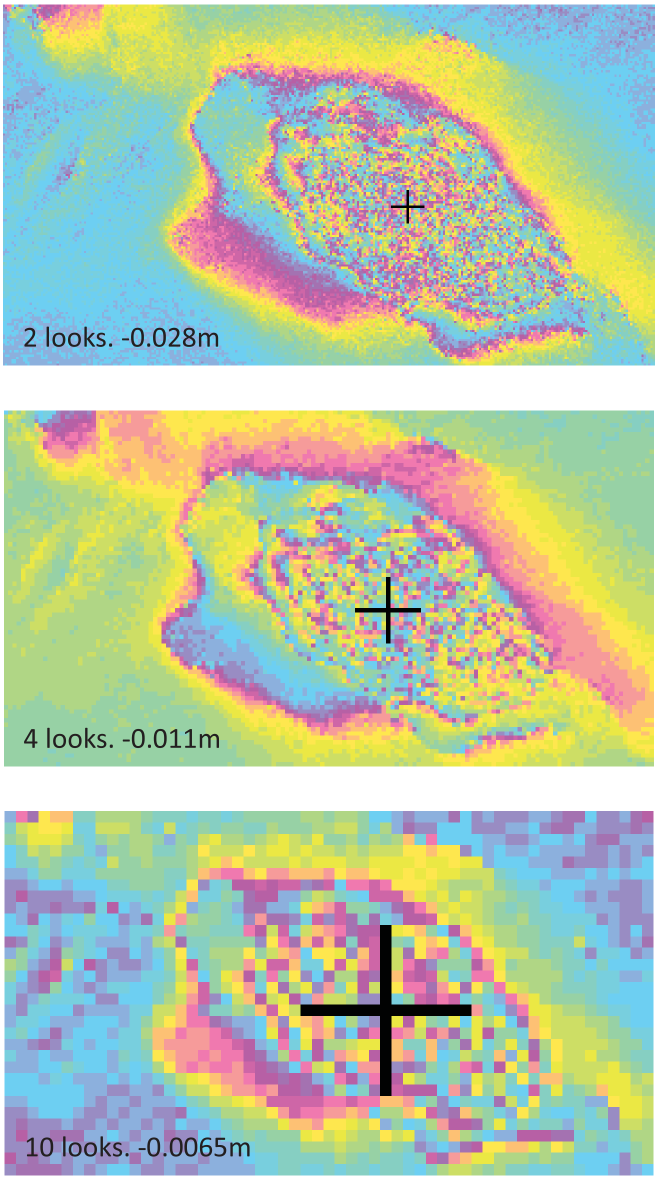

Figure 5.27 DDG test. Upper: 2 looks; Middle: 4 looks; Lower: 10 looks. The detected displacements at the centre point were indicated separately.

According to equation (5.8.4.1), two operations are available to increase the DDG when people come cross deformation with big gradients. The first is by increasing the wavelength and the other one is to reduce the pixel size (smaller look numbers). In this study, the later was used to improve DDG as the wavelength is 3.1 cm for TerraSAR-X. However, SAR images with small numbers of multi-looks will contain more noises as the aim of multi-look process is to weaken noises at the expense of reducing space resolution. In the DDG test (Fig. 5.27), 2-look seems to be a good choice for Xishan case where the deformation gradients are quite large.

With the aim of surmounting this DDG limitation, a hybrid StaMPS approach (Chen et al., 2014) and was applied to this area. Firstly, the offset-tracking approach was employed to extract large scale non-linear displacements. The remained phase is much easier to be unwrapped now. However, offset-tracking's precision is confined to the resolution and the accuracy of co-registration. Therefore, the second step, StaMPS method was introduced to make analysis of PS candidates and generate high accuracy estimation of phase changes. In other words, this is a combination of offset-tracking and StaMPS, which is hereby called hybrid StaMPS approach.

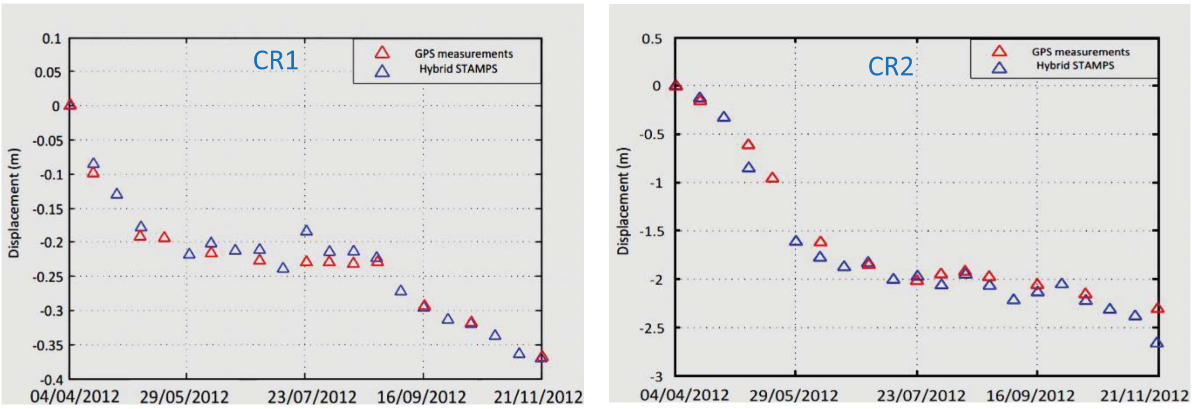

Figure 5.28 Displacements of CRs estimated by GPS and by the proposed approach Hybrid StaMPS.

From the hybrid StaMPS results, we would point out that more than 2m subsidence was observed in half a year. According to the validation by GPS measurements, this hybrid StaMPS approach indicates an exciting potential to measure big deformation. There is no doubt that DDG limitation could be overcome by the proposed method with the help of corner reflectors.

5.9 Correlation analysis of mining and InSAR measurements

Either from the view of production safety or of geoscience research, the participation of mine surveyors is demanded in mining activities (Preusse and Herzog, 2004). Concurrent with underground mining activities, subsidence usually occurs synchronously due to cavities created by underground mining. The extraction of coal seam removes support from the overlying rock strata and therefore makes them collapse into the void space that created by the excavation (Amuedo and Ivey, 1978). Such sag propagates upward to the ground surface which causes the surface subsidence and induces so-called subsidence trough. In Fig. 5.28, curve 1 indicates the subsidence history of a point P on the surface that affected by mining underground, and curve 2 represents the temporal effect of mining in terms of the maximum subsidence at the point P (Walter et al., 2004). The velocity and time delay of subsidence are also shown. Surface deformation varies with the type of mine, the geometry of mine and manner of excavations. After cessation of excavation, subsidence may continue for some time in a gradual manner. In some cases, subsidence would even stop for a period, to be followed by sudden or steady deformation at some later date.

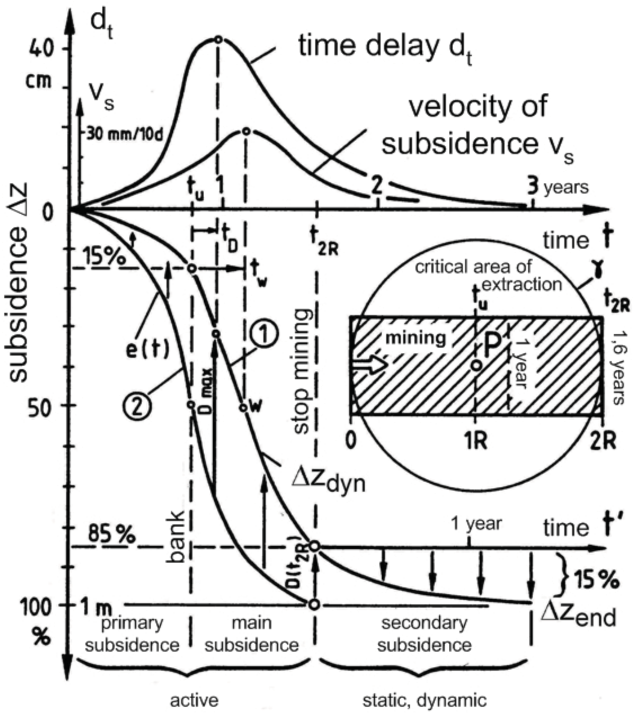

Figure 5.29. Mining induced subsidence at point P. (Kratzsch, 1997. Adapted by Walter et al., 2004).

One product, the subsidence hazard map or Subsidence Hazard Boundary (SHB), provided by geodesy engineer is requisite for mining production. Subsidence hazard boundary indicates areas where the ground surface suffered from subsidence related to underground mining activities.

When the maximum subsidence at the ground is usually less than the thickness of the coal seam mined (but not in some cases, for instance, with repeated mining), the extent of subsidence at the ground surface is much wider than that of underground mining area (Amuedo and Ivey, 1978).

Three terms have to be discussed when talking about SHB, apart from the maximum subsidence.

1. Advanced influence angle – The ground surface starts to move (10 mm as defined) before the underground working face arrives. In the sagittal plane, the angle between the horizontal line and the line connecting the working face and the ground starting moving point on the coal pillar side is so-called advanced influence angle.
2. Advanced influence distance – The horizontal distance between this starting moving point and the working face is advanced influence distance.
3. Initial moving distance, or starting distance of subsidence – In the sagittal plane, mining move forward inch by inch. The deformation propagates upward to the ground surface and makes it start to move (10 mm), when the underground working face moved forward a distance d_0. This critical distance d_0 is defined as initial moving distance. In other words, when the mining extent is less than the initial moving distance, mining subsidence on the ground surface is equal to zero. Mostly, the deformation propagates upward to the ground surface when the working face achieves $1/4$ or $1/3$ of the mining depth (He et al., 1991).

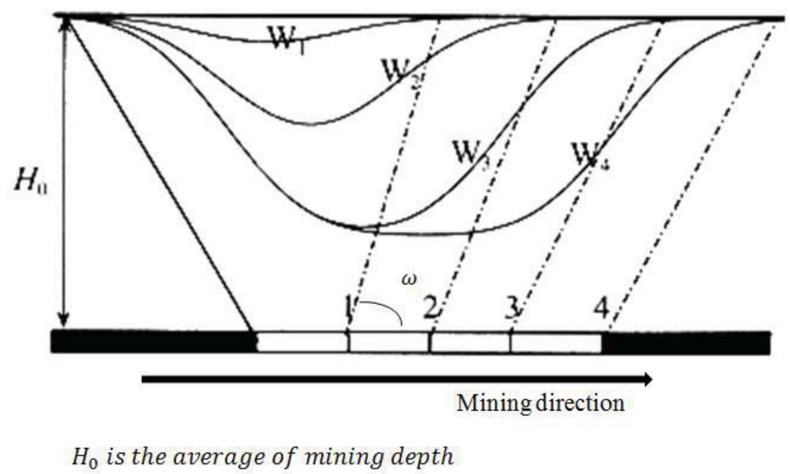

Figure 5.30 Surface subsidence basin (Adapted from He et al., 1991). ω is the advanced influence angle.

As mentioned, the underground mining will induce a big subsidence area at the ground surface and then comes into being a basin. In Figure 5.29, a basin W_1 will appear when the working face arrives at point 1. Along with the working face carries on, the basin will expand to be W_2 with a bigger depth. The maximum value of subsidence will not increase any more when the working face reaches to point 3, as this is critical extraction now. Following, W_4 is wider than W_3 but its depth will keep the same as that of W_3.

In order to obtain or Subsidence hazard boundary and relevant parameters, we carried out correlation analysis of mining and InSAR measurements (Liu and Bian., 2012).

5.9.1 Site 1 – Tunlan – 18207 working face

The main coal-bearing strata of Tunlan consist of 18 coal seams. 8 of them have high economic value for exploiting. The sum of thickness of strata is approximate 158.50 m, and the average thickness of coal seams is 15.70 m. Coal bearing ratio in this area is 10%.

Table 5.8 Information of 18207 working face and other working faces around.

Working face	Layers No.	Extraction Date	Length （m）	Width （m）	Thickness （m）	bed pitch （°）	roof to ground （m）
18207	8	2011.5-2012.10	1757	201	3	5	354-555
18a203	8a	2012.6-	817	198	1.46	4	313-493
12212	2	2008.1-2008.7	1320.5	889	3.2	5	342-488
12210	2	2006	1234	171	3.4	3	N/A
12208	2	2003-2004	1735	183	3.2	3	N/A
12206	2	2001-2002	1842	164	3.1	3	N/A
12202	2	1999-2000	1396	198	3.1	4	N/A
18205	8	2009.12-2010.12	1592	205	3.25	5	301-468
18203	8	2008.7-2009.10	1528	204	3.54	4	300-443
18201	8	2007.6-2008.5	1475	294	3.68	5	298-482

The working face 18207 locates inside Tunlan mine. The thickness from the roof of coal seam to the ground surface is 354 m to 555 m. The length of 18207 is 1757 m while the width is around 201 m. The sum of thickness of strata is approximate 2.3 to 3.65 m when the average thickness of coal seams is 3 m. The maximum coal bed pitch is 7° and the minimum is 3°, with an average of 5°. Therefore, 18207 working face is a comparatively regular coal seam.

As shown above, there are three layers of coal in this working face: No.2, No.8 and No.8a. Moreover, the details of working faces in this area were list as well.

In Figure 5.30, there are several goafs, which are marked as 12212, 12208, 12206 and 12202 in No.2 layer. In No.8 layers, 18205 and 18203 are goafs. Working face 18a203 started to mining in the latter half of the excavation of working face 18207. Apparently, surrounding ground will be affected by repeated mining influence.

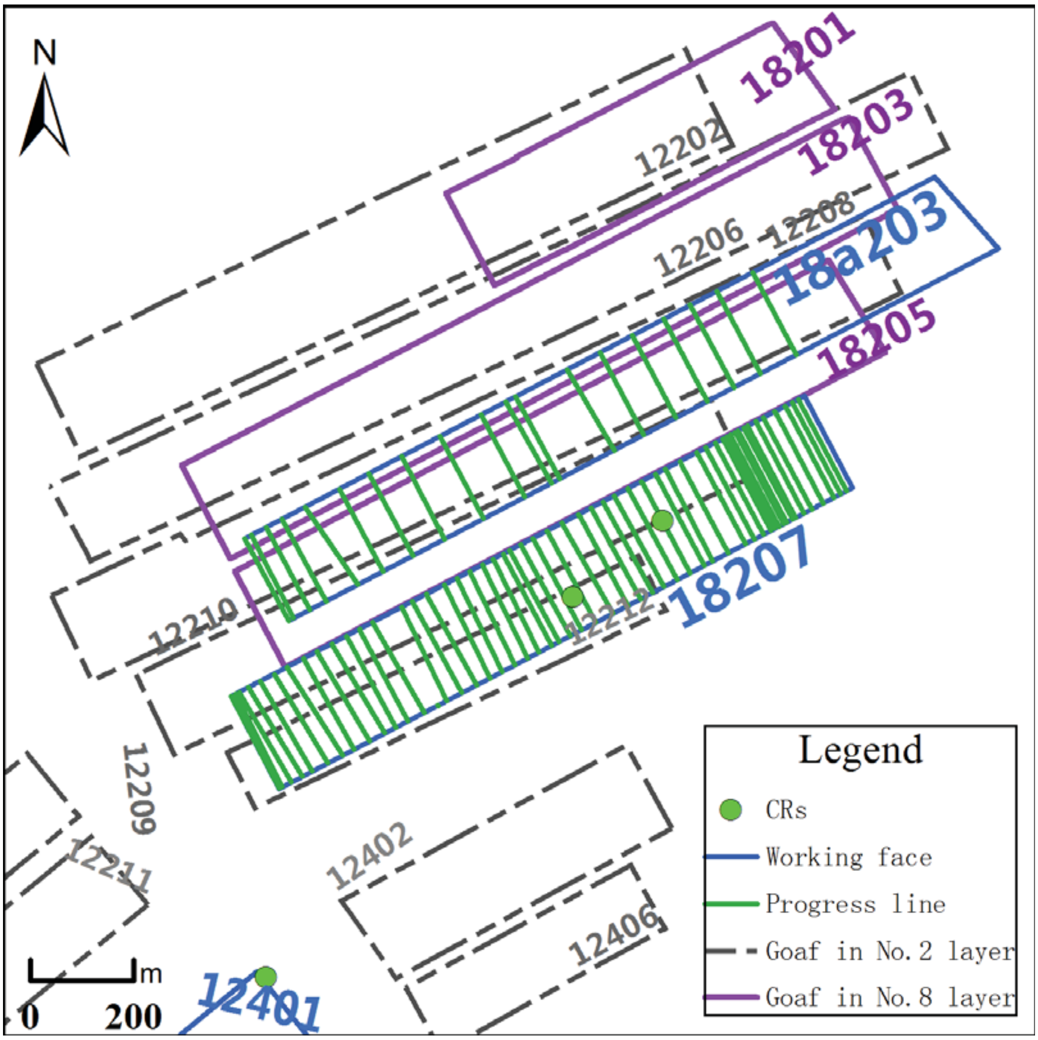

Figure 5.31 18207 working face with other working faces around. Green points are corner reflectors.

The extraction of coal in working face 18207 began in May, 2011 and completed in October, 2012. The distance of cumulative tunnelling is 870 m until 5th April, 2012. During the period with SAR data acquisitions (from 5th April, 2012 to 22nd November, 2012), the distance of cumulative tunnelling is 370 m. Time ordered InSAR results are then overlaid by mining maps in ArcGIS, with the aim of parameter extraction (Fig. 5.31).

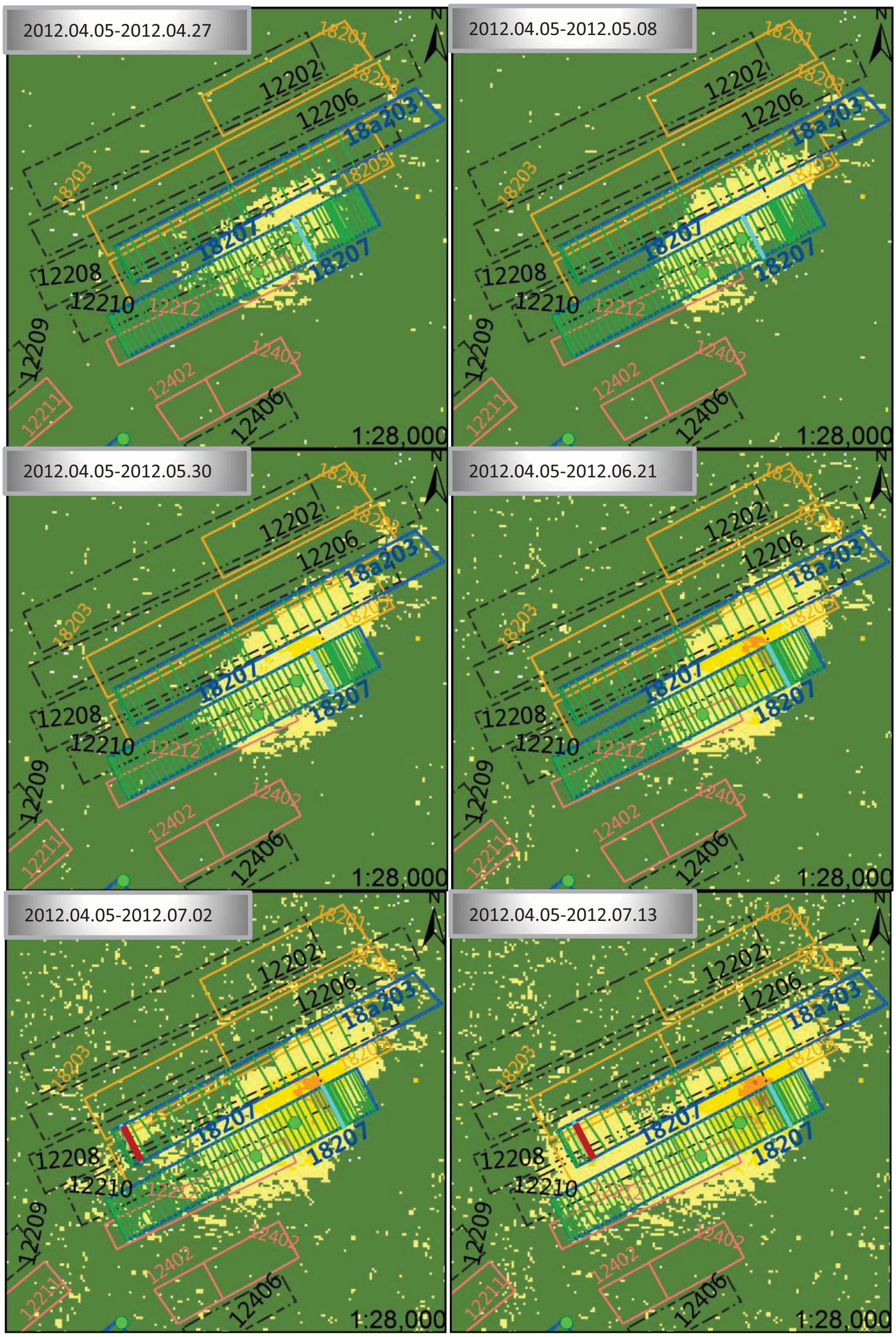
2012.04.05-2012.04.27
2012.04.05-2012.05.08
2012.04.05-2012.05.30
2012.04.05-2012.06.21
2012.04.05-2012.07.02
2012.04.05-2012.07.13
N
18201
12202
18203
12206
18a203
18205
18207
12208
12210
12212
12209
12402
12404
12406
12211
1:28,000

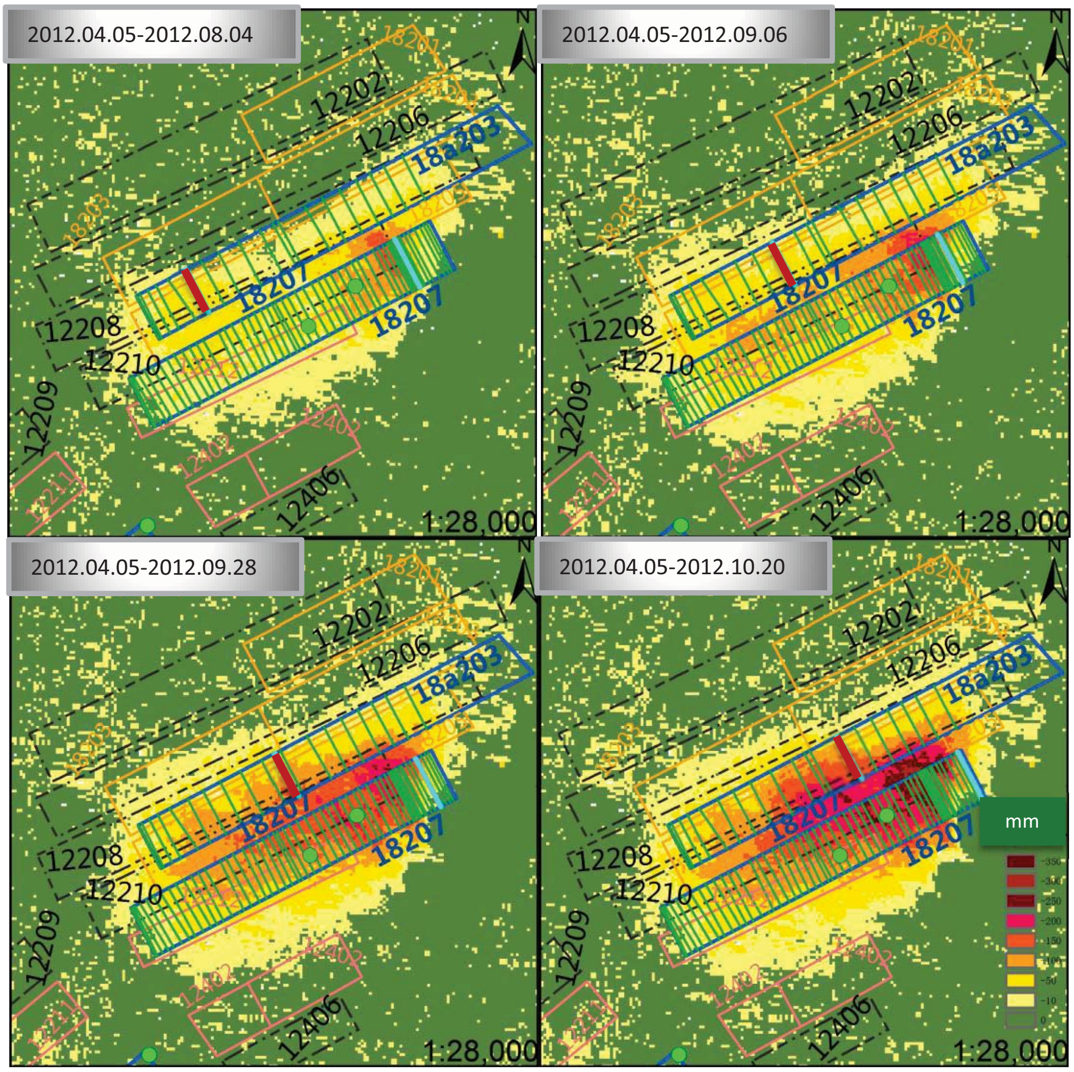

Figure 5.32 Time ordered subsidence maps in 18207 working face. Green points are corner reflectors. Blue and brown lines are progress lines and their dates are indicated respectively.

Four steps are necessary before the determination of advanced influence angle and distance:

- Find the progress line that its date is the closest to the time of SAR data acquisition. One has to note that the time of SAR data acquisition is in UTC, but it has to be converted to local time.
- Calculate the time difference between the time of SAR data acquisition and of the progress line.
- According to the mining record, the average speed of tunnelling should be estimated.
- Reckon the position of progress line on the date of SAR data acquisition, by combining the average speed of tunnelling and the time difference between the time of SAR data acquisition and of the progress line. The progress is assumed to be linear.

From 8th May, 2012 to 28th Sep, 2012, the advanced influence angle varies from 43° to 45° when 41° on 4th Aug, 2012 dispersed around 2°. An interesting exception appeared on 27th April, 2012, with an advanced influence distance of 248 m which is much shorter than those at other dates and an advanced influence angle of 60°. The explanation may go to the difference in the schedule of tunnelling or the composition of rocks, if more detailed information could be provided.

Table 5.9 Estimation of advanced influence angles/distances at different time in 18207 working face.

Date（local）	Mining depth/m	Subsidence boundary to working face/m	Advanced influence distance/m	Advanced influence angle/degree
2012.04.27	453	426	248	60
2012.05.08	453	424	413	46
2012.05.30	435	425	413	46
2012.06.21	435	425	412	46
2012.07.02	440	475	492	44
2012.07.13	442	475	488	44
2012.08.04	449	415	471	41
2012.09.06	453	382	440	43
2012.09.28	440	383	399	44

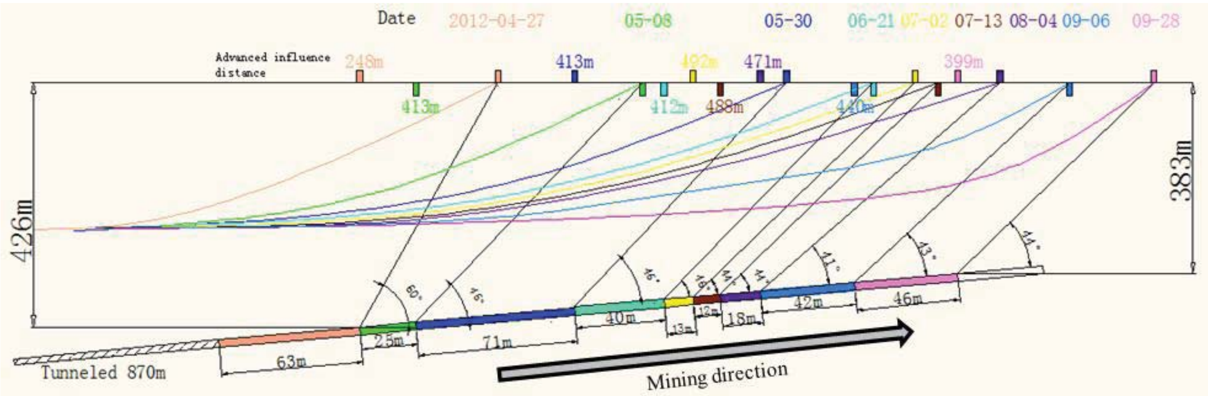

Figure 5.33 Expansion of subsidence basin caused by 18207 working face.

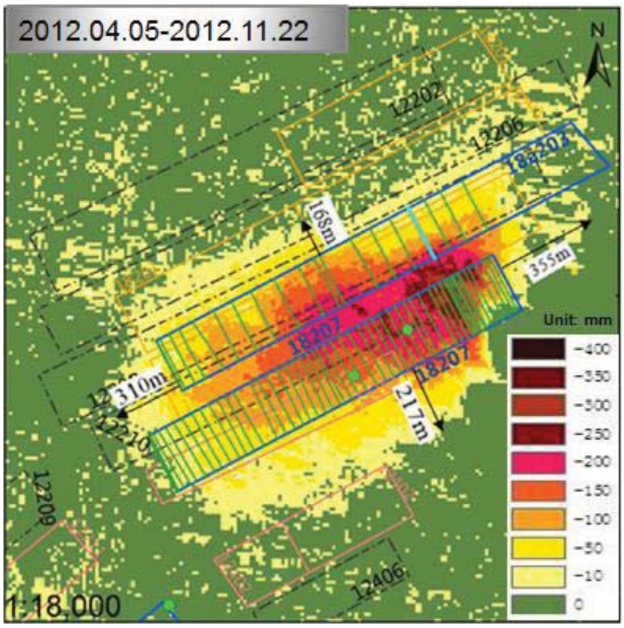

Figure 5.34 SHB caused by 18207 working face.

After 28th Sep, 2012, no clear expansion of subsidence boundary was detected, although the maximum displacement increased. According to the displacement map based on pair 20120405 and 20121122, the final subsidence hazard boundary around this working face was shown above.

In the displacement map 2012.04.05-2012.07.02, another basin appeared on the eastern side of the basin caused by the working face 18207. This is due to the started mining in 18a203 working face. As time went on, these two subsidence basins expanded wider and wider, and then merged with each other. If viewed from the vertical direction, 18207 and 18a203 working faces have different depths. The interconnecting area between these two basins was suffering from combined subsidence induced by the falling and collapsing in two working faces underground. As a result, we would prefer to not estimating initial moving distance in 18a203 working face case even though its starting moving time was monitored by DInSAR, as this is not a pure situation for calculation of initial moving distance induced by one single mine.

5.9.2 Site 2 – Xiqu – 18307 working face

The main coal-bearing strata of Xiqu consist of 14 coal seams. 8 of them have high economic value for exploiting. The sum of thickness of strata is approximate 159.79 m, and the average thickness of coal seams is 15.04 m. The working face 18307 locates inside Xiqu mine. The thickness from the roof of coal seam to the ground surface is 210 m to 280 m. The length of 18307 is 1061 m while the width is around 195 m. The sum of thickness of strata is approximate 3.8 to 4.35 m when the average thickness of coal seams is 4.15 m. The maximum coal bed pitch is 7° and the minimum is 2°, with an average of 4°. Therefore, 18207 working face is a comparatively regular coal seam.

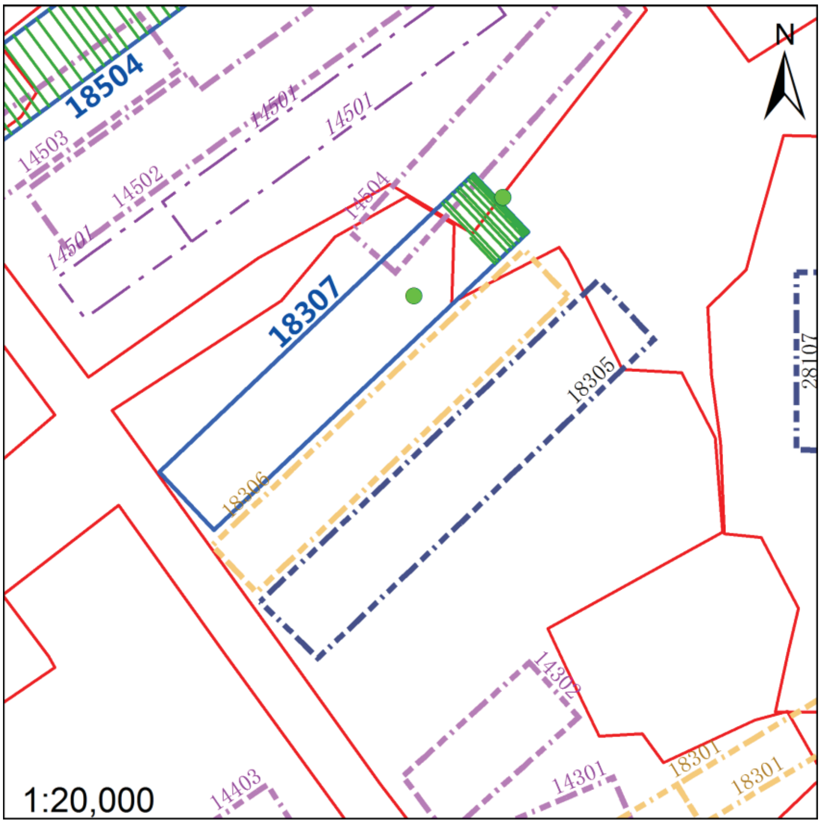

Figure 5.35 18307 working face with other working faces around. Green points are corner reflectors. Red lines show the goaf at other layers.

A layer 60-70 m above 18307 working face has completed the excavation (red lines in Fig. 5. 34). Another layer 55 m above 18307 working face contains three goafs marked as 14504, 18306 and 18305, which completed mining in July 2008, June 2010 and June 2008, respectively.

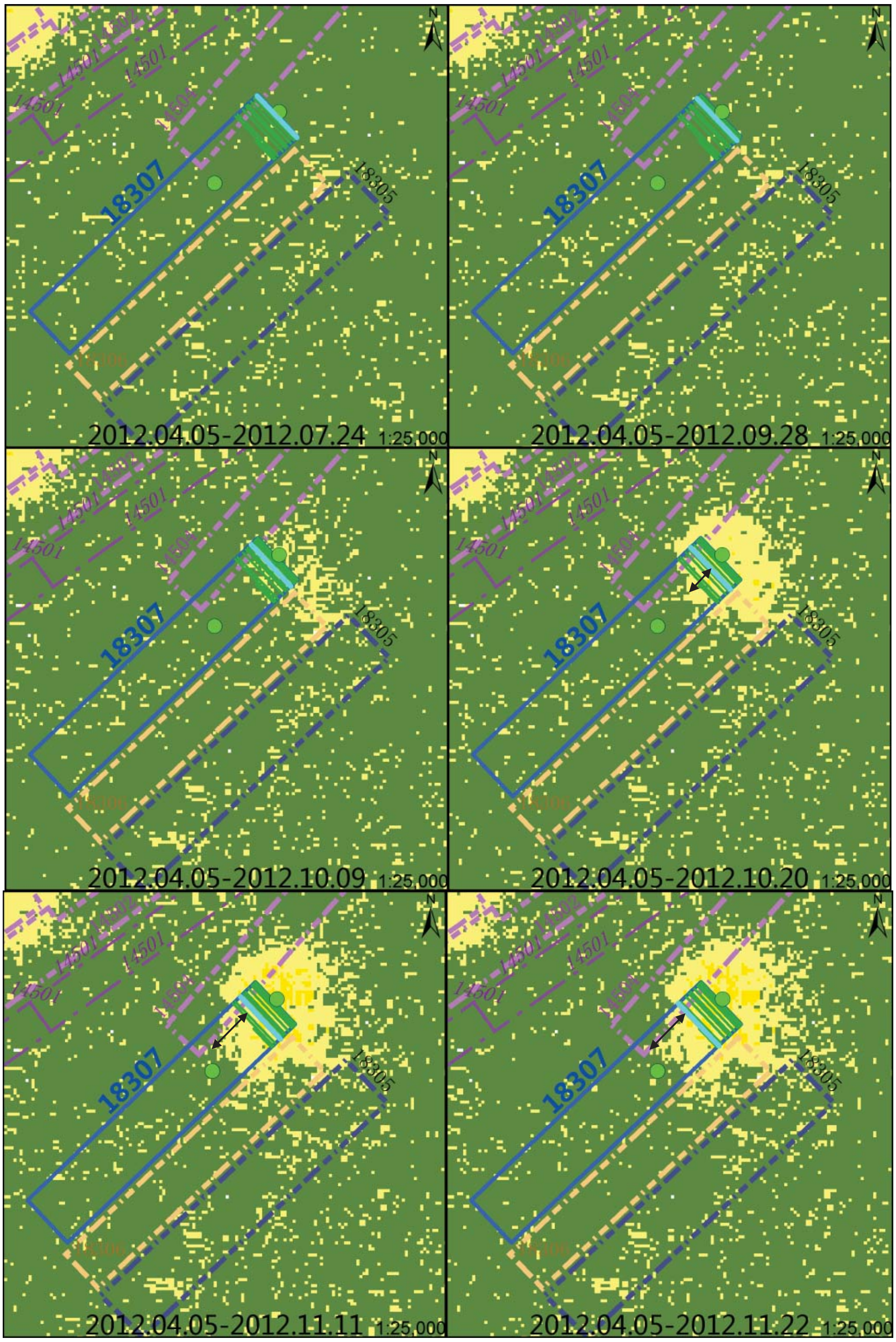

Figure 5.36 Time ordered subsidence maps in 18307 working face. Green points are corner reflectors. Blue lines are progress lines and their dates are indicated respectively.

This working face started coal extraction in July 2012 and totally moved forward 101 m until 22nd Nov, 2012. According to the subsidence map, the ground surface above this working face subsided for the first time on 9th Oct, 2012. At that date, the accumulative tunnelling is 38 m. Therefore, initial moving distance, or mining subsidence starting distance is 38 m in this case.

Table 5.10 Estimation of advanced influence angles/distances at different time in 18307 working face.

Date（local）	Subsidence boundary to working face/m	Advanced influence distance/m	Advanced influence angle/degree
2012.10.20	244	151	58.2
2012.11.11	236	180	52.7
2012.11.22	231	154	56.3

Based on combined analysis of InSAR result and mining schedule, advanced influence angles on 20th Oct 2012, 11th Nov 2012 and 22nd Nov 2012 are 58.2°, 52.7° and 56.3°. Respectively, three advanced influence distance are 151 m, 180 m and 154 m.

5.10 Geocoding Accuracy

The accuray of of SHB estimation mainly relies on the accuracy of geocoding. In order to assess the accuracy of the geocoding, the displacement maps with the corner reflectors were transformed to the World Geodetic System 1984 (WGS84) in UTM. Moreover, GPS processed results of the corner reflectors were used to compare with and evaluate the coordinates of corner reflectors in the displacement maps. It is delighted that the average error vector was 4 m. As for converting mining maps in BJZ54 into WGS84, the differences were considered to be negligible.

5.11 Summary

An experiment to apply InSAR to a mountainous area with strong mining activities has been undertaken in this chapter. The maximum displacement was not able to be detected by TerraSAR-X due to the big phase gradient. According to InSAR theory, the maximum detectable displacement is one fringe between two pixels. Therefore, a look test was carried out to find the best look number for measuring big subsidence by TerraSAR-X here. For further applications, longer wavelength and shorter revisit cycle were proposed for SAR system design, and less look number was suggested for InSAR data processing when the image quality allows. Another solution could be applying super high resolution SAR images, for instance, the coming TerraSAR-X data in staring spot light mode, which are able to provide images with very small pixels (less than 1 m).

By applying the Hybrid StaMPS to two corner reflectors, more than 2m displacements was observed in approximate half a year, which indicates an exciting potential to measure big deformation. It is concluded that DDG limitation could be partly overcome by the proposed method with the help of corner reflectors. Apart from detecting the maximum subsidence, InSAR fulfils the aim of SHB derivation. By studied the working face 18207, advanced influence angles and advanced influence distances are provided. Furthermore, it is confirmed that InSAR can measure the initial moving distances with the help of mining schedule according to the test at site 18307. We would point out that more precise estimation is possible when the sampling rate increases with shorter revisit cycle of SAR satellites.

Chapter 6 Conclusions and Recommendations

In chapter 1, a set of aims and objectives were stated. They were:

- What are the advantages and limitations of applying InSAR to monitoring movements in urban and non-urban areas?
- The atmospheric effects on InSAR measurements and how can we reduce the effects, for example, by new algorithms or by integrating other techniques like GPS observations in urban areas?
- How can SAR be used for detecting reliable movements when the movements are rapid and phase gradients are large?
- Can we use SAR for deriving mining parameters in mountainous area?

According to the research and work presented in this thesis, these aims are discussed following. After this, recommendations for further research are made.

6.1 Advantages and Limitations of InSAR

Comparing with conventional techniques, InSAR is inevitably the better technique for land movements monitoring. Even be ranked with advanced tools, such as GPS and laser scanner, Satellite-based SAR system has several significant advantages.

- The coverage of Satellite-based SAR is square kilometers and larger. For example, it is 30km by 50 km for TerraSAR-X image in SM mode.
- InSAR can detect relative change between acquisitions to millemetric levels.
- InSAR is an all-weather technique for monitoring land displacement, both during the day and night.

On the other hand, InSAR still has some limitations:

- InSAR does not provide 3D coordinates and only detects relative displacement.
- At the moment, InSAR is not a real-time system for geo-monitoring, as it requires post processing after observation.
- Atmospheric delay may contaminate the deformation signal when it is insignificant (in urban area).
- There is a limitation of measuring phase gradient in InSAR. When the phase gradient of displacements is too big, displacements could not be measured by InSAR correctly. This happened in Xishan experiment (chapter 5).

If we consider the different features of urban and non-urban area, the application of InSAR for land movements monitoring comes cross different problems. In urban area, there is little vegetation, but full of buildings and infrastructure, which are artificial scatterers. However, the displacement is normally insignificant and therefore easy to be contaminated by atmospheric delay. On the contrary, non-urban area lacks of buildings and infrastructure but is with abundance vegetation so that coherence loss is a problem that could not be ignored here. Besides, land movements in non-urban area people would like to pay attention to are always with higher intensity scale than in urban area. Another problem occurs to InSAR when the land displacements occur with big phase gradient and exceed the maximum detectable gradient of InSAR, which is half of the wavelength between two pixels.

6.2 PSInSAR and GPS in Urban Area – Düsseldorf

PSI and SBAS are the extension of conventional InSAR. They aim to dispel the influences of de-correlation and atmospheric delay in InSAR processing. PSI investigates the characteristics of all phase stable points on a succession of time-ordered SAR images. Such points with stable phase temporally are so-called PS points that with dominant scatterers in the resolution cells. In this study, Düsseldorf was used as the test site by processing 20 TerraSAR-X images. The algorithms and approaches integrated in the open source software DORIS and following StaMPS were chosen for data processing. Firstly, DORIS processed this TSX data set and formed interferograms. Subsequently, a combined MTI (multi-temporal InSAR) which integrated both PS and SBAS methods in StaMPS was applied for time series analysis of persistent scatterers selected. Atmospheric delay was estimated as a parameter and removed in this processing. The GPS station in Düsseldorf was set as the start point of 3-D unwrapping. Levelling results provided by the State Capital of Düsseldorf validated the PSInSAR result, when two time series showed similar progress with very few discrepancies. Furthermore, we compared PPP-derived atmospheric delay to that estimated by PSInSAR. PPP-derived indicated smaller ZWD than that PSInSAR-derived. However, using PPP for atmospheric delay shows a good potential due to its continuously observation, rather than relative measurements from different passes by InSAR.

6.3 Large Phase Gradient in Mining Area – Xishan Mine

Xishan was chosen as the test site in this project because of several reasons. Firstly, Xishan is well served by mining schedule and literature. Secondly, strong mining activities were and are carrying out in Xishan. These mining activities always induce rapid movements with big phase gradients, which provide people a precious chance to look at the DDG limitation. Another major advantage is that the TerraSAR-X acquisitions is cooperated by synchronous field work and GPS and corner reflector measurements.

According to the InSAR theory, two operations are available to increase the DDG when people deal with deformation with big gradients. The first is by increasing the wavelength and the other one is to reduce the look numbers. In this study, the later was used to improve DDG as the wavelength is fixed to be approximate 3.1 cm for TerraSAR-X. However, SAR images with small numbers of multi-looks contain more noises as the aim of multi-look process is to weaken noises at the expense of reducing space resolution. In the DDG test, 2-look seems to be a good choice for Xishan case where the deformation gradients are quite large. A conclusion is we have to select SAR data set with suitable wavelength and choose a good look number for InSAR processing, in order to make sure reliable results are obtained. Besides, with the help of the Hybrid StaMPS, the integration of offset-tracking and StaMPS approach, more than 2m displacement was observed in approximate half a year. The results were validated by GPS measurements with good accuracies, which show an exciting potential to measure big deformation.

6.4 InSAR for Deriving Mining Parameters – Xishan Mine

In the experiments carried out in Xishan mine, InSAR fulfils the aim of mining parameters derivation. Advanced influence angle and distance were successfully estimated for the test at Tunlan test site. Besides, it was confirmed that InSAR can measure the initial moving distances with the help of mining schedule at Xiqu test site. Due to the retention of high coherence and being strong back scatterers, corner reflectors were involved in this experiment. GPS was employed to measure the coordinates of corner reflectors, which helped the baseline refinements, and validated the accuracy of geocoding.

6.5 Recommendations for Further work

The items following may indicate valuable points for further research and lead to dramatic results:

- Combine Satellite-based SAR data sets with long wavelength and those with high resolution for InSAR processing.
- Develop new algorithms for detecting displacement in azimuth direction, such as advanced offset tracking or multi-aperture InSAR. Extend InSAR measurements from one dimension to two or three dimensions. This is extremely important for monitoring landslides, glacier, and so on.

References

Adam, Nico, et al. "Practical persistent scatterer processing validation in the course of the Terrafirma project." Journal of Applied Geophysics 69.1 (2009): 59-65.

Agram, Piyush Shanker. Persistent Scatterer Interferometry in Natural Terrain. Diss. stanford university, 2010.

Ahrens, C. Donald. Essentials of meteorology: an invitation to the atmosphere. Cengage Learning, 2011.

Amuedo, C. L, and Ivey, J. B., Coal and Clay Mine Hazard Study and Estimated Unmined Coal Resources, Jefferson County, Colorado, 1978.

Berrada Baby, H., P. Gole, and J. Lavergnat. "A model for the tropospheric excess path length of radio waves from surface meteorological measurements."Radio science 23.6 (1988): 1023-1038.

Bamler, Richard, and Philipp Hartl. "Synthetic aperture radar interferometry."Inverse problems 14.4 (1998): R1.

Bamler, R. "Radar interferometry for surface deformation assessment." Summer School Alpbach (2006).

Baran, Ireneusz, Mike Stewart, and Sten Claessens. "A new functional model for determining minimum and maximum detectable deformation gradient resolved by satellite radar interferometry." Geoscience and Remote Sensing, IEEE Transactions on 43.4 (2005): 675-682.

Bechor, Noah. Extending interferometric synthetic aperture radar measurements from one to two dimensions. Diss. Stanford University, 2006.

Bechor, Noa BD, and Howard A. Zebker. "Measuring two- dimensional movements using a single InSAR pair." Geophysical research letters 33.16 (2006).

Berardino, Paolo, et al. "A new algorithm for surface deformation monitoring based on small baseline differential SAR interferograms." Geoscience and Remote Sensing, IEEE Transactions on 40.11 (2002): 2375-2383.

BGS, Earthwise issue 18, Geology and Planning. Tech. Rep. 18, BGS, 2002.

Bingley, R. M., Satellite Positioning, Lecture, Institute of Engineering Surveying and Space Geodesy, 2008.

Boehm, Johannes, and Harald Schuh. "Vienna mapping functions in VLBI analyses." Geophysical Research Letters 31.1 (2004).

Böhm, Johannes, Robert Heinkelmann, and Harald Schuh. "Short note: a global model of pressure and temperature for geodetic applications." Journal of Geodesy 81.10 (2007): 679-683.

Boehm, Johannes, Birgit Werl, and Harald Schuh. "Troposphere mapping functions for GPS and very long baseline interferometry from European Centre for Medium- Range Weather Forecasts operational analysis data." Journal of Geophysical Research: Solid Earth (1978–2012) 111.B2 (2006).

Böhm, Johannes, et al. "Global Mapping Function (GMF): A new empirical mapping function based on numerical weather model data." Geophysical Research Letters 33.7 (2006).

Chao, C. C. "A model for tropospheric calibration from daily surface and radiosonde balloon measurements." Tech. Memo. 391-350, Jet Propul. Lab.(1972).

Chen, R., Yu, W., Wang, R., Li, X., Shao, Y., Liu, G., and Liu, D., "A Hybrid StaMPS Approach to Measure Large Displacement Caused by Coal Mining." IEEE Transactions on Geoscience and Remote Sensing, under review, 2014.

Collins, John Paul. Assessment and development of a tropospheric delay model for aircraft users of the global positioning system. University of New Brunswick (Canada)., 1999.

Curlander, John C., and Robert N. McDonough. Synthetic aperture radar. Vol. 199. No. 1. New York: Wiley, 1991.

Davis, J. L., et al. "Geodesy by radio interferometry: Effects of atmospheric modeling errors on estimates of baseline length." Radio science 20.6 (1985): 1593-1607.

Elgered, Gunnar, and Per OJ Jarlemark. "Ground- based microwave radiometry and long-term observations of atmospheric water vapor." Radio Science 33.3 (1998): 707-717.

Ferretti, Alessandro, et al. InSAR Principles-Guidelines for SAR Interferometry Processing and Interpretation. Vol. 19. 2007.

Farr, Tom G., and Mike Kobrick. "Shuttle Radar Topography Mission produces a wealth of data." Eos, Transactions American Geophysical Union 81.48 (2000): 583-585.

Farr, Tom G., et al. "The shuttle radar topography mission." Reviews of geophysics 45.2 (2007).

Feltens, J., and S. Schaer. "IGS Products for the Ionosphere." Proceedings, 1998.

Ferretti, Alessandro, Claudio Prati, and Fabio Rocca. "Nonlinear subsidence rate estimation using permanent scatterers in differential SAR interferometry."Geoscience and Remote Sensing, IEEE transactions on 38.5 (2000): 2202-2212.

Ferretti, Alessandro, Claudio Prati, and Fabio Rocca. "Measuring subsidence with SAR interferometry applications of the permanent scatterers technique." Workshop on Advanced Techniques for the Assessment of Natural Hazards in Mountain Areas. 2000.

Ferretti, Alessandro, Claudio Prati, and Fabio L. Rocca. "Permanent scatterers in SAR interferometry." Remote Sensing. International Society for Optics and Photonics, 1999.

Fialko, Yuri, Mark Simons, and Duncan Agnew. "The complete (3- D) surface displacement field in the epicentral area of the 1999 Mw7. 1 Hector Mine earthquake, California, from space geodetic observations." Geophysical Research Letters 28.16 (2001): 3063-3066.

Fielding, Eric J., et al. "Surface ruptures and building damage of the 2003 Bam, Iran, earthquake mapped by satellite synthetic aperture radar interferometric correlation." Journal of Geophysical Research: Solid Earth (1978–2012) 110.B3 (2005).

Geng, Jianghui. Rapid integer ambiguity resolution in GPS precise point positioning. Diss. University of Nottingham, 2011.

Geng, J., et al. "Kinematic precise point positioning at remote marine platforms." GPS solutions 14.4 (2010): 343-350.

Goldstein, Richard M., Howard A. Zebker, and Charles L. Werner. "Satellite radar interferometry: Two- dimensional phase unwrapping." Radio Science 23.4 (1988): 713-720.

Hanssen, Ramon. Atmospheric heterogeneities in ERS tandem SAR interferometry. The Netherlands: Delft University Press, 1998.

Hanssen, Ramon F. Radar interferometry: data interpretation and error analysis. Vol. 2. Springer, 2001.

Hanssen, Ramon, and Richard Bamler. "Evaluation of interpolation kernels for SAR interferometry." IEEE Transactions on Geoscience and Remote Sensing37.1 (1999): 318-321.

He, G., Yang, L., Ling, G., Mining Subsidence, CUMT press, 1991.

Henderson, Floyd M., and Anthony J. Lewis. Principles and applications of imaging radar. Manual of remote sensing, volume 2. John Wiley and sons, 1998.

Hinz, S., Alshawaf, F., Fuhrmann, T., Heck, B., Knöpfler, A., Luo, X., Mayer, M., Schenk, A., Thiele, A, and Westerhaus, M, "Atmosphärenkorrekturen Durch Integration Von Insar Und GNSS Beobachtungen." Proceedings of Geomonitoring, 2012.

Hong, Sang-Hoon, et al. "Multi-temporal monitoring of wetland water levels in the Florida Everglades using interferometric synthetic aperture radar (InSAR)."Remote Sensing of Environment 114.11 (2010): 2436-2447.

Hooper, Andrew John. Persistent scatter radar interferometry for crustal deformation studies and modeling of volcanic deformation. 2006.

Hooper, Andrew. "A multi- temporal InSAR method incorporating both persistent scatterer and small baseline approaches." Geophysical Research Letters 35.16 (2008).

Hooper, A., P. Segall, and H. Zebker. "Persistent scatterer interferometric synthetic aperture radar for crustal deformation analysis, with application to Volcán Alcedo, Galápagos." Journal of Geophysical Research: Solid Earth (1978–2012) 112.B7 (2007).

Hooper, Andrew, et al. "A new method for measuring deformation on volcanoes and other natural terrains using InSAR persistent scatterers." Geophysical research letters 31.23 (2004).

Hopfield, H. S. "Two- quartic tropospheric refractivity profile for correcting satellite data." Journal of Geophysical research 74.18 (1969): 4487-4499.

JPL, "GNSS-Inferred Positioning System and Orbit Analysis Simulation Software package." https://gipsy-oasis.jpl.nasa.gov/index.php?page=home (available on 4th March 2013).

Kampes, Bert M., Ramon F. Hanssen, and Zbigniew Perski. "Radar interferometry with public domain tools." Proceedings of FRINGE. 2003.

Klobuchar, John A. Present status and future prospects for ionospheric propagation corrections for precise time transfer using GPS. Phillips Lab Hanscom Afb Ma, 1991.

Klobuchar, John. "Ionospheric effects on GPS." Global Positioning System: Theory and applications. 1 (1996): 485-515.

Kouba, Jan. "A guide to using International GNSS Service (IGS) products."International GNSS (2009).

Kratzsch, Helmut. "Bergschadenkunde. 3. ergänzte Auflage." Deutscher Markscheider-Verein, Bochum (1997).

Krivenko, A., Riedel, B., Niemeier, W., Schindler, S., Heek, P., Mark, P, and Ziem, E, "Monitoring The Subway Construction Site "Wehrhahnlinie" In Düsseldorf Using Radar Interferometry. " Proceedings of Geomonitoring, 2012.

Lanari, Riccardo, et al. "An overview of the small baseline subset algorithm: A DInSAR technique for surface deformation analysis." Pure and Applied Geophysics 164.4 (2007): 637-661.

Lanari, Riccardo, et al. "A small-baseline approach for investigating deformations on full-resolution differential SAR interferograms." Geoscience and Remote Sensing, IEEE Transactions on 42.7 (2004): 1377-1386.

Leighton, J. M. GPS and PSI integration for monitoring urban land movements, Diss. 2010.

Li, Zhenhong. Correction of atmospheric water vapour effects on repeat-pass SAR interferometry using GPS, MODIS and MERIS data. Diss. 2005.

Li, Fuk K., and Richard M. Goldstein. "Studies of multibaseline spaceborne interferometric synthetic aperture radars." Geoscience and Remote Sensing, IEEE Transactions on 28.1 (1990): 88-97.

Lillesand, Thomas M., Ralph W. Kiefer, and Jonathan W. Chipman. Remote sensing and image interpretation. No. Ed. 5. John Wiley & Sons Ltd, 2004.

Liu, D., Sowter, A., Liu, Z., Niemeier, W, and Bian, Z. "Initial evaluation of insar technology for monitoring land deformation caused by mining in a mountainous area." Proceedings of ISM Conference, 2012.

Liu, Zhenguo, et al. "Monitoring on subsidence due to repeated excavation with DInSAR technology." International Journal of Mining Science and Technology23.2 (2013): 173-178.

Lu, Zhong, and Daniel Dzurisin. "Ground surface deformation patterns, magma supply, and magma storage at Okmok volcano, Alaska, from InSAR analysis: 2. Coeruptive deflation, July–August 2008." Journal of Geophysical Research: Solid Earth (1978–2012) 115.B5 (2010).

Lutgens, F. K., and E. J. Tarbuck. "The Atmosphere: an Introduction to Meteorology. 2001."

Mark, Peter, et al. "Radarinterferometrie zum Setzungsmonitoring beim Tunnelbau." Bautechnik 89.11 (2012): 764-776.

Massonnet, Didier, and Kurt L. Feigl. "Discrimination of geophysical phenomena in satellite radar interferograms." Geophysical research letters22.12 (1995): 1537-1540.

Massonnet, Didier, and Kurt L. Feigl. "Radar interferometry and its application to changes in the Earth's surface." Reviews of geophysics 36.4 (1998): 441-500.

Niell, A. E. "Global mapping functions for the atmosphere delay at radio wavelengths." Journal of Geophysical Research: Solid Earth (1978–2012)101.B1 (1996): 3227-3246.

Odijk, Dennis. "Fast precise GPS positioning in the presence of ionospheric delays." (2002).

Olmsted, Coert. "Alaska SAR Facility scientific SAR user’s guide." University of Alaska Fairbanks, Geophysical Institite. ASF-SD-003 (1993).

Osmanoglu, Batuhan. "Applications and development of new algorithms for displacement analysis using InSAR time series." (2011).

Peltzer, Gilles, and Paul Rosen. "Surface displacement of the 17 May 1993 Eureka Valley, California, earthquake observed by SAR interferometry." Science268.5215 (1995): 1333-1336.

Preuße, A, and Herzog, Chr. "Alternative fuels – a new field for mine surveying." ISM China, 2004.

Qu, W. J., et al. "The Evaluation of Precision about Hopfield, Saastamoinen and EGNOS Tropospheric Delay Correction Model." Acta Astronomica Sinica 49 (2008): 113-122.

Rees, Manfred Hugh. Physics and chemistry of the upper atmosphere. Vol. 1. Cambridge University Press, 1989.

Riedel, B., and A. Walther. "InSAR processing for the recognition of landslides."Advances in Geosciences 14 (2008).

Saastamoinen, J. "Atmospheric correction for the troposphere and stratosphere in radio ranging satellites." Geophysical Monograph Series 15 (1972): 247-251.

Sandwell, David T., Lydie Sichoix, and Bridget Smith. "The 1999 Hector Mine earthquake, southern California: Vector near-field displacements from ERS InSAR." Bulletin of the Seismological Society of America 92.4 (2002): 1341-1354.

Seeber, Gunter. "Satellite Geodesy: Foundations." Methods, and Applications, Waler de Gruyter, Berlin, New York (1993).

Scharroo, Remko, and Pieter Visser. "Precise orbit determination and gravity field improvement for the ERS satellites." Journal of Geophysical Research: Oceans (1978–2012) 103.C4 (1998): 8113-8127.

Shimada, Masanobu. "Correction of the satellite's state vector and the atmospheric excess path delay in SAR Interferometry-Application to surface deformation detection." Geoscience and Remote Sensing Symposium, 2000. Proceedings. IGARSS 2000. IEEE 2000 International. Vol. 5. IEEE, 2000.

Skolnik, Merrill I. "Introduction to radar." Radar Handbook (1962): 1990.

Sousa, J. J. Potential of Integrating PSI Methodologies in the Detection of Surface Deformation. Diss. PhD Thesis, University of Porto, Portugal, 2009.

Sowter, A. "Orthorectification and interpretation of differential InSAR data over mountainous areas: a case study of the May 2008 Wenchuan Earthquake."International Journal of Remote Sensing 31.13 (2010): 3435-3448.

Sowter, Andrew. "Phase ambiguity determination for the positioning of interferometric SAR data." The Photogrammetric Record 18.104 (2003): 308-324.

Tong, X., and D. Sandwell, "Assessment of Ionospheric Corrections to ALOS L-Band Interferograms." TIGIR workshop, Pasadena, California, 2009.

Wadge, G., and B. Parsons. "Achieving the EVINSAR objectives with TerraSAR-L." Proc. Third International Workshop on ERS SAR Interferometry, Frascati, Italy, 2–5 December. 2003.

Wadge, G., et al. "Atmospheric models, GPS and InSAR measurements of the tropospheric water vapour field over Mount Etna." Geophysical Research Letters29.19 (2002): 11-1.

Walter, D., Hoffmann, J., Kampes, B., and Sroka, A., "Radar Interferometric Analysis Of Mining Induced Surface Subsidence Using Permanent Scatterer." 2004 Envisat & ERS. Symposium, 6-10 September 2004, Salzburg, Austria, 2004.

Warren, Mark. The development of a 3-Pass Persistent Scatterer algorithm using the Integer Ambiguity Search method. Diss. University of Nottingham, 2007.

Webley, P.W. Atmospheric water vapour correction to InSAR surface movements measurements on mountains: case study on mount etna, Diss. University of Nottingham, 2003.

Wright, Tim J., Barry E. Parsons, and Zhong Lu. "Toward mapping surface deformation in three dimensions using InSAR." Geophysical Research Letters31.1 (2004).

Xia, Ye. "CR-Based SAR-Interferometry for landslide monitoring." Geoscience and Remote Sensing Symposium, 2008. IGARSS 2008. IEEE International. Vol. 2. IEEE, 2008.

Yuan, Xiao-kang. "Introduce to the Spaceborne Synthetic Aperture Radar."National Defense Industry Press, Beijing (2003).

Zebker, Howard A., and Yanping Lu. "Phase unwrapping algorithms for radar interferometry: residue-cut, least-squares, and synthesis algorithms." JOSA A15.3 (1998): 586-598.

Zebker, Howard A., et al. "On the derivation of coseismic displacement fields using differential radar interferometry: The Landers earthquake." Journal of Geophysical Research: Solid Earth (1978–2012) 99.B10 (1994): 19617-19634.

Zebker, Howard A., and Richard M. Goldstein. "Topographic mapping from interferometric synthetic aperture radar observations." Journal of Geophysical Research: Solid Earth (1978–2012) 91.B5 (1986): 4993-4999.

Zebker, Howard A., and John Villasenor. "Decorrelation in interferometric radar echoes." Geoscience and Remote Sensing, IEEE Transactions on 30.5 (1992): 950-959.

Zumberge, J. F., et al. "Precise point positioning for the efficient and robust analysis of GPS data from large networks." Journal of Geophysical Research: Solid Earth (1978–2012) 102.B3 (1997): 5005-5017.